University of California
Santa Barbara

Co-design of Electronic and Silicon Photonic Integrated Circuits for Microwave Photonics and Data-Center Communications

A dissertation submitted in partial satisfaction
of the requirements for the degree

Doctor of Philosophy
in
Electrical and Computer Engineering

by

Navid Hosseinzadeh

Committee in charge:

Professor James F. Buckwalter, Chair
Professor Clint L. Schow
Professor John E. Bowers
Professor Jonathan Klamkin

September 2020

The Dissertation of Navid Hosseinzadeh is approved.

Professor Clint L. Schow

Professor John E. Bowers

Professor Jonathan Klamkin

Professor James F. Buckwalter, Committee Chair

July 2020

Co-design of Electronic and Silicon Photonic Integrated Circuits for Microwave Photonics and Data-Center Communications

by

Navid Hosseinzadeh

To Mitra, and my parents, Reza and Forouzan

Acknowledgements

My appreciation and gratitude extends to many people who helped me for the past few years and made this work possible. I am deeply grateful to my advisor, Prof. Jim Buckwalter. I find myself very fortunate to have joined his group at UCSB as his first student. Jim has been a great mentor for me, and I am always inspired by his immense knowledge, his dedication to his students, and his smart and invaluable ideas. He has taught me a lot that I did not know before, and I find myself a better researcher thanks to him.

I am also thankful to Prof. Clint Schow, for his guidance and advises. Clint has taught me so much about optics and solving problems in the lab, and I am deeply grateful that I had the opportunity to work with him . I am also thankful to my other Ph.D. committee members, Prof. John Bowers and Prof. Jonathan Klamkin, for their contribution to my research and what I learned from them during meetings, talks, and collaborations on different projects. I would also like to thank Prof. Rodwell, who also has taught me a lot about microwave circuit design, and Dr. Roger Helkey for his insightful discussions on analog optical links.

Over the past five years I enjoyed working with so many talented students and researchers at UCSB. I would like to thank all the current and past members of RFIC group at UCSB. Dr. Kang Ning, who is a great friend and I really enjoyed working with on tape-outs and also talking about circuits and everything else. My friend Luis Valenzuela, who is always willing to help and I had the pleasure to collaborate with on the optical TX project. And all of my friends in our group, Dr. Cameron Hill, Ahmed Hamza, Hector Andrade, Dr. Hussam AlShammary, Mayank Kumar Singh, Ghazal Movaghar, Andrea Arias, Everett OMalley, Jeff Chien, Rohit Reddy Karnaty, Jonathan Tao, Jinesh Jhonsa, and Shu-Ming Chang. I would also like to thank members of Prof. Rodwell, Prof. Schow,

and Prof. Bowers labs who I had the pleasure of working with: Dr. Aditya Jain, who we worked together designing the RF photonic receiver, Takako Hirokawa, who helped me a lot with learning optical measurements, Dr. Paolo Pintus, Yujie Xia, Junqian Liu, Ahmed Ahmed, and Ali Farid. I also thank Dr. Seong-Kyun Kim and Dr. Rob Maurer who helped me with fundamentals of high-frequency measurements and learned how not to break a probe!

I am also grateful to my friends, who I enjoyed living in Santa Barbara with, Mohammad Javad, Mahnaz, Soheil, Neda, Saeid, Razieh, Farnood, Farnaz, Mahdi, Samira, Mehran, Fatemeh, Kasra, Razieh, Hedieh, Behnam, Setareh, and Amirali.

To my parents, Reza and Forouzan, who always supported me and been there for me, throughout my life. I owe them so much and any accomplishment I ever have is because of them. Also, I am grateful to my wonderful brothers for their support from overseas.

Finally, I owe a large debt of gratitude to my beloved wife Mitra, who has helped me with every step during these years at Santa Barbra. She always has been supportive and encouraging, and this work would not been possible without her. Also it is great that she is also a circuit designer and we can discuss circuits as well!

Curriculum Vitæ

Navid Hosseinzadeh

Education

2020	Doctor of Philosophy, Electrical and Computer Engineering, University of California, Santa Barbara
2014	Master of Science, Electrical Engineering, Sharif University of Technology, Tehran, Iran
2011	Bachelor of Science (Honors), Electrical Engineering , Babol Noshirvani University of Technology, Babol, Iran

Professional Employment

2015-2020	Graduate student researcher, Dept. of Electrical and Computer Engineering, University of California, Santa Barbara, CA
2019	Summer intern, PsiQuantum Corp., Palo Alto, CA

Publications

J6 **N. Hosseinzadeh**, K. Fang, L. Valenzuela, C. Schow, J. F. Buckwalter, "Co-design of CMOS Drivers and Silicon Photonic Mach-Zehnder Modulators for Hybrid and Monolithic Integrated Optical Transmitters," (in progress)

J5 **N. Hosseinzadeh**, A. Jain, R. Helkey and J. F. Buckwalter, "A Distributed Low-Noise Amplifier for Broadband Linearization of a Silicon Photonic Mach-Zehnder Modulator," submitted to IEEE Journal of Solid-State Circuits, (accepted with minor revision)

J4 T. Hirokawa, S. Pinna, **N. Hosseinzadeh**, A. Maharry, H. Andrade, J. Liu, T. Meissner, S. Misak, G. Movaghar, L. A. Valenzuela, Y. Xia, S. Bhat, F. Gambini, J. Klamkin, A. A. M. Saleh, L. Coldren, J. F. Buckwalter, and C. L. Schow, "Analog Coherent Detection for Energy Efficient Intra-Data Center Links at 200 Gbps per Wavelength," submitted to Journal of Lightwave Technology, (accepted with major revision)

C7 **N. Hosseinzadeh**, K. Fang, L. Valenzuela, C. Schow, J. F. Buckwalter, "A 50-Gb/s Optical Transmitter Based on Co-design of a 45-nm CMOS SOI Distributed Driver and 90-nm Silicon Photonic Mach-Zehnder Modulator," 2020 IEEE/MTT-S International Microwave Symposium (IMS), 2020

C6 L. Valenzuela, H. Andrade, **N. Hosseinzadeh**, A. Maharry, Clint Schow, J. F. Buckwalter, "A 2.85 pJ/bit, 52-Gbps NRZ VCSEL Driver with Two-Tap Feed-forward Equalization," 2020 IEEE/MTT-S International Microwave Symposium (IMS), 2020

J3 K. Ning, Y. Fang, **N. Hosseinzadeh** and J. F. Buckwalter, "A 30-GHz CMOS SOI Outphasing Power Amplifier With Current Mode Combining for High Backoff Efficiency and Constant Envelope Operation," in IEEE Journal of Solid-State Circuits, vol. 55, no. 5, pp. 1411-1421, May 2020.

J2 **N. Hosseinzadeh**, A. Jain, K. Ning, R. Helkey and J. F. Buckwalter, "A Linear Microwave Electro-Optic Front End With SiGe Distributed Amplifiers and Segmented Silicon Photonic Mach–Zehnder Modulator," in IEEE Transactions on Microwave Theory and Techniques, vol. 67, no. 12, pp. 5446-5458, Dec. 2019.

C5 **N. Hosseinzadeh**, A. Jain, K. Ning, R. Helkey and J. F. Buckwalter, "A 0.5-20 GHz RF Silicon Photonic Receiver with 120 dB•Hz2/3 SFDR using Broadband Distributed IM3 Injection Linearization," 2019 IEEE Radio Frequency Integrated Circuits Symposium (RFIC), Boston, MA, USA, 2019, pp. 99-102.

C4 **N. Hosseinzadeh**, A. Jain, K. Ning, R. Helkey and J. F. Buckwalter, "A 1 to 20 GHz Silicon-Germanium Low-Noise Distributed Driver for RF Silicon Photonic Mach-Zehnder Modulators," 2019 IEEE MTT-S International Microwave Symposium (IMS), Boston, MA, USA, 2019, pp. 774-777.

J1 A. Jain, **N. Hosseinzadeh**, X. Wu ; H. K. Tsang, R. Helkey, J. E. Bowers, J. F. Buckwalter, "A High Spur-Free Dynamic Range Silicon DC Kerr Ring Modulator for RF Applications," in Journal of Lightwave Technology, vol. 37, no. 13, pp. 3261-3272, July, 2019.

C3 **N. Hosseinzadeh**, A. Jain, R. Helkey and J. Buckwalter, "Sources of RF Intermodulation Distortion in Silicon Photonic Modulators," 2018 IEEE Avionics and Vehicle Fiber-Optics and Photonics Conference (AVFOP), Portland, OR, 2018, pp. 1-2.

C2 **N. Hosseinzadeh**, A. Jain, R. Helkey and J. F. Buckwalter, "RF silicon photonics for wideband, high dynamic range microwave and millimeter-wave signal processing," 2018 IEEE 18th Topical Meeting on Silicon Monolithic Integrated Circuits in RF Systems (SiRF), Anaheim, CA, 2018, pp. 41-44.

C1 **N. Hosseinzadeh** and J. F. Buckwalter, "A compact, 37% fractional bandwidth millimeter-wave phase shifter using a wideband lange coupler for 60-GHz and E-band systems," 2017 IEEE Compound Semiconductor Integrated Circuit Symposium (CSICS), Miami, FL, 2017, pp. 1-4.

Patents

2019 Analog Predistortion Linearization For Optical Fiber Communication Links (USPTO provisional)

Awards

2020 UC Santa Barbara ECE Dept. Herbert Kroemer dissertation fellowship

2018 UC Santa Barbara Graduate Division fellowship for AIM Photonics researchers

Abstract

Co-design of Electronic and Silicon Photonic Integrated Circuits for Microwave Photonics and Data-Center Communications

by

Navid Hosseinzadeh

Silicon photonics offer a low-cost platform for large-scale optical systems, and find applications in data-centers, long-haul optical networks, LiDAR, and RF/microwave photonics. RF photonic systems offer interference-tolerant, wideband radio systems in RF and millimeter-wave bands. This is feasible through analog optical links that take advantage of low loss and immune to electromagnetic interference fiber optical cables. Performance of such systems is characterized by spur-free dynamic range (SFDR). Most of current RF Photonic systems are based on $LiNbO_3$ Mach-Zehnder (MZM) modulators, which are expensive and difficult to fabricate in large volume. Silicon phonics, on the other hands, offer low cost low large scale integration, however the performance is below what $LiNbO_3$ technology offers.

In this work, fundamental sources of nonlinearity in Silicon photonics MZMs are analyzed and characterized, and methods and techniques are proposed to overcome the limitations in order to design high SFDR silicon photonic based optical RF receivers. First, A SiGe low-noise distributed driver is co-designed for the SiP MZM to linearize and extend the bandwidth over which the SFDR remains high, by focusing on improving NF of the receiver. The RoF transmitter achieves 1-20 GHz bandwidth and an SFDR of 109 $dB{\cdot}Hz^{2/3}$ at 11 GHz. This is the highest SFDR demonstrated for a SiP technology without incorporating predistortion. Next, a distributed silicon-germanium (SiGe) HBT-based low-noise amplifier (LNA) is co-designed for linearization with a Silicon phonics

MZM for a broadband RoF link. The SiGe LNA incorporates a distributed, tunable predistortion scheme that is inherently wideband and improves the third-order intercept point over an 18 GHz range. The assembled SiGe LNA and SiP MZM prototype demonstrates an SFDR as high as 120 dB·Hz$^{2/3}$ at 9 GHz, a 14 dB improvement over previous SiP RF components or RoF links, and a record among Silicon photonic MZM based RoF systems.

In the next part of dissertation, integration strategies of silicon photonics are compared for compact and efficient integrated optical transmitters with CMOS drivers, to be used in coherent intra-data center optical link. An integrated optical transmitter, based on a CMOS driver and a silicon photonic segmented MZM with travelling wave, that operates to 50 Gb/s is designed. The MZM consists of 4 traveling wave segments along a 3.2 mm length in a 90-nm Silicon Photonic technology. The broadband distributed amplifier is a pseudo-differential design with 3-stack driver stages to deliver sufficient voltage swing in a 45nm CMOS SOI technology. The optical eye is open to 50 Gb/s and indicates error-free operation to 30 Gb/s. The total circuit consumes 480 mW. Next, A fully integrated optical transmitter with 90-nm CMOS driver is presented. The novel design, based on a distributed amplifier merged in a travelling wave Mach-Zehnder modulator, maximizes area and bandwidth efficiency. Open optical eyes are measured up to 30 Gbps for the first run implementation.

The material in this dissertation has been partially appeared in the following publications:

- N. Hosseinzadeh, A. Jain, R. Helkey and J. F. Buckwalter, "A Distributed Low-Noise Amplifier for Broadband Linearization of a Silicon Photonic Mach-Zehnder Modulator," in IEEE Journal of Solid-State Circuits

- N. Hosseinzadeh, K. Fang, L. Valenzuela, C. Schow, J. F. Buckwalter, "A 50-Gb/s Optical Transmitter Based on Co-design of a 45-nm CMOS SOI Distributed Driver and 90-nm Silicon Photonic Mach-Zehnder Modulator," 2020 IEEE/MTT-S International Microwave Symposium (IMS), 2020

- N. Hosseinzadeh, A. Jain, K. Ning, R. Helkey and J. F. Buckwalter, "A Linear Microwave Electro-Optic Front End With SiGe Distributed Amplifiers and Segmented Silicon Photonic Mach–Zehnder Modulator," in IEEE Transactions on Microwave Theory and Techniques, vol. 67, no. 12, pp. 5446-5458, Dec. 2019.

- N. Hosseinzadeh, A. Jain, K. Ning, R. Helkey and J. F. Buckwalter, "A 0.5-20 GHz RF Silicon Photonic Receiver with 120 dB•Hz2/3 SFDR using Broadband Distributed IM3 Injection Linearization," 2019 IEEE Radio Frequency Integrated Circuits Symposium (RFIC), Boston, MA, USA, 2019, pp. 99-102.

- N. Hosseinzadeh, A. Jain, K. Ning, R. Helkey and J. F. Buckwalter, "A 1 to 20 GHz Silicon-Germanium Low-Noise Distributed Driver for RF Silicon Photonic Mach-Zehnder Modulators," 2019 IEEE MTT-S International Microwave Symposium (IMS), Boston, MA, USA, 2019, pp. 774-777.

- N. Hosseinzadeh, A. Jain, R. Helkey and J. Buckwalter, "Sources of RF Intermodulation Distortion in Silicon Photonic Modulators," 2018 IEEE Avionics and Vehicle Fiber-Optics and Photonics Conference (AVFOP), Portland, OR, 2018, pp. 1-2.

- N. Hosseinzadeh, A. Jain, R. Helkey and J. F. Buckwalter, "RF silicon photonics for wideband, high dynamic range microwave and millimeter-wave signal processing," 2018 IEEE 18th Topical Meeting on Silicon Monolithic Integrated Circuits in RF Systems (SiRF), Anaheim, CA, 2018, pp. 41-44.

Contents

List of Figures

List of Tables

Chapter 1

Introduction

The exponential expansion of mobile communication networks, result of their continuous growth in both number of users and bandwidth per user, has led to increase in demand for more efficient usage of available spectrum. Wireless communication networks, generation after generation, evolve around maximizing spectrum efficiency to address growing number of applications and bandwidth requirements. For example, based on the annual report by Cisco, global Wi-Fi's average connection speed is predicted to increase by 200% to 91.6 Mbps in 2023, from 30.3 Mbps in 2018. For Mobile networks this jump is even larger than 200%, and it is projected average connection speed will get to 43.9 Mbps in 2023, compared to 13.2 Mbps in 2018 [1]. These all require drastic changes in how frequency spectrum is used, and also pushes networks toward higher frequencies where more bandwidth is available. Systems with wider bandwidth can be designed at higher frequencies, as required fractional bandwidth is smaller as we move upper on the frequency axis. The next generation of wireless communication systems rely on wideband signals, and at higher carrier frequencies than what current generation uses. Multiple antennas are required in such systems to achieve spatial multiplexing, beam forming and supporting multiple frequency bands [2–4]. Emerging millimeter-wave networks based

on multi-input multi-output (MIMO) systems are more distributed than current RF systems and require transceivers at different locations to cover a small cell environment with wireless signal. This is due to higher path-loss and higher frequencies, which dictates to increase number of transceivers in order to get the same coverage as what current RF frequency system do without increasing transmitter power level, and nature of line of sight communications as any physical object can block the signal. RF signal distribution in such multi-antenna environments at high-frequencies is challenging considering the high signal path loss and packed frequency spectrum.

On the other end of networks, data centers are facing a constant increasing power consumption as they are expanding rapidly to adapt with higher data storage/processing demand. In addition, cloud computing has increased data centers power consumption as growing number of applications are turning toward using cloud power for computing. Date centers' electricity usage is projected to increase 15-fold by 2030, which will be 8% of global electricity demand by the time [5]. A lot of efforts have been made to keep electricity usage in data centers constant. New generation of computing servers has played a big role so far. Another part that researchers and industries are working on is to find more efficient intra-data center communication networks. As data demand is increased, a higher portion of data transmission are happening inside data-centers rather than between servers and users. Traditionally, electrical connections are used for short distances and optical links, due to much lower loss of fiber optical links compared to electrical cables, are used for distant servers. So far, the increased data traffic in data centers has been addressed by faster wire-line links. At some point, however, required bandwidth and demand for low power consumption has pushed networks to consider using fiber optical links to maximize efficiency, even for short-range communications.

Integration of electronics and photonics, feasible through recent and ongoing advances in silicon photonics technology, has paved the way for novel efficient wired and wireless

communication systems. The applications ranges from highly efficient optical links for intra-data center communication, to LiDAR systems for autonomous vehicles and imaging, and to microwave photonics and Radio-over-Fiber systems for 5G communication links and low loss RF signal distribution. Advances in silicon photonics, aimed to follow the same path as the silicon based electronics toward achieving large scale low cost production of highly integrated systems, has lead to novel electro-optical systems that are capable of challenging traditionally used expensive and bulky III-V and $LiNBO_3$ based photonics. Most reported high performance Radio-over-Fiber (RoF) links, in both academia research and industry, are predominantly based on $LiNBO_3$ technology.

1.1 RF Photonic Systems

RF photonic systems find applications in antenna remoting and beam forming for phased-array systems and can be used for signal distribution in millimeter-wave networks. Fig. 1.1 shows an example environment with different type of users in a wireless network. RF signal distribution can be enhanced by using RF photonic based network systems. RoF link can be used as the connecting link between two wireless network towers, or to distribute internet connection to an entire building using a single wireless connection for all.

RF photonic systems based on silicon photonics (SiP) enable low-cost high-yield integrated optical links. Mach-Zehnder Modulator (MZM) is widely used as the modulator in both analog and digital optical links mainly due to its wide bandwidth and simple design. The key challenge in RF photonic link design is the limited spurious-free dynamic range (SFDR) defined by (1.1) and shown in Fig, [6] which is due to intrinsic nonlinearity of MZM. SFDR is defined by:

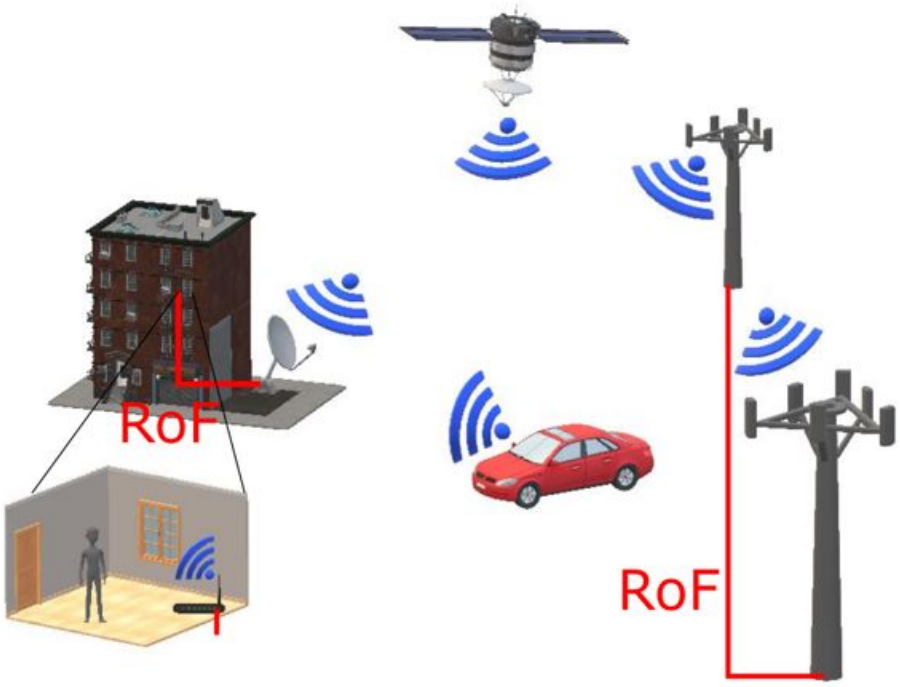

Figure 1.1: RF signal distribution using RF photonic links for wireless communications networks.

$$SFDR = \frac{2}{3}\Big(IIP3 + 174 - NF - 10\log BW\Big), \tag{1.1}$$

where NF is the noise figure, and IIP3 is the third order input intercept point.

Another application for microwave photonic links is in MIMO and beamforming systems [7] for radar imaging and tracking. At high frequencies with the goal of being immune to electromagnetic interference, signal distribution and collection to support large number of antennas is only possible with fiber optics. Fig. 1.2 and example MIMO imaging system based on optical interconnects. The optical links here collect the signals from receiver and transfer them for processing and control to the central processing block. Here Mach-Zehnder modulator is used to convert the electrical signals to optical

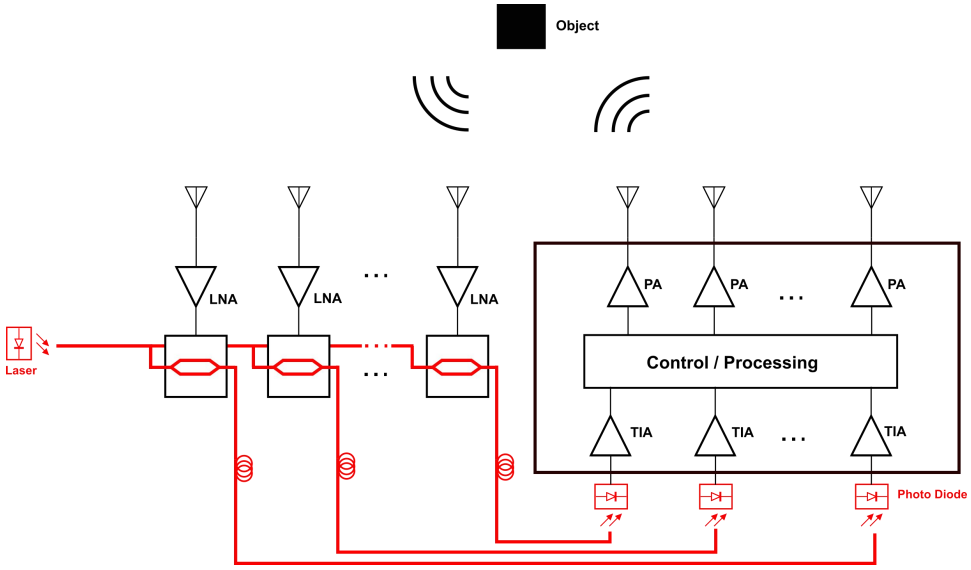

Figure 1.2: Illustration of a millimeter-wave electro-optical MIMO imaging system.

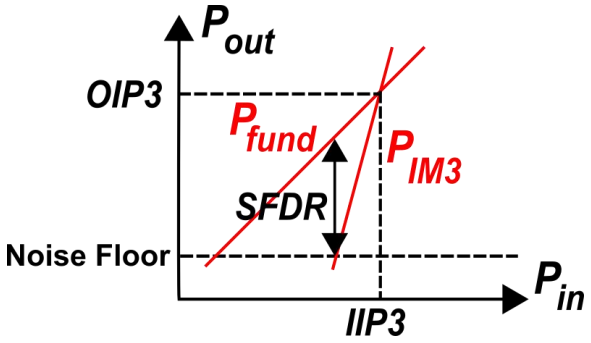

Figure 1.3: Spurious-free dynamic range (SFDR) of an RF system limited by third order nonlinearity

and on the receiving side of the link, photo-receivers are used to perform the opposite conversion.

As 5G wireless networks operate over a larger range of frequency bands, more emphasis is placed on utilizing multiple bands and not only sub-6 GHz bands but also microwave/millimeter-wave bands. The RF loss of distributing signals from antennas to signal processing receivers increases at higher frequency and higher directionality in mm-wave signals increases the potential for blockage. RoF links were initially developed for optical-domain RF signal distribution in phased-array antennas [8] due to advan-

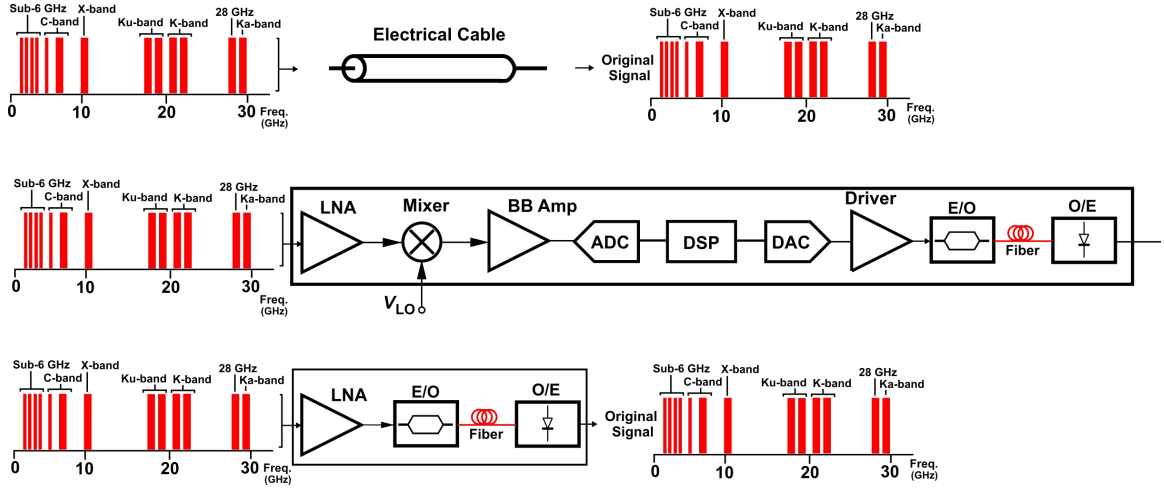

Figure 1.4: Illustration of three methods for RF signal distribution: traditional electrical link based on coaxial cables, digital optical link based on amplitude modulation (NRZ, PAM4), and RoF link as a low loss method for multi-band RF signal distribution

tages for lossless signal distribution over a wide frequency range. In a RoF system, an electro-optical modulator converts the microwave signal to optical which is transmitted over optical fibers. Here, an RF signal is narrowband and multiple signals, depending on linearity and bandwidth of the optical modulator, can be carried over a single fiber simultaneously as shown in Fig. 1.4. This figure also compares the analog optical link against a simple electrical link and and also a digital optical link. At high frequencies, interference sensitive applications, and for long distance communications, the electrical link will not support the needs anymore. Digital optical links, widely used in fiber optical communication systems, work well if the goal is to get base band signal at the end of the link. However, that's not the case for signal distribution to multiple antennas in a low power way. The wideband RoF link is proposed to capture and distribute signals from different cellular and satellite frequency bands in a multifunctional receiver. In the presence of strong blockers, such a wideband receiver demands high linearity and low noise figure as characterized with SFDR.

The RoF link illustrated in Fig. 1.5 has a low-noise amplifier to receive the RF signal

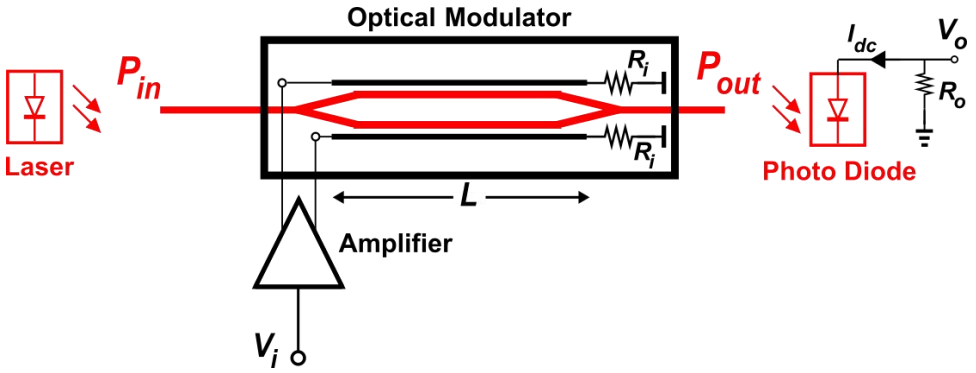

Figure 1.5: Illustration of RoF transmitter based on Mach-Zehnder modulator and driven by a low noise driver

from the antenna and drive the modulator to produce the electro-optic (E/O) conversion. The signal is distributed to a photodetector where the optical carrier produces an RF current that is linearly proportional to the input RF signal. The SFDR of RoF links is limited by nonlinearity in the E/O and O/E conversions and noise [9]. An LNA improves the noise figure of the RoF but requires a wideband, high linearity circuit design.

1.2 Coherent Optical links

There is a growing interest in using coherent optical communication for intra-data center communications. A simple block-diagram of a coherent optical link, consisted of a dual polarization transmitter and receiver, is illustrated in Fig. 1.6 [10]. Compared to traditionally used direct detection based links, coherent optical links are scalable to higher data rates through higher-order modulation formats and orthogonal polarization, have lower link power due to additional link budget, adapt with the loss of active photonic switching without requiring additional optical gain blocks, have a more relaxed optical crosstalk requirement between channels due to higher selectivity, are lower in power and complexity compared to current digital coherent technology that relies heavily on digital signal processing (DSP), and take advantage of Optical Phase Lock Loop (OPLL) to

perform carrier recovery rather than power hungry DSP [11, 12]. As shown in Fig. 1.6, by using orthogonal modulation we can increase the bit-rate per fiber. In the figure, QPSK modulation is utilized and bit is doubled per fiber. This can be further increased by using higher order modulation formats, but that will increase sensitivity and linearity requirements of the system. Another degree of freedom that can be employed to double the bit-rate is using orthogonal polarization on the electromagnetic beam. This can be done by using Polarizations Beam Combiner (PBC) and Polarization Beam Splitter (PBC), as is shown in Fig. 1.6. Further increase of bandwidth per fiber possible by using Wavelength Division Multiplexing (WDM) [11].

Silicon photonics (SiP) offer a low-cost platform for large-scale optical systems used in data centers. However, high-speed electro-optical (E/O) modulation requires separate electronic and photonic device technologies. The SiP Mach-Zehnder Modulator (MZM) is constructed with p-n junction phase shifters that produce a 180 degree phase shift at the V_π voltage. Due to the relatively low $V_\pi L$ product for SiP MZMs (˜1.5 V-cm), the driver should produce around 3-5 Vpp differential voltage swing. All of these considerations prompt to co-design electronic and photonics and take advantage of the flexibility within the co-design approach.

1.3 Contributions and Organization

In this dissertation, novel electro-optical systems are developed for both RF photonic and coherent optical systems. First, sources of nonlinearity in MZM are analysed and a frequency dependent nonlinear model for MZM is developed for the first time. First integrated silicon photonic MZM and SiGe driver is reported. A wideband photonic RF receiver is designed to achieve high SFDR by co-designing a SiGe low noise driver and a silicon photonic MZM. Next, an analog predistortion method is proposed to linearize

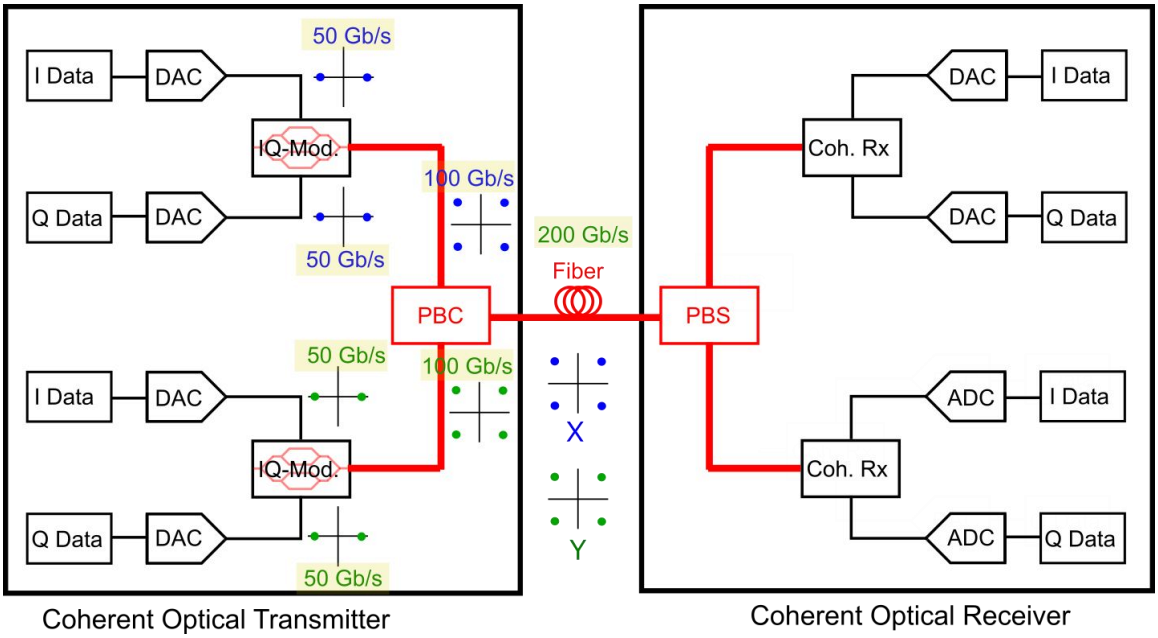

Figure 1.6: Illustration of a simple block-diagram of a coherent optical link, consisted of a dual polarization transmitter and receiver

the MZM. The predistorter driver in co-designed with the Silicon Photonic MZM and achieves record SFDR among reported silicon photonic MZMs, with BW extending to 20 GHz.

Next, for coherent optical systems, a distributed CMOS driver is co-designed with a silicon photonic segmented MZM with novel architecture, for the first time. Finally, a novel architecture for fully integrated optical transmitters is proposed and a prototype is designed and implemented in 90 nm CMOS technology. The novel monolithically integrated optical transistor is based on a distributed amplifier merged in a travelling-wave Mach-Zehnder modulator. The organization of this dissertation is as follows.

Chapter 2 analyzes the underlying source of nonlinearity in SiP Mach-Zehnder Modulator (MZM) and demonstrates fundamental limitations on intermodulation distortion. First operation of MZM is mathematically analyzed with having the goal of deriving a frequency dependent nonlinear model in mind. Subsequently, a nonlinear model is de-

veloped for the MZM for the first time that includes three major source of nonlinearity. Using cascade analysis for cascaded nonlinear blocks, IIP3 and SFDR as a function of frequency and different MZM design parameters are found. These results are used in next chapters to design an RF photonic receiver with an enhanced SFDR.

Chapter 3 discusses design of the novel SiGe driver for co-integration with a segmented MZM is silicon photonics. It presents detailed design steps taken to maximize bandwidth and dynamic range. The driver is based on a distributed amplifier in 130 SiGe BiCMOS technology. Next, measurement results are presented for the assembled SiP MZM and SFDR of the RoF link is characterized. It shows comparable dynamic range to bulky $LiNbO_3$ and III-V MZM. Maximum SFDR of 120dB·$Hz^{2/3}$ is measured with bandwidth of 1-20 GHz.

Chapter 4 demonstrates a distributed silicon-germanium (SiGe) HBT-based low-noise amplifier (LNA) co-designed for linearization with a SiP MZM for a broadband RoF link. A novel linearization technique is proposed and utilized to further extend the dynamic range of the MZM. The SiGe LNA incorporates a distributed, tunable predistortion scheme that is inherently wideband and improves the third-order intercept point over an 18 GHz range. The assembled SiGe LNA and SiP MZM prototype demonstrates an SFDR as high as 120 dB·$Hz^{2/3}$ at 9 GHz, a 14 dB improvement over previous SiP RF components or RoF links.

Chapter 5 presents an integrated optical driver and MZM that operates to 50 Gb/s. The MZM consists of 4 traveling wave segments along a 3.2 mm length in a 90-nm Silicon Photonic (SiP) technology. The broadband distributed amplifier is a pseudo-differential design with 3-stack driver stages to deliver sufficient voltage swing in a 45nm CMOS SOI technology. The optical eye is open to 50 Gb/s and indicates error-free operation to 30 Gb/s. The total circuit consumes 480 mW.

Chapter 6 Discusses design and implementation of a high-speed fully differential

driver and MZM using a co-design approach in 90nm 9WG technology. A novel architecture is proposed that merges a distributed amplifier into a travelling wave Mach-Zehnder modulator. Driver has a differential input and drives a transmission line, which is also anode terminal for p-n junction phase shifters. It achieve open eyes up to 30 Gbps.

1.4 Permissions and Attributions

Chapter 2

Sources of Nonlinearity in Mach-Zehnder Modulator

2.1 Introduction

Silicon photonics (SiP) offer a low-cost platform for large-scale RF system integration. Yet, the SFDR of a SiP Mach-Zehnder modulator (MZMs) is significantly worse than $LiNbO_3$ or InP modulators [16]. SiP devices are characterized by a relatively weak electro-optic plasma dispersion effect and the parasitics associated with long devices. Generally, a SiP MZM has a $V_\pi L$ product of around 1.5 V-cm, suggesting that relatively long devices are required to achieve high RF gain. However, long devices result in reduced third-order input intercept point (IIP3) and significant parasitics to drive the long traveling-wave electrode. In this chapter, underlying sources of nonlinearity in MZM are analyzed and characterized and a frequency dependant nonlinear model for the MZM is derived.

2.2 SFDR of Mach-Zehnder Modulators

Dynamic range of a system is an important metric that shows how the system handles different input signal levels. For narrow-band systems where inter-modulation components from out-of-band or in-band limit the dynamic range, SFDR is used. High SFDR demands achieving minimum NF with the highest IIP3. The SFDR of an RF circuit is characterized by

$$SFDR = \frac{2}{3}(IIP3 - MDS), \tag{2.1}$$

where MDS is the input minimum detectable signal, $MDS = -174 + NF + 10\log(BW)$, for a receiver noise figure (NF) and bandwidth (BW). To normalize the SFDR for a given signal, the bandwidth is assumed to be 1 Hz and SFDR will have units of dB·Hz$^{2/3}$. Improving the SFDR requires improving the IIP3 while reducing the NF.

2.3 RF Modulation of an MZM

The optical power transmission through an MZM with arms of length L, labeled A and B in Fig. 2.1, can be found assuming each arm has a propagation constant, $\gamma_{A,B} = \alpha_{A,B} + j\beta_{A,B}$, where α is the attenuation per unit length and β is the phase per unit length. If we assume the propagation constant has a linear dependence on the applied voltage, then $\alpha = a_0 + a_1 V$ and $\beta = b_0 + b_1 V$. The applied voltage can be considered as a DC and RF signal, $V_{A,B} = V_{Q,(A,B)} \pm v_i$ generated from an input resistance R_i. The electric field in a fiber can be written as:

$$E_{in}(t) = \sqrt{\frac{2P_{in}}{A}}(\frac{\mu}{\epsilon})^{\frac{1}{4}}\ cos(\omega_L t) \tag{2.2}$$

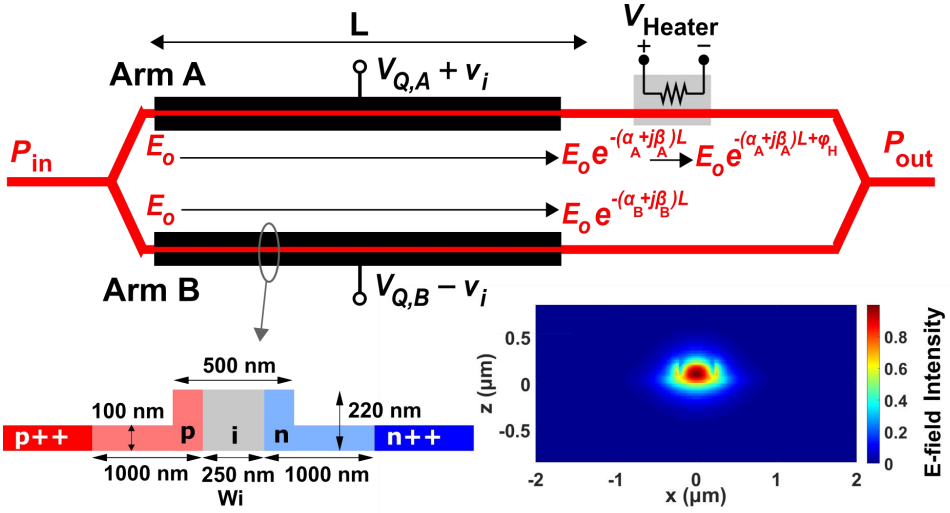

Figure 2.1: Simplified model of the Mach-Zehnder modulator (top), Cross sectional view of the p-i-n junction phase shifter (bottom left), and normalized simulated E-field intensity of the p-i-n junction phase shifter.

where P_{out} is the laser power. The following equation can be found for the power received by photo diode:

$$P_{out} = \frac{A}{2}(\frac{\mu}{\epsilon})^{\frac{1}{2}} E_{out} E_{out}^{\star} \tag{2.3}$$

Considering a heating phase shift ϕ_H, the optical transmission through the MZM can be found by the adding electric fields at the output of each arm, shown in Fig. 2.1. E_{out} can be found at the output of MZM:

$$E_{out} = \frac{E_{in}}{\sqrt{2}}(e^{-\gamma_A L} e^{j\phi_H} + e^{-\gamma_B L}) \tag{2.4}$$

Then corresponding optical power can be found from (2.4):

$$\frac{P_{out}}{P_{in}} = \frac{e^{-\alpha_{DC} L}}{2}\big(\cosh(2a_1 L v_i) + \cos(2b_1 L v_i - \phi_{DC})\big), \tag{2.5}$$

where the optical DC attenuation is $\alpha_{DC} = 2a_0 + a_1(V_{Q_A} + V_{Q_B})$ and phase change is $\phi_{DC} = \phi_H - b_1(V_{Q,A} - V_{Q,B})$.

The cosine term in (2.5) is modulated by an RF signal $v_i = V\cos(\omega t)$ and is simplified with a Jacobi-Anger expansion.

$$\begin{aligned}\cos(2b_iLv_i - \phi_{DC}) =&[J_0(2b_1VL) + 2\sum_{n=1}^{\infty}(-1)^n J_{2n}(2b_1VL)\cos(2n\omega t)]\cos\phi_{DC} \\ &+ [2\sum_{n=1}^{\infty}(-1)^n J_{2n-1}(2b_1VL)\cos((2n-1)\omega t)]\sin\phi_{DC} \end{aligned} \tag{2.6}$$

where $J_n(x)$ is the n-th Bessel function of the first kind. The single tone input generates odd harmonics in the optical power of the MZM.

$$P_{2n-1} = P_{in}e^{-\alpha_{DC}L}J_{2n-1}(2\pi\frac{V}{V_\pi})\sin\phi_{DC}. \tag{2.7}$$

Note, the coefficients in (2.6) indicate that even harmonics are eliminated at the quadrature bias, i.e. $\phi_{DC} \simeq \frac{\pi}{2}$.

2.3.1 E/O Gain

From (2.5), The electro-optical (RF) gain of MZM is approximated using a small-signal approximation of the Bessel function and characterizing the modulation of the optical power with the applied RF voltage. i.e. $G_{EO} = \frac{dP_{out}}{dv_i}$.

$$G_{EO} = P_{in}e^{-\alpha_{DC}L}b_1L\sin\phi_{DC} \tag{2.8}$$

The MZM achieves maximum gain near the quadrature bias and is set with the heating phase ϕ_H. The ϕ_{DC} might not be exactly $\frac{\pi}{2}$ due to fact that the nonlinear absorption and phase shift are related in the PN junction (e.g. $2a_1v_i \propto \Delta\phi$) [17]. When the attenuation

loss is low, the gain is approximately $G_{EO} = P_{in} b_1 L \simeq \pi \frac{P_{in}}{V_\pi}$ where we characterize the MZM modulation efficiency by $b_1 V_\pi L = \pi$ or the voltage required to induce a π phase shift.

2.3.2 O/E Gain

We will assume a linear receiver is available that converts the optical signal to an electrical voltage through an ideal photodetector (PD) with responsivity $\Re$ in units of A/W [18].

$$G_{OE} = \Re R_o \tag{2.9}$$

R_o is the output resistance of the PD. The product of $G_{EO} G_{OE}$ is the RoF link gain, i.e. $G_{ROF} = \pi \frac{I_{DC} R_o}{V_\pi} e^{-\alpha_{DC} L}$ where $I_{DC} = P_{IN} \Re$ is the DC current of the PD. For a low-loss SiP MZM with V_π of 10 V and PD biased at 1 mA both terminated in 50 Ω, the RoF gain is around -24 dB. The $V_\pi L$ product of SiP is around 1.5 V-cm suggesting that a reduction in V_π requires long integrated devices. Therefore, an RF amplifier is useful to compensate for the low RF gain in a SiP process.

2.3.3 Two Tone Analysis

To calculate the third-order intermodulation distortion (IM3), two tones are applied, $v_i = V(\cos(\omega_1 t) + \cos(\omega_2 t))$. Using (2.5), the cosine term can be rewritten as:

$$
\begin{aligned}
cos(2b_iLv_i - \phi_{DC}) = &\cos(2b_1LVcos(\omega_1 t))\cos(2b_1LVcos(\omega_2 t))\cos(\phi_{DC}) \\
&- sin(2b_1LV\cos(\omega_1 t))sin(2b_1LVcos(\omega_2 t))\cos(\phi_{DC}) \\
&- sin(2b_1LV\cos(\omega_1 t))\cos(2b_1LVcos(\omega_2 t))\sin(\phi_{DC}) \\
&- cos(2b_1LV\cos(\omega_1 t))\sin(2b_1LV\cos(\omega_2 t))\sin(\phi_{DC})
\end{aligned} \tag{2.10}
$$

and applying the Jacobi-Anger expansion, this can be expanded as:

$$
\begin{aligned}
cos(\phi_B - \phi_A - \phi_H) = &\left(J_0(2b_1V) + 2\sum_{n=1}^{\infty}(-1)^n J_{2n}(2b_1V)\cos(2n\omega_1 t)\right) \times \\
&\left(J_0(2b_1V) + 2\sum_{n=1}^{\infty}(-1)^n J_{2n}(2b_1V)\cos(2n\omega_2 t)\right)\cos\theta_B
\end{aligned} \tag{2.11}
$$

$$
\begin{aligned}
- &\left(2\sum_{n=1}^{\infty}(-1)^n J_{2n-1}(2b_1V)\cos((2n-1)\omega_1 t)\right) \times \\
&\left(2\sum_{n=1}^{\infty}(-1)^n J_{2n-1}(2b_1V)\cos((2n-1)\omega_2 t)\right)\cos\theta_B
\end{aligned} \tag{2.12}
$$

$$
\begin{aligned}
+ &\left(2\sum_{n=1}^{\infty}(-1)^n J_{2n-1}(2b_1V)\cos((2n-1)\omega_1 t)\right) \times \\
&\left(J_0(2b_1V) + 2\sum_{n=1}^{\infty}(-1)^n J_{2n}(2b_1V)\cos(2n\omega_2 t)\right)\sin\theta_B
\end{aligned} \tag{2.13}
$$

$$
\begin{aligned}
+ &\left(J_0(2b_1V) + 2\sum_{n=1}^{\infty}(-1)^n J_{2n}(2b_1V)\cos(2n\omega_1 t)\right) \times \\
&\left(2\sum_{n=1}^{\infty}(-1)^n J_{2n-1}(2b_1V)\cos((2n-1)\omega_2 t)\right)\sin\theta_B
\end{aligned} \tag{2.14}
$$

Using equation above, the power of the IM3 tone at $2\omega_2 - \omega_1$ can be found as:

$$P_{IM3} = P_{in}e^{-\alpha_{DC}L}J_2(2\pi\frac{V}{V_\pi})J_1(2\pi\frac{V}{V_\pi})\sin(\theta_{DC}) \tag{2.15}$$

Consequently, the IIP3 of the MZM is determined when $P_{IM3} = P_1$ from (2.7). Therefore,

$$IIP3_{VP} = \frac{\sqrt{2}V_\pi}{\pi}. \tag{2.16}$$

Notably, the $IIP3_{VP}$ is around 20 dBm for a V_π of 10 V. The OIP3=IIP3 G_{EO} of the MZM is an optical power and is $\sqrt{2}P_{in}$.

2.3.4 Noise Figure of the RoF Link

In the absence of an LNA, the noise factor of an RoF link has been previously derived in [18].

$$F = 1 + \frac{V_\pi^2}{\pi^2 R_i kT}\Big(\frac{kT}{I_{DC}^2 R_o} + \frac{2q}{I_{DC}} + RIN\Big) \tag{2.17}$$

where R_i is the input resistance, k is Boltzmann's constant, q is the charge of an electron, T is temperature, and RIN is the relative intensity noise of the laser. The first term in parenthesis is the thermal noise contribution of R_o. The second term is the shot noise of the PD. The third term is the contribution of laser noise. When the RoF link is limited by R_o, the F is approximated as

$$F \approx \frac{1}{G_{RoF}^2}\frac{R_o}{R_i} \tag{2.18}$$

In this limit, the noise figure ($NF = 10\log(F)$) increases with reduced RoF link power gain and long modulators with lower V_π have lower NF.

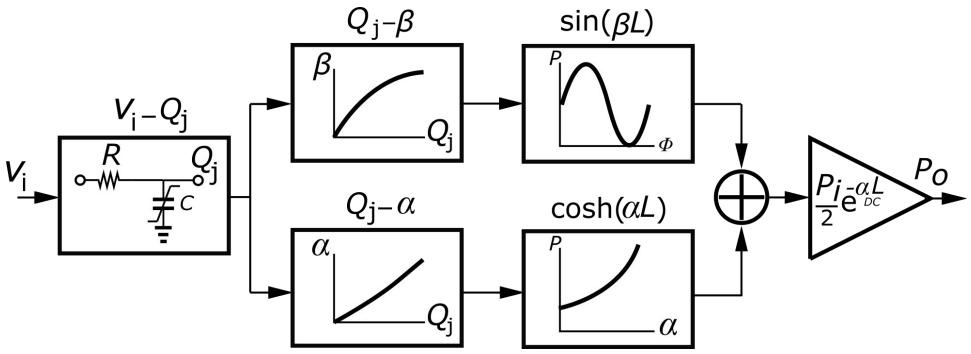

Figure 2.2: Model of nonlinear distortion in the SiP MZM

2.3.5 SFDR of RoF Link

As has been demonstrated, the design of an MZM trades IIP3 and NF. For the R_o-limited NF, the SFDR can be found from (2.18) and using $SFDR = \left(\frac{OIP3}{N_{out}BW}\right)^{2/3}$, where N_{out} is noise power spectrum at PD output:

$$SFDR \approx (\frac{IIP3^2_{MZM}G^2_{RoF}}{4kTR_o})^{2/3}, \tag{2.19}$$

The product of $IIP3_{MZM}$ from (2.16) and the RoF link gain is independent of V_π. Most importantly, this predicts that the SFDR is constant over frequency.

However, experimental measurement of SFDR in integrated MZMs reveals reduction at high frequency. Moreover SiP technologies do not offer similar SFDR as III-V materials. In the following section, we discuss the frequency dependence of SFDR of the MZM as well as the reasons for reduced SFDR in SiP devices.

The relatively low RF gain and high NF of the SiP MZM suggests that an LNA should offset the gain of the RoF link and compensate the contribution of RoF noise.

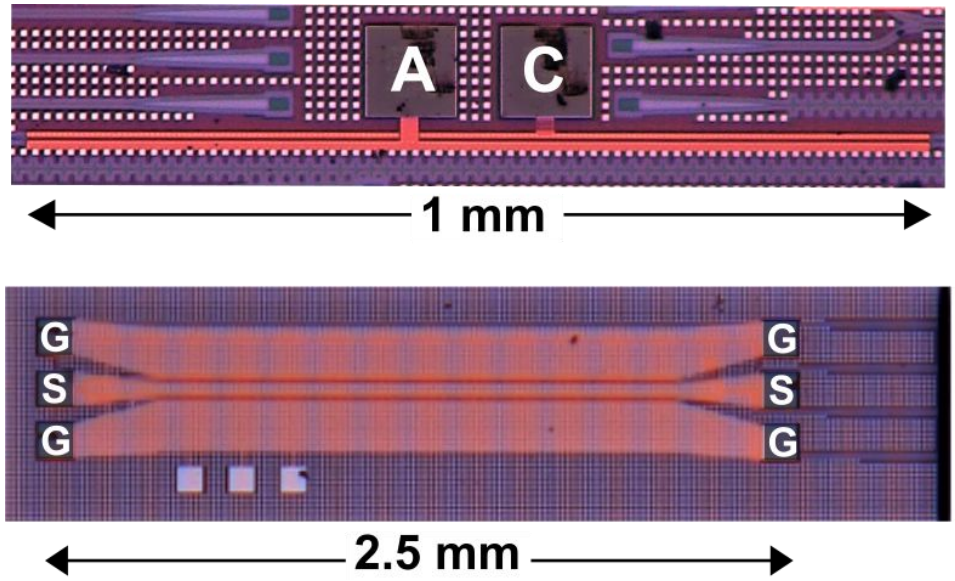

Figure 2.3: Chip micro-photograph of the 1 mm long p-i-n diode in AIM silicon photonics process with anode and cathode labeled (top), and micro-photograph of an unbalanced MZM in the same technology (bottom).

2.4 SFDR of Silicon Photonic MZM

Silicon photonic (SiP) devices generate optical phase shift through plasma dispersion introduced at a reverse-biased p-i-n junction. The carrier density in the waveguide causes a nonlinear phase and amplitude shift. Therefore, the linearity of the depletion region and its optical phase shift is a further IIP3 limitation beyond the MZM response found in (2.16). Here, we will consider the nonlinear capacitance as a function of voltage (C-V) and the linearity of the optical phase and attenuation as a function of voltage [19].

Fig. 2.2 illustrates an RF model for a SiP device that extends the result from (2.5) where distortion was generated based on the sum of contributions from the attenuation ($\cosh(\alpha L)$) and phase shift ($\sin(\beta L)$). In these paths, the attenuation and phase constant is a nonlinear function of the junction charge, Q_j. Furthermore, the applied RF voltage modulates the junction voltage of the p-i-n junction of the optical waveguide to change Q_j. In the following subsections, we analyze the contribution of each mechanism.

2.4.1 C-V Nonlinearity

We develop a Volterra series, assuming an RC time constant limit, to characterize the nonlinearity of a p-i-n diode [20]. The junction capacitance of the diode is :

$$C(v) = \frac{C_{J0}}{\left(1 - V_{A,B}/V_{bi}\right)^m}, \tag{2.20}$$

where C_{J0} is the zero-bias junction capacitance, V_{bi} is the built-in potential, and m is the grading coefficient of the junction. The capacitance can be expressed as a polynomial in terms of the junction voltage.

$$C(v) = C_0 + C_1 v_j + C_2 v_j^2 + ... \tag{2.21}$$

where $C_0 = C(V_Q)$, $C_1 = -C_0 \frac{m}{(1-V_Q/V_{bi})^{m+1}}$, and $C_2 = C_0 \frac{m(m+1)}{(1-V_Q/V_{bi})^{m+2}}$. Given the source resistance, R_i of the MZM, the junction voltage is given by the model in Fig. 2.2 and can be found using a Volterra analysis [20]. The junction voltage is

$$\begin{aligned} v_j &= A_1(j\omega_a) \circ v_i + A_2(j\omega_a, j\omega_b) \circ v_i^2 \\ &+ A_3(j\omega_a, j\omega_b, j\omega_c) \circ v_i^3 + ... \end{aligned} \tag{2.22}$$

The calculation for the Volterra coefficients are provided in Appendix A. The Volterra series introduces a frequency dependence to the IM3. For $\omega_a = \omega_b = \omega_1$, $\omega_c = -\omega_2$, and $\omega_1 \simeq \omega_2$,

$$\begin{aligned} IM3 &= \frac{3}{4} \frac{|A_3(j\omega_1, j\omega_1, -j\omega_2)|}{|A_1(j\omega_1)|^2 |A_1(j\omega_2)|} V^2 \\ &= \frac{3}{4} \omega_1 R_i C_2 \sqrt{\frac{1 + \omega_1^2 R_i^2 (\frac{C_1^2}{C_2} + 2C_0)^2}{1 + 5\omega_1^2 R_i^2 C_0^2 + 4\omega_1^4 R_i^4 C_0^4}} V^2. \end{aligned} \tag{2.23}$$

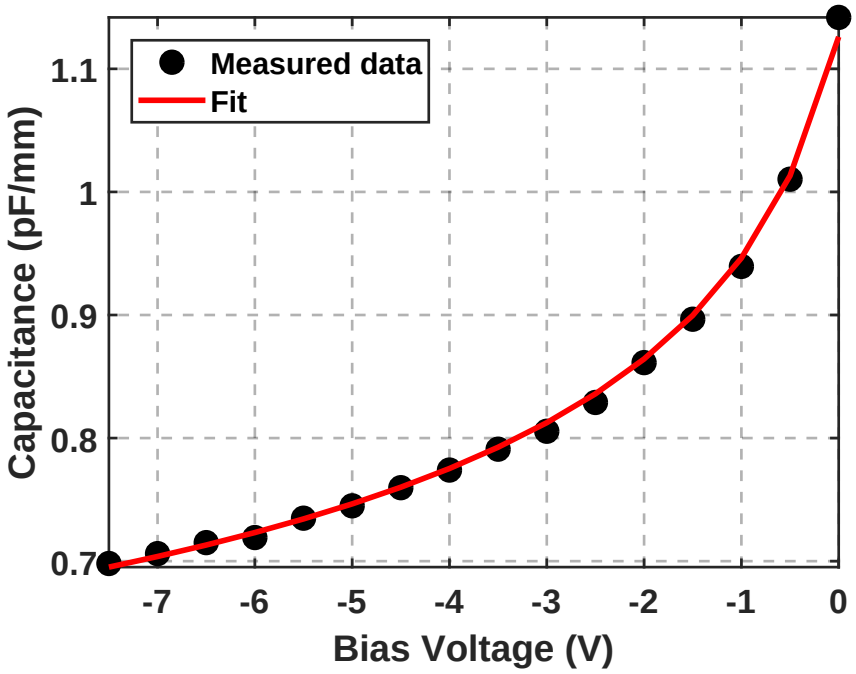

Figure 2.4: Normalized measured capacitance of a 1-mm long p-i-n diode in Silicon Photonics process and curve fit.

The IIP3 of the CV nonlinearity is found from $|IM3| = 1$.

$$IIP3_{VC} = \sqrt{\frac{4}{3\omega_1 R_i C_2}} \sqrt[4]{\frac{1 + 5\omega_1^2 R_i^2 C_0^2 + 4\omega_1^4 R_i^4 C_0^4}{1 + \omega_1^2 R_i^2 (\frac{C_1^2}{C_2} + 2C_0)^2}} \tag{2.24}$$

At low frequency, the IIP3 decreases with frequency according to $\sqrt{\frac{1}{\omega_1 R_i C_2}}$. At high frequency, the IIP3 approaches a lower limit at

$$IIP3_{VC\infty} = \sqrt{\frac{8C_0^2}{3(C_1^2 + 2C_0 C_2)}} \tag{2.25}$$

Most notably, the IIP3 at high-frequency is independent of the source resistance and MZM length. Comparing this limit to $IIP3_{VP}$ in (2.16), reducing the length of the

MZM to increase V_π would not result in an IIP3 improvement. The critical L would be reached when $IIP3_{VP} = IIP3_{VC\infty}$.

$$L_{SEG} = \frac{\sqrt{2}}{\pi b_1 IIP3_{CV\infty}} \tag{2.26}$$

This insight is the primary motivation for the use of a segmented structure for the MZM and a corresonding segmented modulator driver. If the critical length of the segment is chosen from (2.26), the number of segment is determined by bandwidth or power consumption constraints. Estimating $IIP_{CV\infty}$ allows us to characterize the optimal segment length.

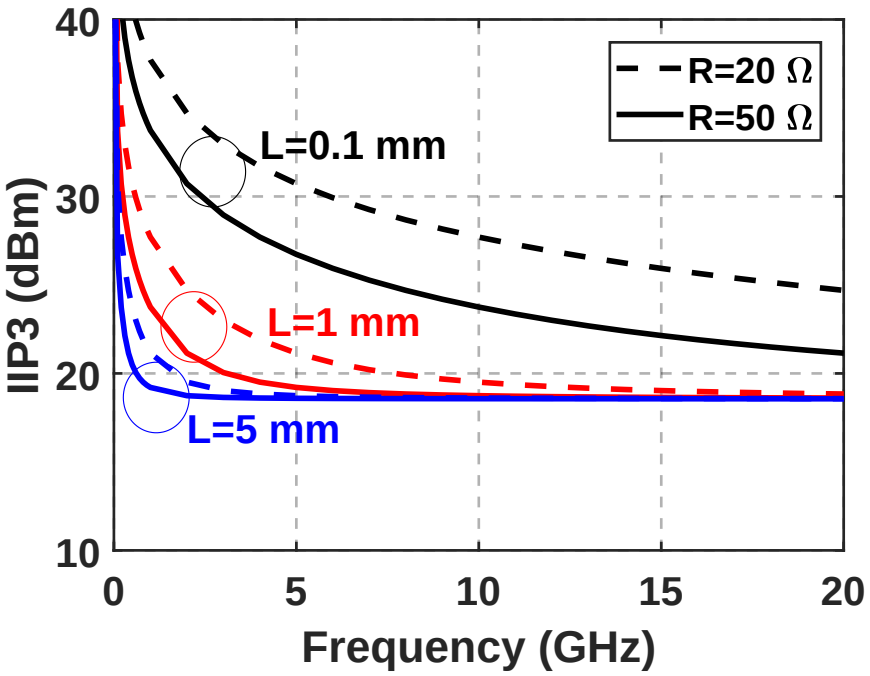

Figure 2.5: Calculated IIP3 of the RC network using Volterra series for different diode lengths.

To accurately characterize the nonlinearity of the capacitance, we designed a p-i-n diode test structure. The diode was fabricated in the SiP process as shown in Fig. 2.3.

The measured data and extracted fit for the data is illustrated in Fig. 2.4. At a nominal reverse bias voltage of -4 V, the capacitance per unit length is about 0.8 pF/mm. The coefficients for C_k will be used in subsequent analyses.

The IIP3 of the C-V junction is plotted in Fig. 2.5. At low-frequency, the IIP3 increases to more than 30 dBm. At high frequency, the IIP3 for all junction lengths approaches around 20 dBm based on the capacitance parameters extracted in Fig. 2.4. Using $b_1 = 1/15$ V-mm for a SiP process, the optimal MZM length is around 1.5 mm from (2.26) since the IIP3 would become dominated by the CV nonlinearity. While the asymptotic limit does not depend on the generator resistance, a lower resistance improves IIP3 at low frequency leading to shorter devices. For 50 Ω and 20 Ω, the IIP3 as a function of device length and frequency is plotted in 2.5.

2.4.2 Phase Section Nonlinearity

The complex refractive index in silicon waveguides changes with carrier density [21] and underlies the operation of ring [22], electro-absorption, and MZM modulators. The carrier density is controlled through either carrier depletion or injection. However, carrier-injection modulators are typically limited by carrier recombination in bandwidth and modulation speed [17].

The Drude model describes the dielectric constant of a solid as a function of minority carrier density and frequency [23]. Based on experimental results, Soref and Bennett [24] found that refractive index exhibits some nonlinearity with ΔN_e and ΔN_h, the change in the electron and hole density. Later, Nedeljkovic developed an empirical model for both $\Delta\alpha$ and Δn, where coefficients and powers of ΔN_e and ΔN_h are wavelength-dependent

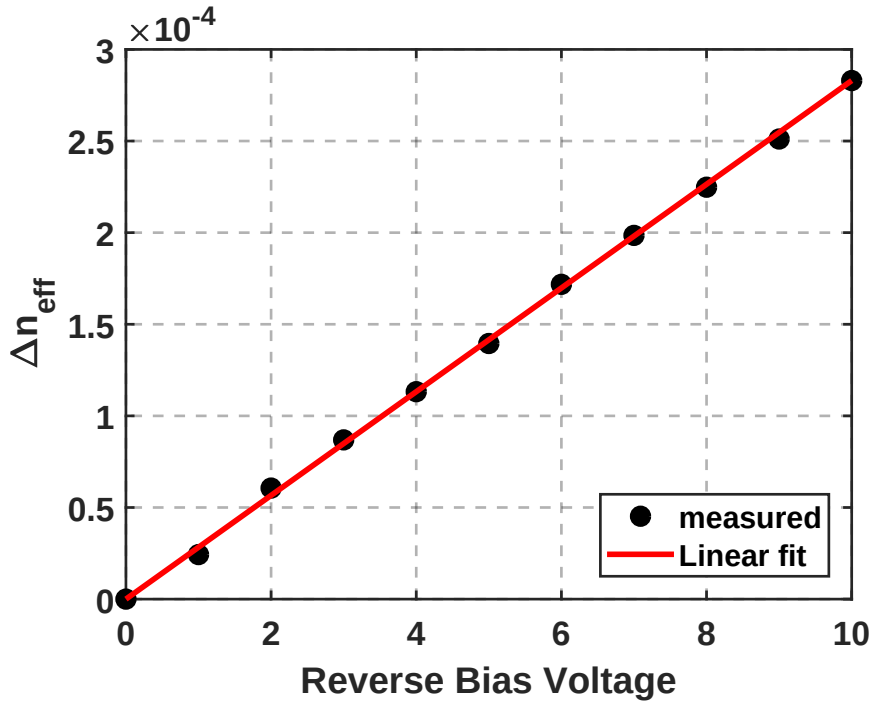

Figure 2.6: Measured effective refractive index change (Δn_{eff}) as a function of reverse bias DC voltage

[25]. For $\lambda = 1550nm$, $\Delta\alpha$ and Δn are

$$\Delta\alpha = 8.9 \times 10^{-21}\Delta N_e^{1.17} + 5.8 \times 10^{-20}\Delta N_h^{1.11} \tag{2.27a}$$

$$\Delta n = -5.4 \times 10^{-22}\Delta N_e^{1.01} - 1.5 \times 10^{-18}\Delta N_h^{0.84}. \tag{2.27b}$$

Effective refractive index change ($\Delta n_{eff}(V)$) can be found numerically for different propagating modes from the refractive index in the material, as well as free-carrier absorption as a function of bias voltage ($\alpha(V)$) [26]:

$$\Delta n_{eff}(V) = \frac{\int E^*(y).\Delta n(y,V)E(y)dy}{\int E^*(y).E(y)dy}\frac{dn}{dn_{co}} \tag{2.28}$$

$$\alpha(V) = \frac{\int E^*(y).\Delta\alpha(y,V)E(y)dy}{\int E^*(y).E(y)dy} \tag{2.29}$$

where n_{co} is silicon refractive index, and $E(y)$ is the 1D field profile [26]. Since the electron and hole concentrations can be related to the charge in the junction, i.e. $\Delta N_e = \frac{Q}{qlwh}$ where lwh are the length, width, and height of the depletion region, the nonlinear change of refractive phase can be estimated as a polynomial function of charge. Referring the index change to a change in the phase constant, $\Delta\beta = \frac{2\pi}{\lambda}\Delta n_{eff}$,

$$\Delta\beta(Q) = \frac{2\pi}{\lambda}\Delta n_{eff} \approx \frac{2\pi}{\lambda}\sum_{k=1}^{m} n_k Q^k. \tag{2.30}$$

The IIP3 for the nonlinear phase shift is

$$IIP3_{Q\beta} = \sqrt{\frac{4}{3}\frac{n_1}{n_3}}. \tag{2.31}$$

While this IIP3 value is expressed in terms of charge, the equivalent voltage is found from $IIP3_{Q\beta} = C_0 IIP3_{V\beta}$.

A SiP test structure constructed from an asymmetric MZM is shown in Fig. 2.3 to extract the index change and attenuation of a SiP phase shifter constructed from a shallow-etch silicon waveguide with rib width = $500nm$, rib thickness = $220nm$, and slab thickness = $100nm$. The measurement is done by sweeping wavelength and varying bias voltage on the asymmetric MZM. From free spectral range (FSR), change of effective refractive index as a function of voltage is measured. The measued Δn_{eff} with the applied reverse bias voltage is plotted in Fig. 2.6.

Table 2.1: Gain and IIP3 for each source of nonlinearity

	$V-Q$	$Q-\beta$	$\beta-P_{out}$
Gain	$C_0A_1(j\omega)=\frac{C_0}{1+j\omega R_iC_0}$	$\frac{2\pi}{\lambda}n_1$	$\mathrm{e}^{-\alpha_{DC}L}P_{in}L$
IIP3	$\frac{2}{\sqrt{\omega R_i C_2}}\sqrt[4]{\frac{(1+5(\omega R_iC_0)^2+4(\omega R_iC_o)^4}{1+\omega^2R_i^2(2C_0+\frac{C_1}{2}C_2)^2}}$	$\sqrt{\frac{4}{3}\lvert\frac{n_1}{n_3}\rvert}$	$\sqrt{2}\frac{1}{L}$

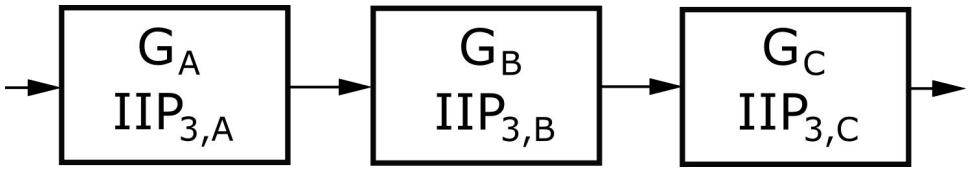

Figure 2.7: Representation of a system formed by three cascaded nonlinear blocks and characterized by a third-order polynomial.

2.4.3 Cascade Analysis

Linearity metrics for a system comprised of cascaded block can be written in terms of linearity of each block. A representation of such system is shown in Fig. 2.7. Assuming each block can be modeled by a third order polynomial, for example $Y_A = a_1X + a_2X^2 + a_3X^3$, IIP_3 of the system can be found from:

$$\frac{1}{IIP3^2} = \frac{1}{{IIP3_A}^2} + \frac{{a_1}^2}{{IIP3_B}^2} + \frac{{a_1}^2{b_1}^2}{{IIP3_C}^2} + \frac{3}{2}\left(\frac{a_2}{IIP2_B} + \frac{a_1^2b_2 + a_2b_1}{IIP2_C}\right) \tag{2.32}$$

From the prior analysis, we return to Fig. 2.2 to model the cascaded nonlinear blocks. Since the attenuation path primarily produces even-order distortion from (2.6), we will ignore the contribution of attenuation nonlinearity. A summary of the gain and nonlinear distortion is shown in Table I. First, the applied RF voltage generates distortion due to C-V nonlinearity. The resulting charge generates a nonlinear change in the refractive index charge. Finally, MZM produces a power variation with the phase change which is the last nonlinear block in the path of signal.

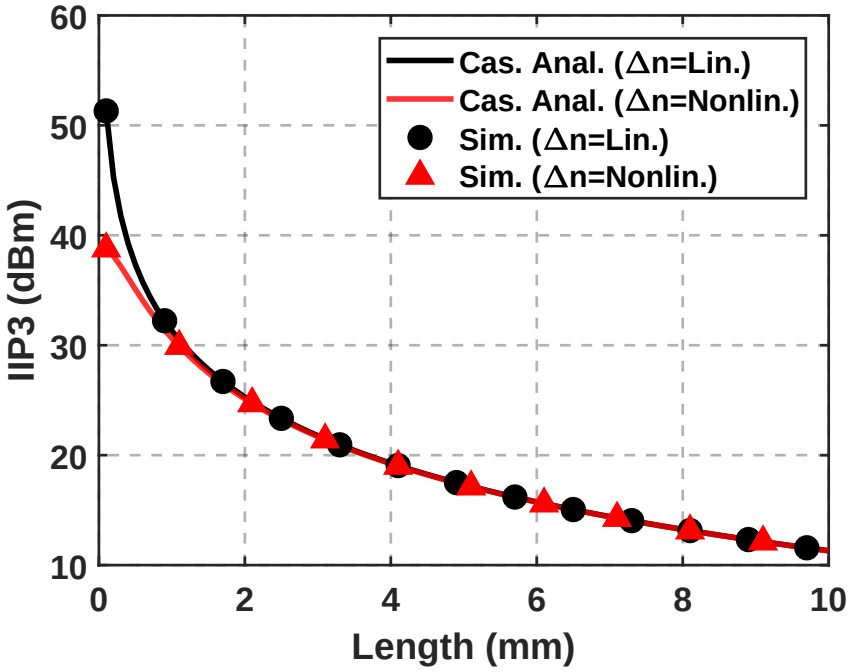

Figure 2.8: IIP3 as a function of MZM length found from cascaded analysis in the absence of C-V variation and behavioral simulation for two different cases of linear phase shifters and nonlinear phase shifters.

To develop an expression for the IIP3 that incorporates the individual sources of IIP3, cascade foruma for IIP3 can be used.

The total IIP3 (in voltage) due to the cascade is

$$\frac{1}{IIP3^2} = \frac{|A_1|^2}{IIP3_{VC}{}^2} + \frac{|A_1|^2 C_0^2}{IIP3_{Q\beta}{}^2} + \frac{|A_1|^2 C_0^2 (\frac{2\pi}{\lambda} n_1)^2}{IIP3_{\beta P}{}^2} + \frac{3}{2}\left(\frac{C_1|A_2|}{IIP2_{Q\beta}} + \frac{C_0^2|A_1|^2(\frac{2\pi}{\lambda}n_2) + C_1|A_2|(\frac{2\pi}{\lambda}n_1)}{IIP2_{\beta P}}\right). \tag{2.33}$$

The nonlinear terms are found from (2.21), (2.22), and (2.30). Note that the role of IIP2 is expected to be weak since $IIP2_{\beta P}$ is large. The cascaded IIP3 is plotted in Fig. 2.8 while ignoring C-V nonlinearity ($IIP3_{VC} = \infty$) to understand the role of the index nonlinearity. Clearly, the IIP3 decreases as $\propto \frac{1}{L}$; the longer MZM has a lower V_π and

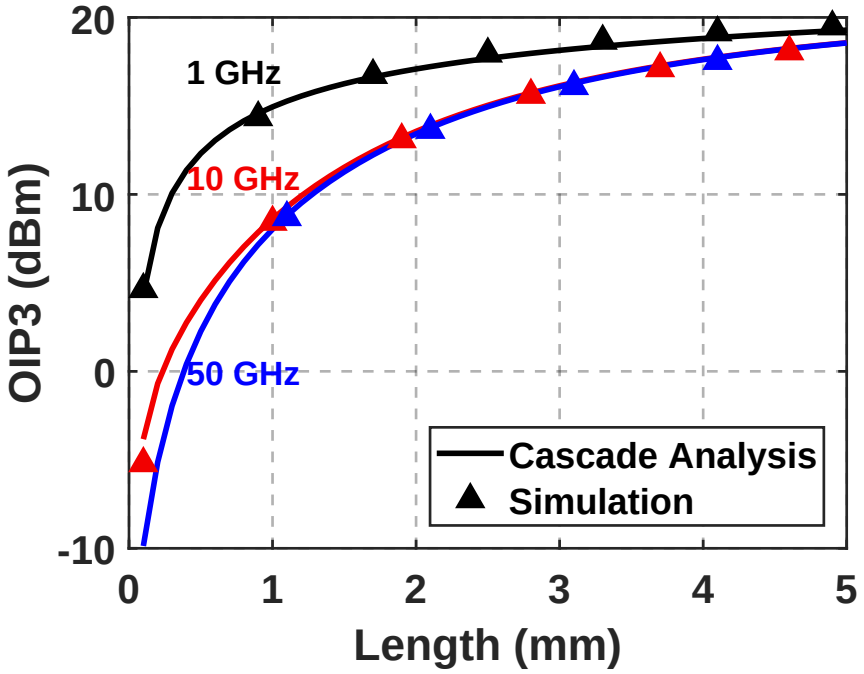

Figure 2.9: OIP3 as a function of MZM length found from cascaded analysis and behavioral simulation at different frequencies including C-V variation.

therefore a lower IIP3. The nonlinear phase shift becomes a dominant source of IIP3 for modulators with length under 1 mm.

Fig. 2.9 compares the RoF OIP3 at different frequencies to illustrate the high-frequency OIP3 limitation. The higher frequency devices see a significant reduction in OIP3 for relatively short devices due to the high voltages that are required across the junction of the optical waveguide.

2.5 Conclusion

Three main sources of nonlinearity in MZM are found as junction capacitance nonlinearity, phase shifter nonlinearity, and cosine transfer function of MZM. A frequency dependant nonlinear model was developed for the MZM and, by using cascade analysis,

IIP3 of the overall system was found. It shows that at low frequencies cosine transfer function of the MZM is the dominant source of nonlinearity, while at high-frequencies C-V nonlinearity limits the IIP3 furthermore.

Chapter 3

An Integrated RF Photonics Receiver in SiGe and Silicon Photonics

3.1 Introduction

For wireless communication networks, SFDR of better than $110 \cdot \mathrm{Hz}^{2/3}$ is required [27]. This put silicon photonic based MZMs in a tough spot, as linearity of these modulators is limited at high frequencies. Here, co-design of a low-noise distributed driver (LNDD) integrated with a SiP MZM, as shown Fig. 3.1, is discussed. The RF photonic receiver's bandwidth works over 1 - 20 GHz to cover sub-6GHz 5G for cellular networks, X-band and Ku-band for space communications [28].

In Section 3.2, segmented design for MZM to improve SFDR is discussed. To compensate the SiP SFDR, the LNDD is proposed based on a broadband LNA and an active-balun with a high-voltage swing driver. In Section 3.4, circuit simulations of the SiGe LNDD is discussed. In Section 3.5, measurements of the LNDD and MZM are

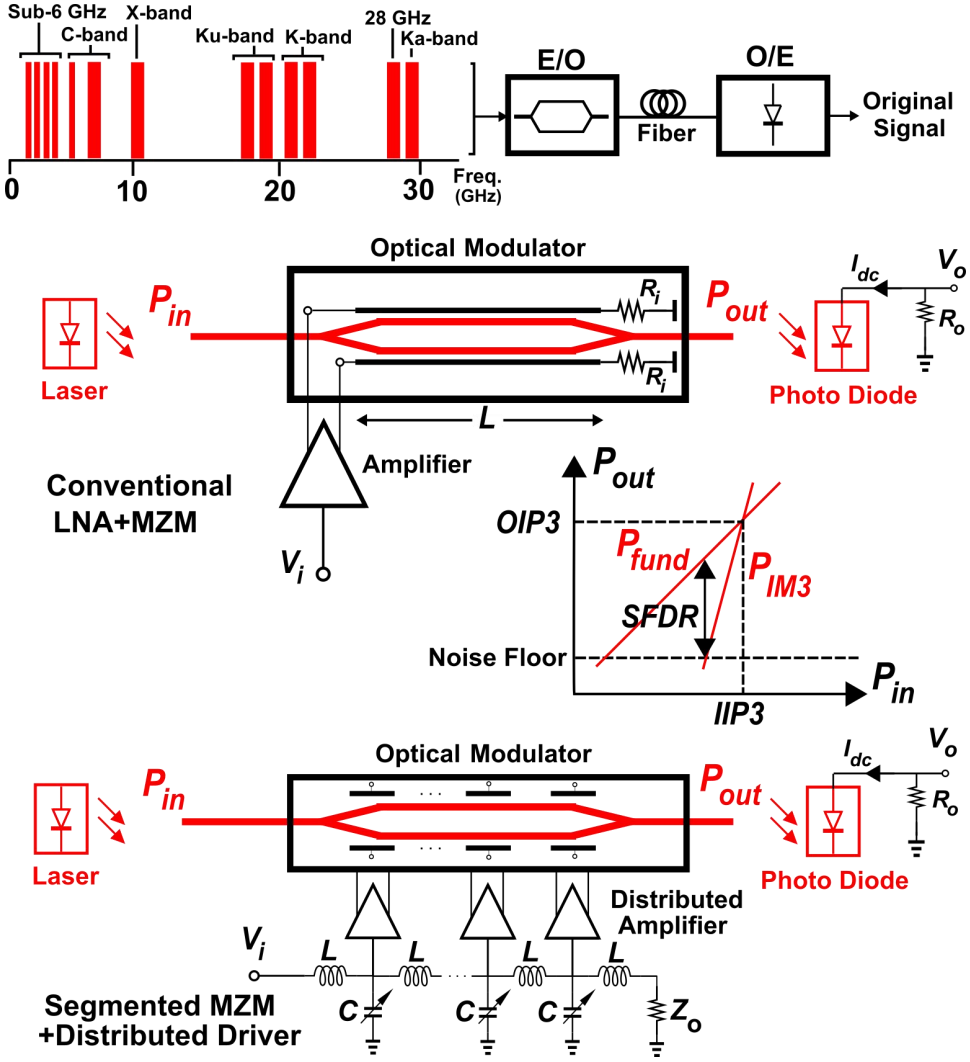

Figure 3.1: Illustration of a conventional RoF link and the proposed low-noise distributed driver

presented. The RoF transmitter achieves a 1-20 GHz bandwidth and a SFDR of 109 dB·Hz$^{2/3}$ at 11 GHz.

Recent published work has investigated linearity improvement of commercial MZMs using systematic techniques and linearity improvement using novel optical modulators [29–50]. External predistorters improved the SFDR of $LiNbO_3$ modulators for a 20-km analog photonic link to an SFDR of 108.4 dB·Hz$^{2/3}$ in a 1-Hz bandwidth [29].

In a traveling-wave MZM, return loss, electrical and optical group delay matching,

and high RF gain are difficult to simultaneously achieve. For high-speed data communications, segmented MZMs have been proposed. Hybrid integration of an InP segmented MZM and BiCMOS driver [51], and monolithic integration of segmented MZM and driver in SiGe:C BiCMOS platform [52] are reported. For 50 Ω terminated optical modulators, high speed BiCMOS drivers in SiGe technology are also reported [53, 54]. In the case of RF applications, the segmented approach allows per amplifier phase control to tune and compensate for process variations at the expense of higher power. Integration of segmented MZM and driver has been previously reported in [55], where a broadband optical transmitter based on a SiGe driver and SiP modulator was proposed. However, for RoF application, different requirements, most notably on noise and linearity, have to be met. Moreover, this work employs a distributed driver with single input while in [55] each segment has an independent input pad which requires a more sophisticated driving scheme.

Experimental measurement of SFDR in integrated MZMs reveals reduction at high frequency. In Fig. 3.2, the SFDR of several recent publications is shown and indicates that the SFDR degrades with frequency. Moreover SiP technologies do not offer similar SFDR as III-V materials. In chapter 2, the frequency dependence of SFDR of the MZM as well as the reasons for reduced SFDR in SiP devices was discussed.

The relatively low RF gain and high NF of the SiP MZM suggests that an LNA should offset the gain of the RoF link and compensate the contribution of RoF noise.

3.2 Segmented MZM for Improved SFDR

The analysis of the CV variation in (2.26) indicated that a critical length segment exists such that the CV nonlinearity did not exceed the MZM IIP3. Segmenting the total length of the MZM into N sections suggests that the IIP3 of each MZM segment is

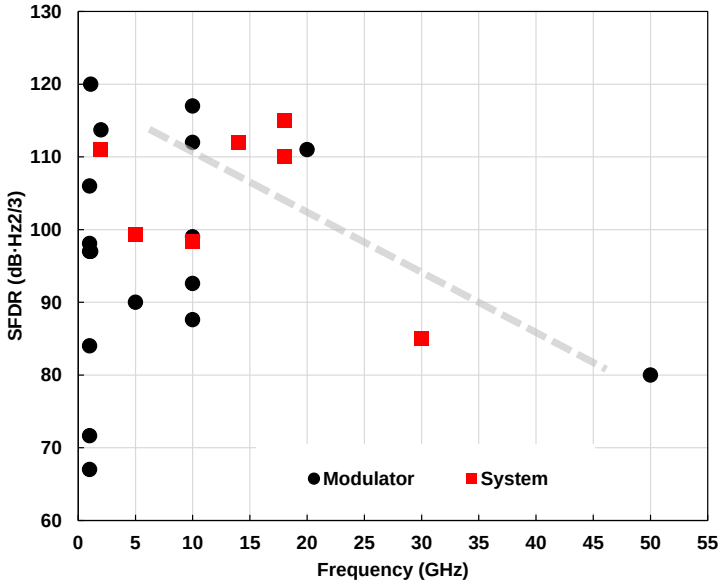

Figure 3.2: SFDR as a function of frequency for recent published work.

inherently higher. For instance, Fig. 2.8 suggests that reducing the length of the MZM from 4mm to 1mm improves the IIP3 by a factor of 10. Additionally, the segment can be driven by a lower resistance without introducing large impedance mismatch. The lower drive resistance also improves the IIP3 as shown in Fig. 2.5. For a given MZM phase shifter characteristic, the SFDR is plotted as a function of frequency for a traveling wave MZM and segmented MZM in Fig. 3.3. At low-frequency, the SFDR of the SiP MZM is around 118 dB·Hz$^{2/3}$. As the frequency increases to 30 GHz, the SFDR drops by around 10 dB for the traveling-wave MZM due to higher frequency-dependent traveling wave losses along the electrode and lower IIP3 of voltage to charge conversion in p-i-n phase shifters. On the other hand, the segmented MZM exhibits a relatively flat SFDR across the frequency band, exhibiting only 2-dB SFDR reduction. The underlying SFDR of the segmented MZM indicates that the driver SFDR should exceed 120 dB·Hz$^{2/3}$ across the

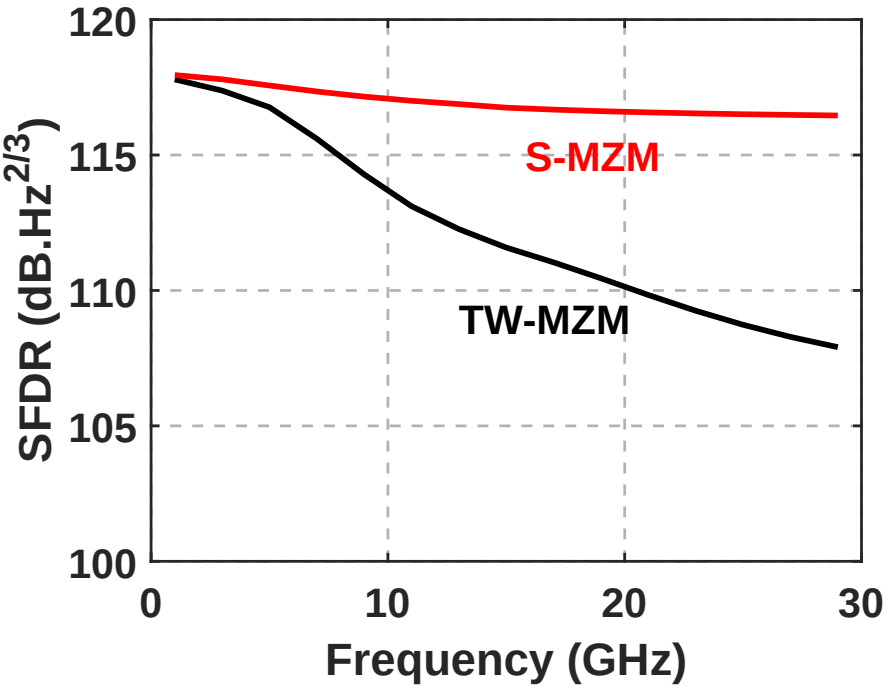

Figure 3.3: SFDR of the SiP MZM as a function of frequency for a 50-Ohm driver and the segmented modulator driver.

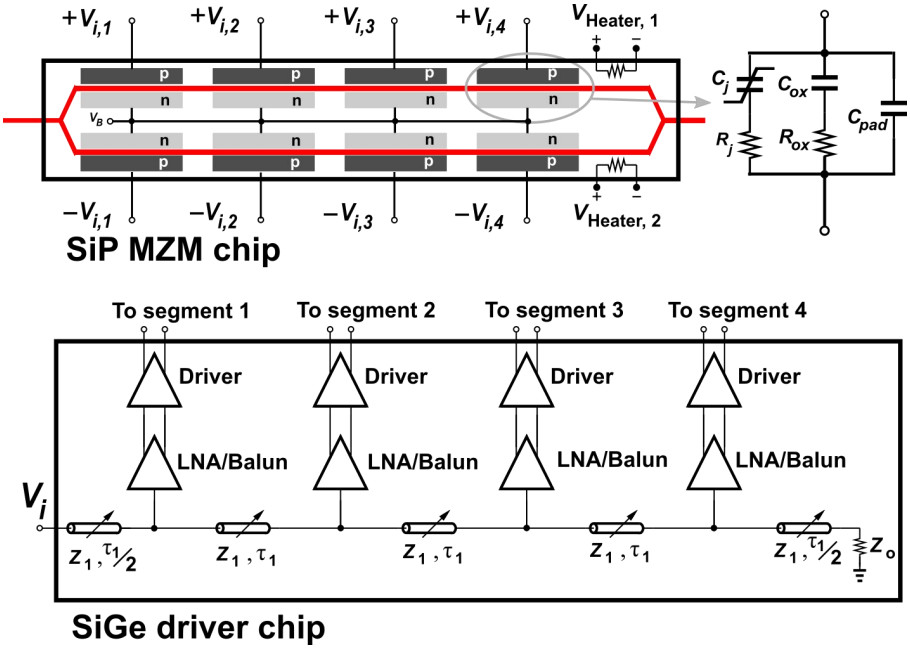

Figure 3.4: Block diagram of 4-segment SiP MZM (top left), equivalent circuit model of the p-i-n junction in reverse bias (top right), and block diagram of the low noise distributed driver consisting of a low-noise amplifier, active balun, and differential driver (bottom).

frequency band.

3.3 Silicon photonics Segmented MZM Design

In this work, a segmented MZM is designed in the AIM photonics 65-nm SiP process. The segmented MZM consists of 4 segments, each 900 μm long, based on the analysis from Chapeter 2 and the analysis in Fig. 2.5 when an RC bandwidth limit of 20 GHz. The number of segments is found from required E/O gain, and since E/O gain is small, number of segment is chosen based on available silicon area, resulting in 4 segments. Fig. 3.4 shows the structure of the segmented MZM. Each segment is a reverse-biased p-i-n junction that is optimized for a combination of linear phase shifters using DC Kerr effect and plasma dispersion [56]. Fig. 3.4 also shows the small-signal model for the p-

i-n junction used in simulations where C_j is nonlinear junction capacitor, R_j is junction capacitor, C_{ox} is capacitance to substrate at junction terminal, R_{ox} is the equivalent substrate resistance, and C_{pad} is the pad equivalent capacitor. Heater resistors are used to bias the modulator at the quadrature point.

3.4 Low-Noise Distributed Driver

The LNDD is introduced to distribute the RF signal to the multiple segments. The distributed segment drivers are fed by a single-ended traveling wave line. There are several advantages to this approach. First, the segmented driver avoids frequency-dependent loss of the long traveling wave electrode. Second, the segmented driver alleviates some of the nonlinear capacitance variation. Third, the LNDD provides high gain and low NF for the RoF link.

The co-design of the segmented MZM with a driver offers degrees of freedom to improve SFDR. The low-noise distributed driver (LNDD) is specified to provide a broadband response to match the bandwidth of the MZM, provide high-gain to overcome the RoF link gain, and low-noise figure to improve the noise figure of the link. Additionally, reducing the impedance at the output of the driver stage to less than 50-Ω improves the IIP3 by decreasing effect of junction capacitor nonlinearity. Moreover, compared to a traveling MZM, segmented MZM is less vulnerable to electrode loss of transmission line. By moving the transmission line to the input of driver, transmission line is being loaded by high impedance rather than low and lossy impedance of p-i-n diodes, resulting in extended bandwidth.

Finally, velocity matching the optical signal in the silicon waveguide with electrical driver can be performed at each MZM segment, while in traveling MZM design, achieving simultaneous impedance matching to 50 Ω and velocity matching to optical silicon

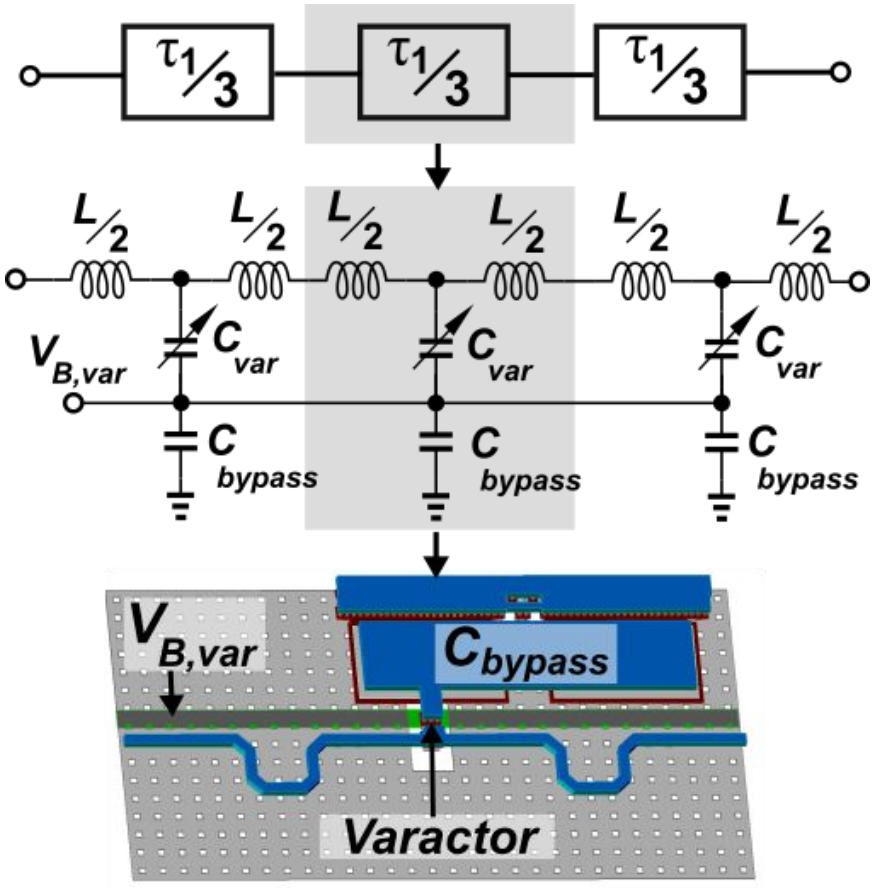

Figure 3.5: Schematic and layout of the ATL unit cell

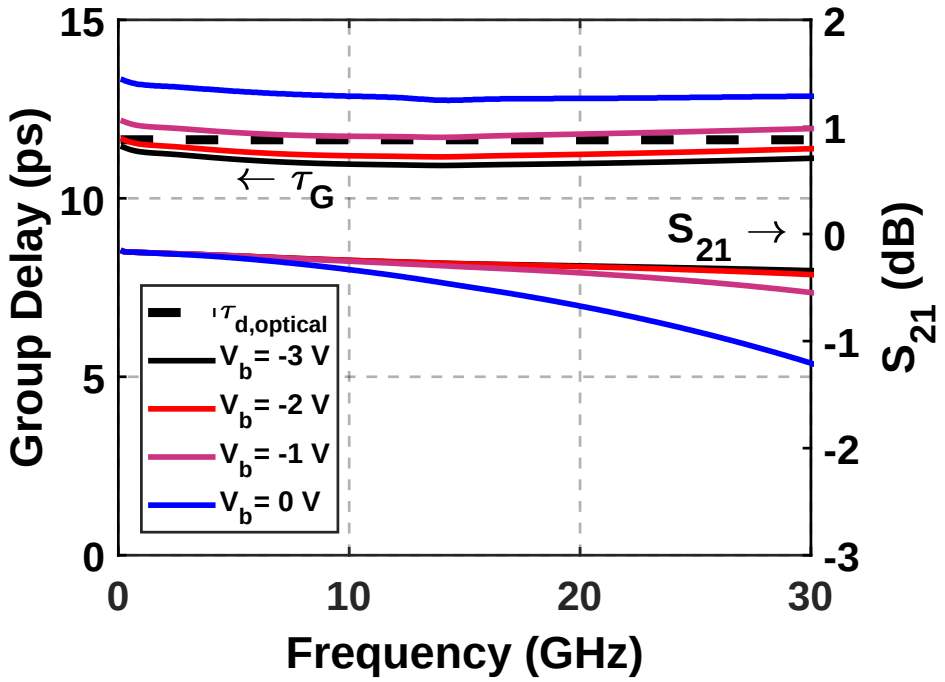

Figure 3.6: Simulated group delay of ATL against calculated optical delay (left axis), and S21 of a section of ATL for different varactor biases (right axis).

waveguide is challenging and leads to a trade-off.

The SiGe LNDD is implemented in a SiGe HBT process and consists of 4 circuit blocks as shown in Fig. 3.4. First, the input matching uses a on-chip terminated, single artificial transmission line (ATL) to provide broadband impedance matching, where the phase velocity along the ATL can be matched to the optical phase velocity. The ATL is loaded with varactors that tune the velocity of the ATL to match the velocity of light in the modulator waveguide arms. Time delay ($\tau_{d,optical}$) between each segment of the MZM can be found from

$$\tau_{d,optic} = \frac{Ln_g}{c} = 11.64\ ps \tag{3.1}$$

where $L = 900\ \mu m$ is length of one segment, $n_g = 3.88$ is group index of silicon waveguide

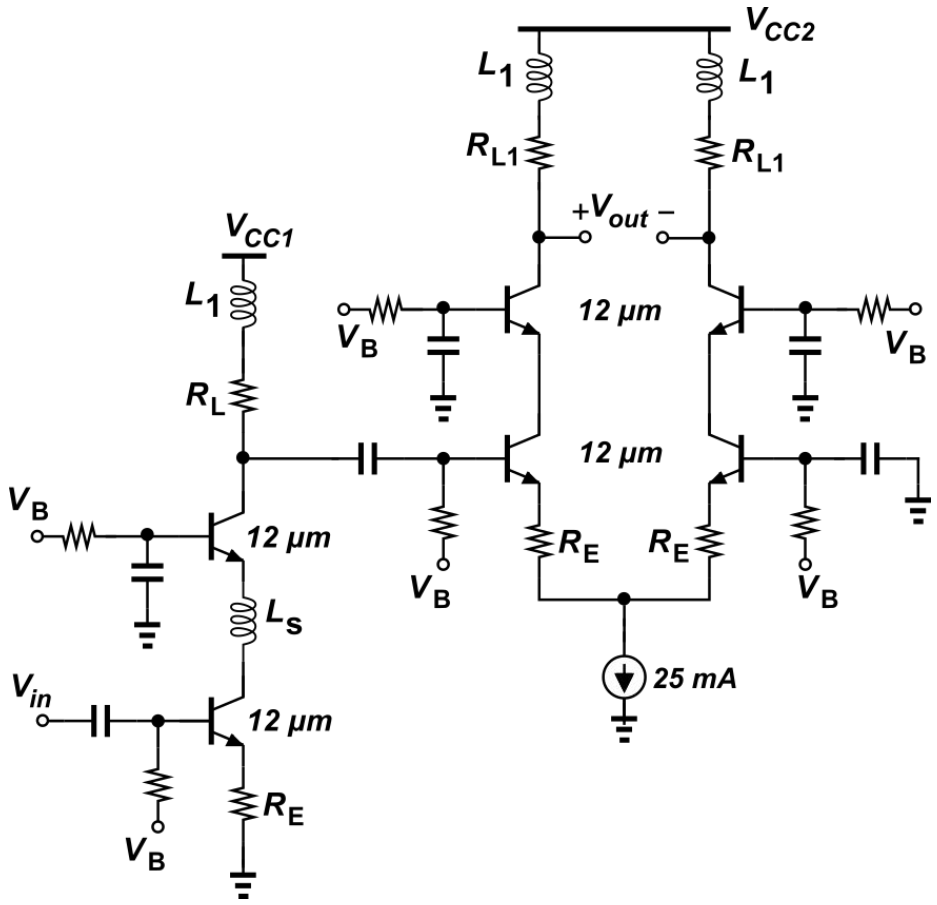

Figure 3.7: Schematic of the low noise amplifier and active balun

at $\lambda = 1550\ nm$, and c is speed of light in vacuum.

The schematic and layout of an ATL unit cell are shown in Fig. 3.5. Three cascaded LC based T-networks are used between each LNA to have decent margin to Bragg cut-off frequency of ATL, defined by $2/\sqrt{LC}$. L and C are sized to match velocity of optical signal in silicon waveguide and impedance matching to 50 Ω after loading by LNA stages. The ground plane shields the ATL from varactor bias line. Fig. 3.6 shows simulated group delay (τ_G) for a section of ATL and S_{21} for different biases of varactors. The time delay of the designed cell covers the calculated $\tau_{d,optical}$ with a good margin, providing ability to tune the delay. This is critical since any process variation in doping levels in p-i-n phase shifter will result in change in expected $\tau_{d,optical}$.

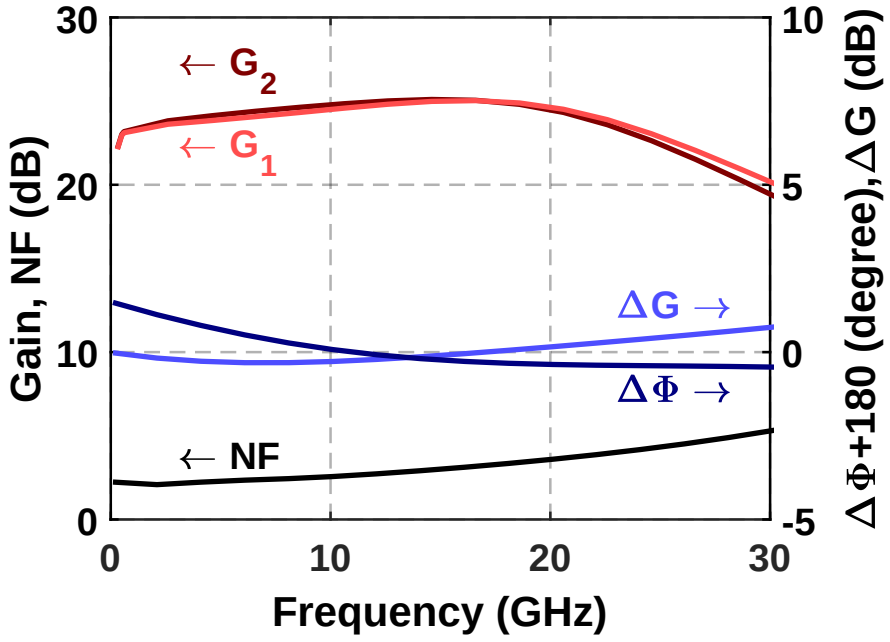

Figure 3.8: Simulated gain and NF of the LNA + active balun (left axis), and simulated gain and phase imbalance of the LNA + Active balun (right axis)

Second, four amplifier stages are distributed along the ATL. Each consists of a low-noise amplifier (LNA), an active balun, and a high-voltage driver. Fig. 3.7 shows the schematic of LNA and active balun. The LNA is a cascode amplifier with emitter degeneration to increase the impedance loading the ATL and improves the bandwidth. The LNA has NF of less than 4 dB up to 30 GHz. The balun incorporates high differential gain with low common mode gain to produce a differential signal.

Fig. 3.8 shows the simulated gain and NF of the LNA/balun stage and single-ended to differential conversion gains (G_1, G_2). Moreover, gain and phase imbalance (ΔG, $\Delta\Phi$) of the LNA/Balun stage are shown indicating less than 0.5 dB gain variation up to 26 GHz and less than 3° phase variation up to 30 GHz. Fig. 3.9 shows the schematic of the high-swing driver stage. The differential output driver uses a differential cascode amplifier to provide a 3-Vpp signal swing on the segmented load impedance. In the design of LNA, balun, and differential driver stage, inductive peaking technique is employed to extend

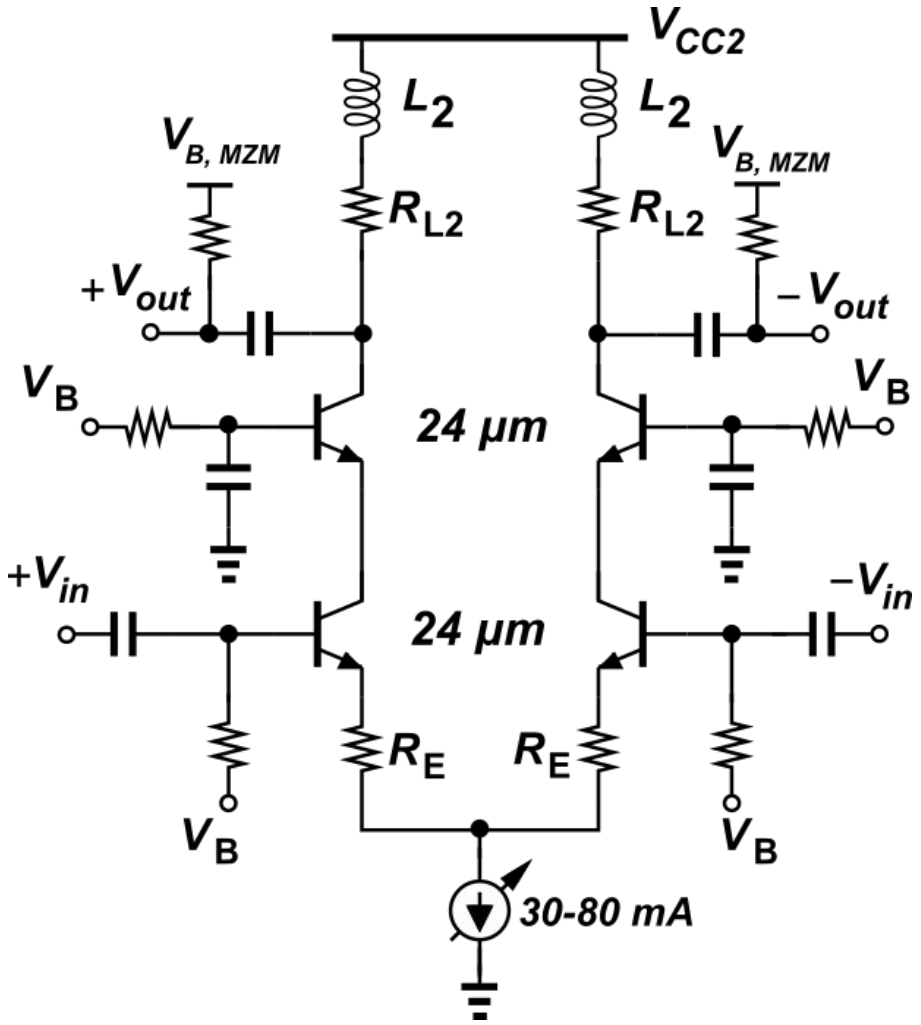

Figure 3.9: Schematic of the differential driver

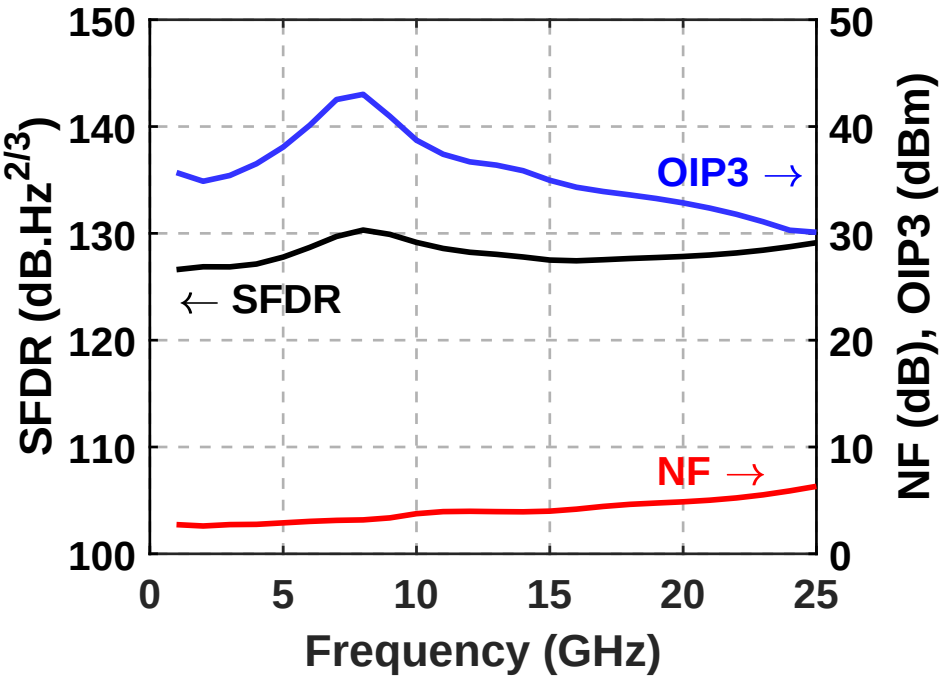

Figure 3.10: Simulated NF, IIP3 and SFDR of the low-noise distributed driver.

the bandwidth.

Fig. 3.10 shows the simulated NF, OIP3, and SFDR of the LNDD. The simulated NF is lower than 5 dB up to 25 GHz. The average IIP3 is 15 dBm for the frequency range of 1-25 GHz and the OIP3 exceeds 35 dBm. The OIP3 is higher than the anticipated IIP3 of the MZM and indicates that the LNDD should not limit the linearity of the RoF link. Notably, the OIP3 peaks around 8 GHz at 42 dBm. We attribute the high OIP3 to the gain and phase mismatch in the active balun. When the mismatch is minimal, higher OIP3 is observed. The average calculated SFDR from NF and IIP3 is about 128 dB·Hz$^{2/3}$.

Electro-optical co-simulation of the SiGe driver and segmented MZM is performed for the RoF link, where Verilog-A behavioral models are used in modeling the SiP segmented MZM. The simulated gain for the RoF link is plotted as a function of frequency in Fig.

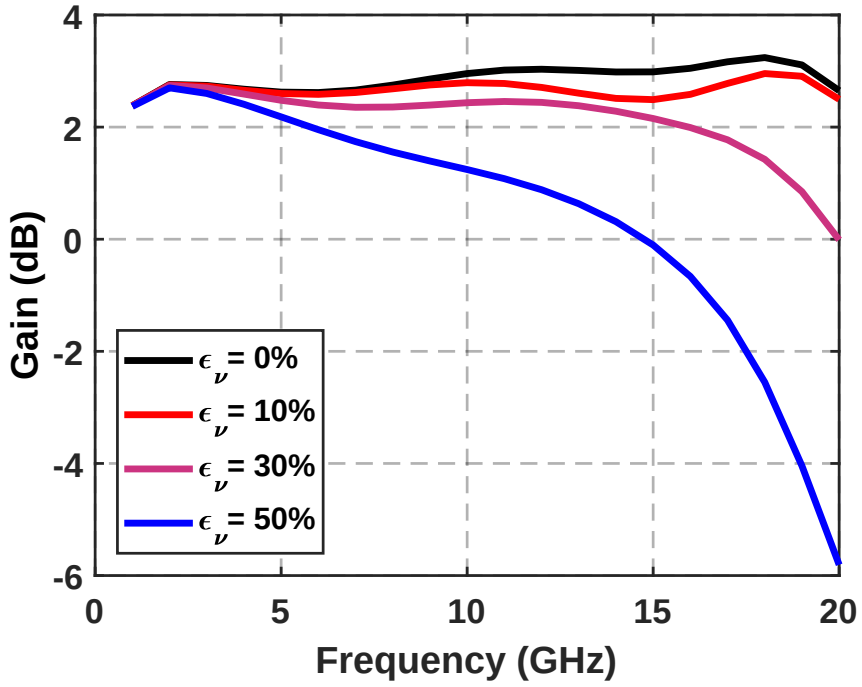

Figure 3.11: Simulated gain for different velocity mismatch values.

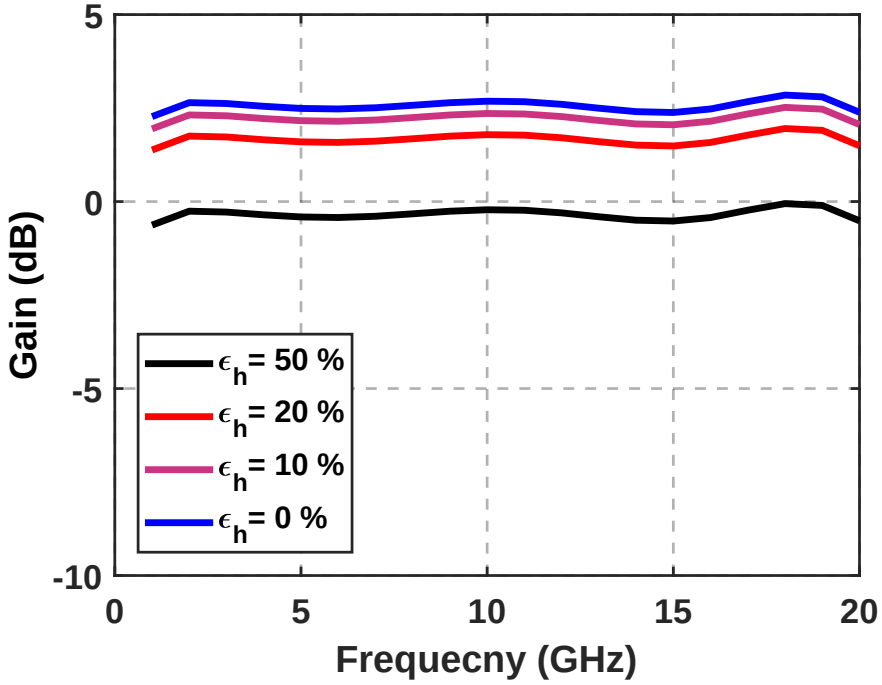

Figure 3.12: Simulated gain for different heater bias points.

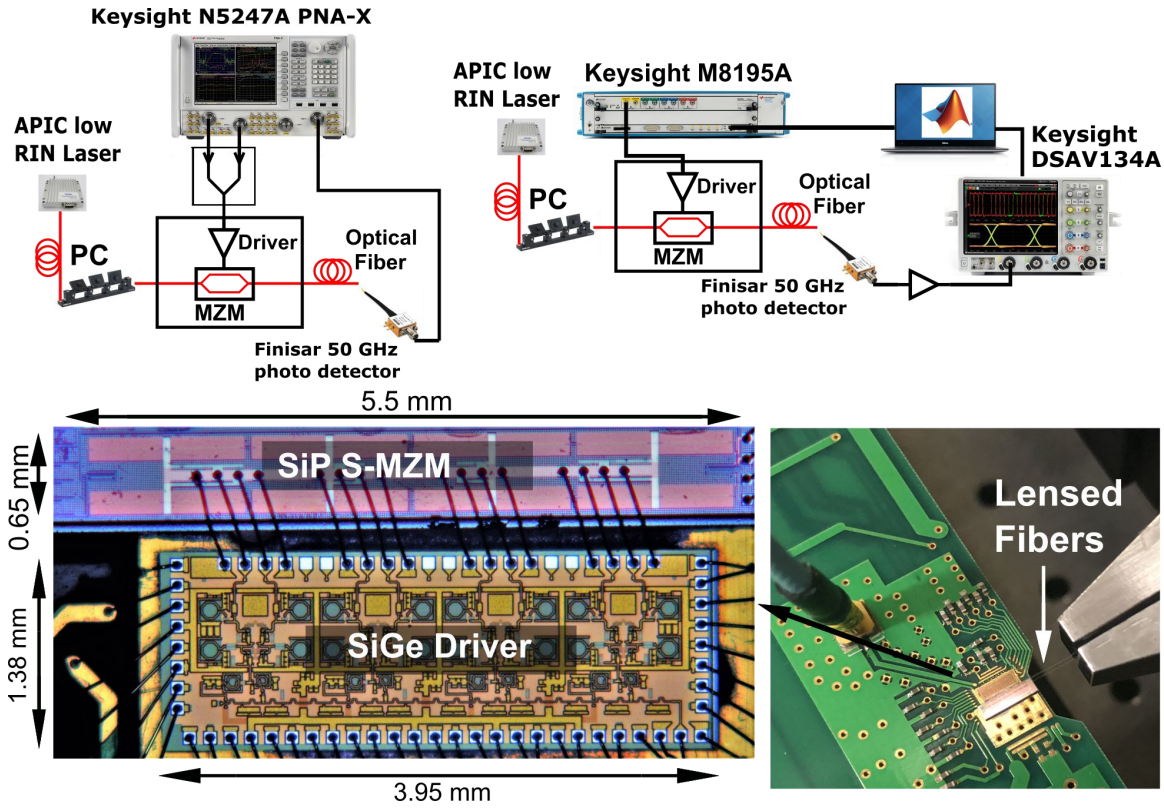

Figure 3.13: Measurement setup for S-parameters and linearity (top left), setup used for EVM measurements (top right), Assembled radio-over-fiber transmitter with a SiP segmented MZM and a SiGe low noise distributed driver (bottom left), and picture of measurement board and light coupling (bottom right).

3.12 for different velocity mismatch values, where $\epsilon_\nu = 2\frac{\tau_G - \tau_{d,optical}}{\tau_G + \tau_{d,optical}}$. First, it should be expected that the gain is near unity since the LNDD gain is enough to offset the RF gain of the E/O and O/E conversion. Second, velocity mismatch degrades the high-frequency gain roll-off. To a bandwidth of 20 GHz, a mismatch of 30% can be tolerated between the electrical ATL and optical waveguide.

3.5 Measurements

The LNDD is fabricated in a 130 nm SiGe BiCMOS HBT technology and the chip size is 3.95 x 1.38 mm^2. The segmented MZM PIC is fabricated in AIM Photonics 65-

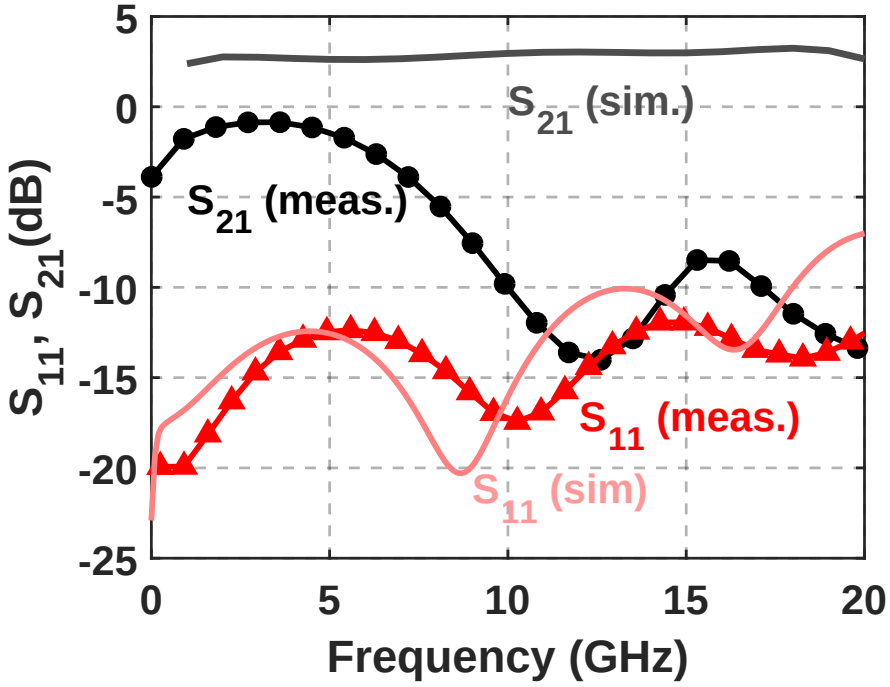

Figure 3.14: Measured S-parameters for radio-over-fiber link with measured S11 of LNDD and measured S21 for the link.

nm SiP process and the chip size is 5.5 x 0.65 mm^2. The assembled RoF transmitter is illustrated in Fig. 3.13 and the segmented MZM PIC is closely mounted adjacent to the SiGe LNDD to reduce the wirebonds between the drivers and the segmented stages. A single-ended RF signal is launched through a mini-SMP connector to a short CPW transmission line on PCB that is wirebonded to the LNDD chip.

The power consumption of the LNDD is 1.65 W, where each amplifier stage consumes 412 mW. The LNA and active balun consume about 120 mW, while the high-swing output driver stage has power consumption of about 280 mW. A small amount of power is also dissipated in DC bias network consisted of current mirrors and reference branches, while power dissipated in reverse biased p-i-n diodes in MZM is negligible.

A 1550-nm low-RIN laser with 18-dBm power and -168 dBc/Hz RIN was used to provide optical power to the MZM. Two lensed fibers provide optical I/O to the PIC.

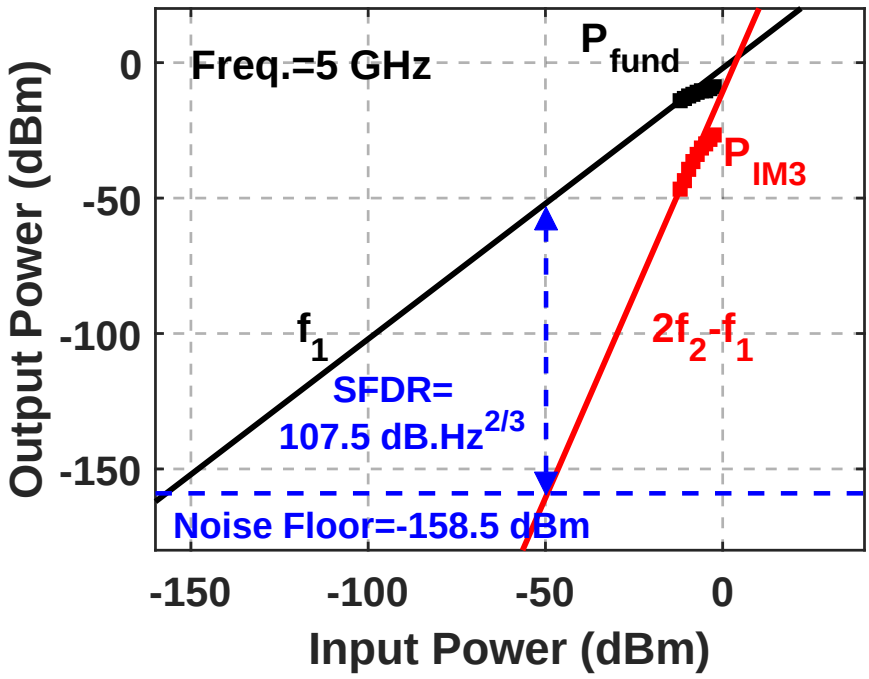

Figure 3.15: Fundamental and intermodulation distortion as a function of input power at 5 GHz

Measured loss for optical edge couplers is about 3-dB and total optical loss of MZM is less than 10-dB, including light coupling loss and the optical power received by the PD is about 0 dBm.

Fig. 3.13 also shows the setup for small-signal and large signal measurement along with view of assembled RoF transmitter and lensed fiber. A Keysight PNA-X is used for both small-signal and large-signal measurements for measuring intermodulation distortion, which is shown in Fig. 3.13. The measured S_{11} and S_{21} for the RoF link are shown in Fig. 3.14 and compared with simulation. The input return loss is better than 12-dB across the frequency band of 0-20 GHz and matches the simulation. The S21 is at most -1 dB and drops to around -10 at 12 GHz.

The frequency roll off is steeper than anticipated due to increased capacitance of the active p-i-n junction phase shifter and uncertainty in the SiP MZM modeling. The

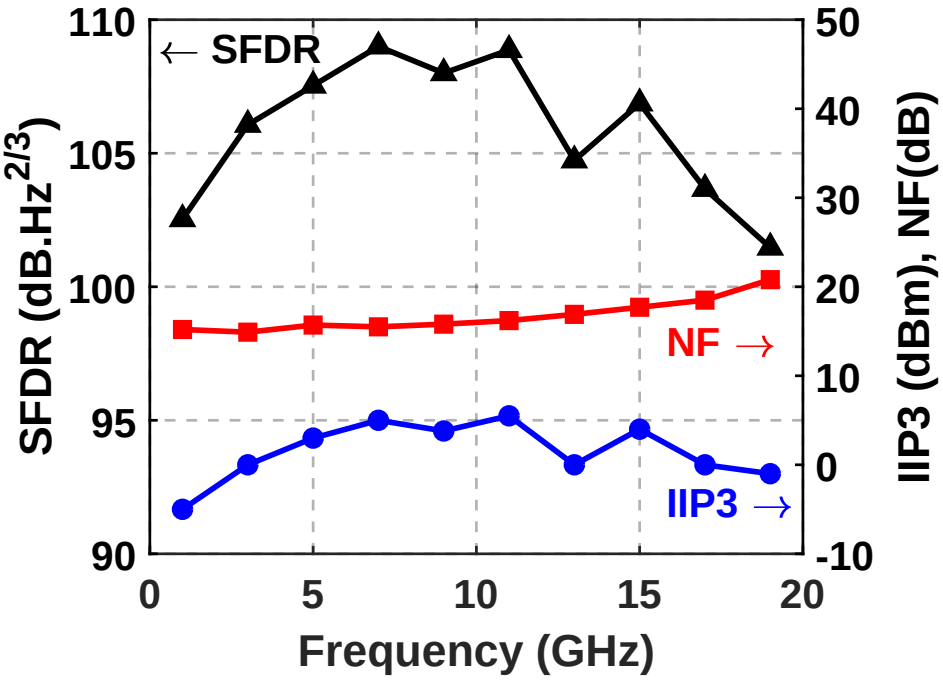

Figure 3.16: Measured NF, IIP3 and calculated SFDR of the RoF link across the frequency band of 1 to 20 GHz.

simulation models do not take into account optical losses in external fibers and fiber to waveguide coupling. Also, the junction models estimate the doping profiles and feature sizes since the PDK provider did not provide this information adding to design uncertainty. For instance, the V_π of these devices ranged between +/-40% introducing much lower RF gain and poor velocity matching. The PD used in measurements introduces a 10 GHz 3dB bandwidth. Additionally wirebonds in the packaging can introduce some frequency variation.

Fig. 3.15 plots IM3 as a function of input power at 5 GHz, where measured noise floor is -158.5 dBm/Hz and the measured SFDR is 107.5 dB·Hz$^{2/3}$. The measured NF, IIP3 and SFDR are plotted in Fig. 3.16 across the frequency band from 0 to 20 GHz. The peak SFDR is greater than 109 dB·Hz$^{2/3}$ at 7 GHz and 11 GHz. The IIP3 ranges between -6 dBm and 5.5 dBm over the 20 GHz range with maximum of 5.5 dBm at 11

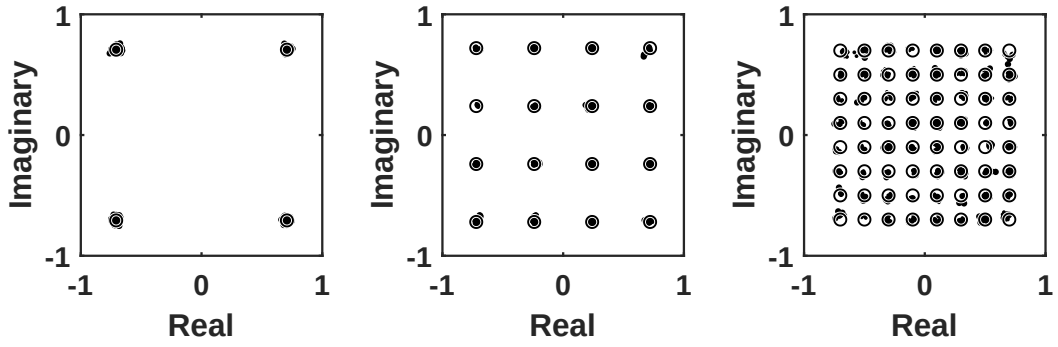

Figure 3.17: Demodulated output waveform constellation of RF photonic link assembly for different modulation formats: QPSK, 16-QAM, and 64-QAM. The symbol rate is 2 GS/s for the QPSK and 16-QAM constellations and 1 GS/s for the 64-QAM constellation.

GHz. Measured NF is less than 20-dB across 0 to 20 GHz with minimum of 14.9 dB at 3 GHz. Compared to simulation results, the measured SFDR is slightly lower than expected due lack of precise model for optics and ambiguity of some SiP process variables.

To demonstrate the RoF transmitter for a wideband RF signal, an 8-GHz RF carrier is modulated with QPSK, 16-QAM, and 64-QAM raised cosine waveforms at 100 MS/s, 200 MS/s, 400 MS/s, 1 GS/s, and 2 GS/s symbol rates, using setup shown in Fig. 3.13, where Keysight M8195A arbitrary waveform generator is used for signal generation and Keysight DSAV134A oscilloscope for demodulation. Demodulated output waveform constellations of the RoF link are shown in Fig. 3.17. The measured error vector magnitude (EVM) is shown in Fig. 3.18. For a 2 GS/s QPSK signal, EVM is maximum 6.1%, and for 16-QAM signal EVM is below 4.5%. For a 1 GS/s 64-QAM signal, measured EVM is 7% in the absence of digital predistortion of the constellation with an RF input power of -40 dBm. Additionally, the ACPR is plotted in Fig. 3.18 and indicates that the ACPR at a 100 MHz offset is 28 dBc below the power in the main lobe.

The measurements are compared in Table. 3.1 with previous work on integrated RF photonic modulators. We demonstrated improved SFDR performance at the cost of

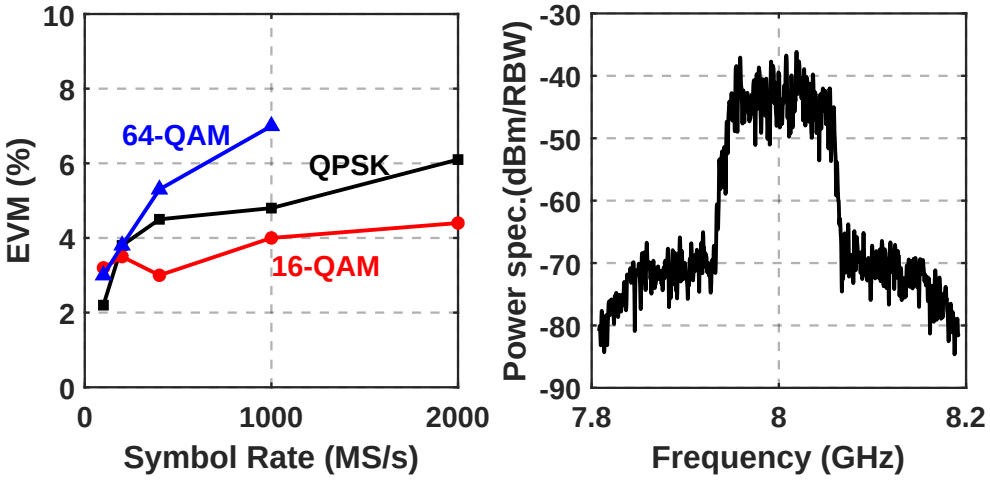

Figure 3.18: Measured EVM at 100 MS/s, 200 MS/s, 400 MS/s, 1 GS/s, and 2 GS/s for QPSK, 16-QAM, and 64-QAM signals (left), and ACPR of 64-QAM with 100 MHz signal (right).

increased power consumption but also with improved bandwidth. A two chip solution, as shown here, is lower power with a separate driver and traveling-wave modulator. Several features of this work are notable. First, the integration of the LNDD and the SiP MZM overcomes some of the gain limitations present in RoF MZMs. Second, the noise figure of RoF MZMs is typically estimated due to the low-gain of the link and often is substantially underestimated. This work has improved noise figure due to the high gain and low noise of the MZM. Finally, this work shows the highest SFDR over the enter range from 1 to 20 GHz. Compared to III-V technologies, however, the SFDR is slightly lower as might be anticipated from the limitations of plasma dispersion for E/O modulation. However, the co-integration demonstrates that a SiGe LNDD solution can be used to overcome some of the limitations of SiP MZMs.

Table 3.1: Table of comparison with reported state-of-the-art silicon and III-V modulators

	Freq. (GHz)	Gain (dB)	Noise Floor (dBm)	SFDR ($dB.Hz^{2/3}$)	Tech.
[31]	2-20	-22	-165[1]	110.03-113.7[1]	Silicon
[33]	1-10	-38	-160[1]	99-106	Silicon (RAMZI)
[34]	5	-43	-160[1]	90	9WG CMOS
[30]	1	-31	-159[1]	117	III-V on Si
[40]	1.1	-57	-165[1]	97	Silicon
This work	**1-20**	(-1)-(-14)	(-153)-(-159)	**101-109**	**Si-SiGe**

3.6 Conclusion

This chapter presented a comprehensive review of the limitations of silicon photonic MZMs on the spur-free dynamic range (SFDR) of a radio-over-fiber link. To compensate for the SFDR degradation in silicon photonic MZMs at high frequency, a co-design approach is proposed where a low-noise distributed driver is designed and implemented in SiGe to drive the segmented SiP MZM over 1-20 GHz. The measured assembly of the SiGe driver and SiP MZM indicates a peak SFDR of 109 dB·$Hz^{2/3}$. The RoF link achieves 7% EVM for 64-QAM modulated signal at 1 GS/s.

Chapter 4

Analog Predistortion Linearization of Mach-Zehnder Modulator

4.1 Introduction

Radio-over-fiber (RoF) has the potential to support microwave and millimeter-wave communication with remote antenna heads. Remote antennas can improve wireless network reliability in environments with poor signal coverage; typically in situations with high RF path loss or blockage. Additionally, RoF links are capable of capturing signals over large instantaneous frequency range and transporting signals with low-loss over optical fiber. RoF links are typically characterized by spur-free dynamic range (SFDR), defined by $\frac{2}{3}$(IIP3-MDS), where IIP3 is the $3^r d$- order input intercept point and MDS is the minimum detectable signal assuming 1-Hz BW. To support wideband RF and microwave communications applications, where complex modulation schemes are employed, the RoF link requires an SFDR exceeding 120 dB·Hz$^{2/3}$, compatible with RF receivers [6, 27].

Fig. 4.1 illustrates a conventional RoF link consisting of an LNA followed by an

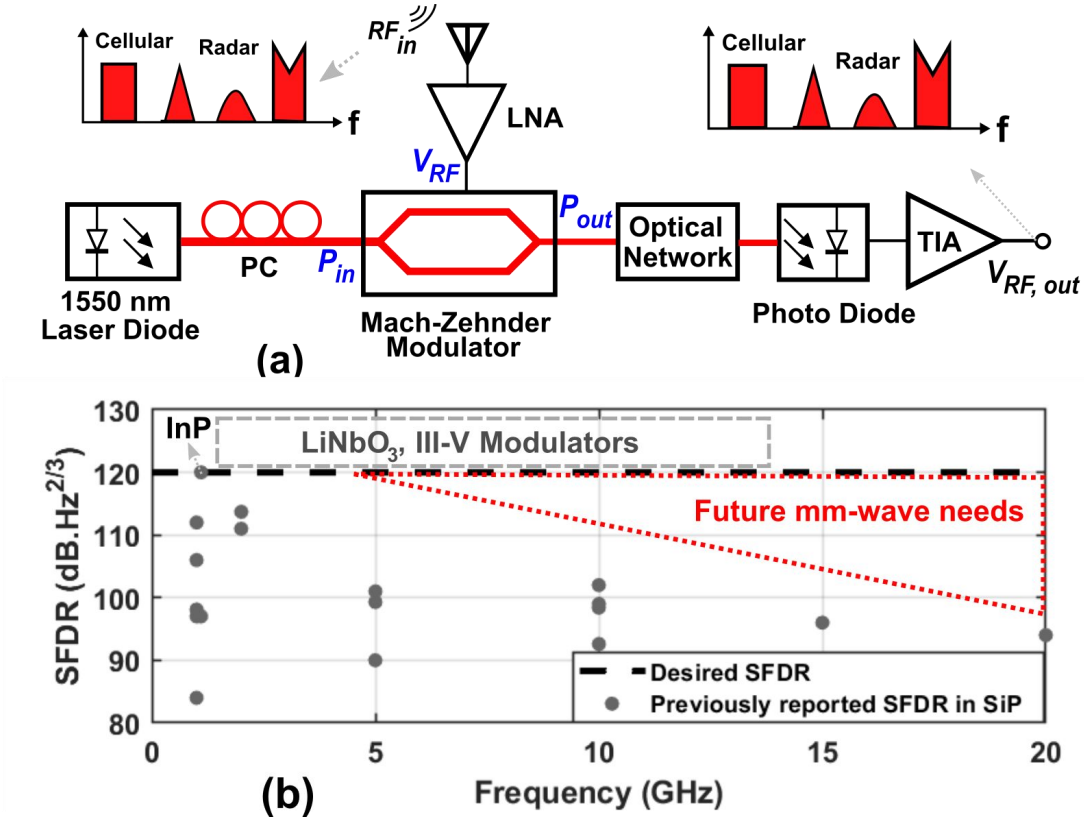

Figure 4.1: Block diagram of an RoF link with a SiGe LNA driving an MZM (top). Recently published SFDR results for SiP MZMs in RoF links. (bottom)

electro-optical (E/O) conversion using a Mach-Zehnder modulator (MZM). The RF-modulated optical signal is transported over fiber with little loss and converted back to the electrical domain through a photodetector. The linearity of the RoF link - as characterized by IIP3 - is typically limited by the V_π, the voltage required to change the optical carrier phase by 180°, of the MZM. While high V_π improves IIP3, it reduces the RF link gain and increases the noise figure (NF) resulting in no overall SFDR improvement of the RoF link [18].

Optoelectronic materials offer different fundamental limits on the $V_\pi L$ product of the MZM, where L is the length of the MZM arms. For instance, InP MZMs typically exhibit 4 V-mm, while SiP MZMs exhibit 15 V-mm due to the weaker change in the index of refraction induced by plasma dispersion. Larger $V_\pi L$ of the SiP modulator requires long

arms (L) to increase gain and reduce NF at the expense of frequency-dependent loss. Prior work illustrates that the SiP MZM has an SFDR of around 110 dB·Hz$^{2/3}$ at 1 GHz that reduces at higher frequency [57] as shown in Fig. 4.1(b). Therefore, a 20-dB SFDR gap exists between current SiP MZMs [13, 29–50] and the 120 dB·Hz$^{2/3}$ target, particularly in microwave bands extending to 18 GHz.

While SiP MZMs have higher $V_\pi L$, Si processes offer integration of the E/O RoF receiver in a monolithic platform for larger scale RF systems. Consequently, this work attempts to overcome the physical IIP3 limits of the broadband MZM with an electronic linearization scheme. Prior optical linearization techniques include optical-based approaches such as feedforward modulators and ring-assisted MZMs. While these approaches have demonstrated a 112 dB·Hz$^{2/3}$ SFDR at 1 GHz and 94 dB·Hz$^{2/3}$ SFDR at 20 GHz for a $LiNbO_3$ MZM [58], they typically also require discrete electronic components [59–61]. Prior work [62–64] proposed predistorter drivers as a radio-frequency integrated circuit (RFIC) for linearization of commercial $LiNbO_3$ and electroabsorption modulators and reported up to 19.5 dB 3rd-order intermodulation distortion (IM3) suppression. These improvements were limited to a maximum operation frequency of 1 GHz and did not explore linearization of SiP modulators which require significant compensation to rival III-V optical modulators.

Here, a broadband linearization approach based on electronic predistortion using 2^{nd}-order intermodulation products (IM2) injection within a distributed amplifier to compensate the nonlinearity of the SiP MZM and improve the SFDR to compete with $LiNbO_3$ or InP MZMs is presented. Three innovations are presented in this work. First, a distributed high-gain LNA is presented that covers 0.5-20 GHz to drive the MZM. Second, a distributed IM2 injection is demonstrated to reduce IM3 and linearize the cascade of the SiGe LNA and MZM. Third, a co-design procedure for a segmented MZM is described that predicts the broadband IIP3 and noise figure (NF) and supports the broadband lin-

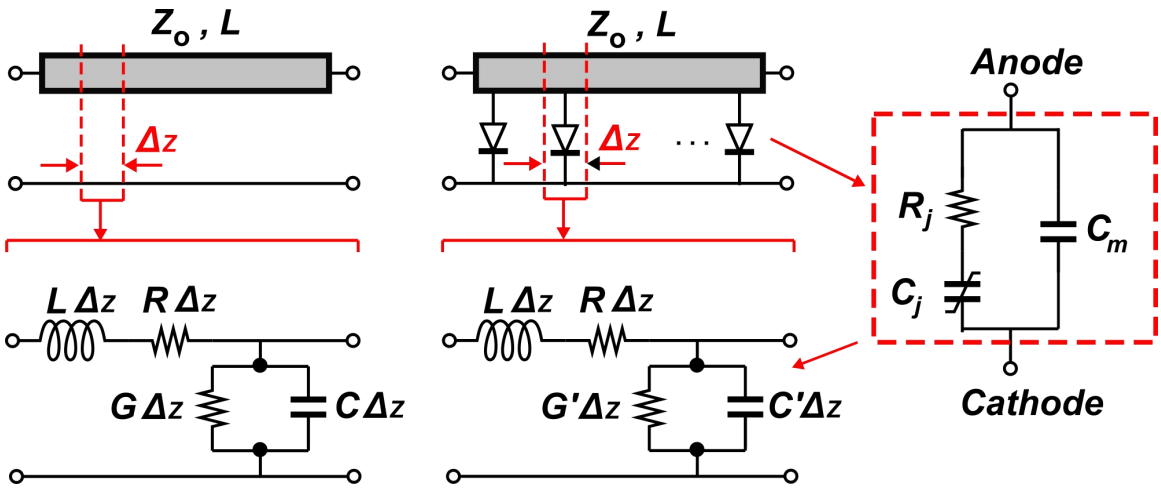

Figure 4.2: Loaded and unloaded transmission loss and corresponding lumped model for a small section

earization of the MZM. Prior work presented the circuit and initial measurements of the RoF link [65]. This paper extends this earlier presentation with analysis of the linearity of the co-integrated SiP MZM and SiGe LNA to calculate the IIP3 of the RF photonic receiver. We also present new circuit analysis that is corroborated with measurement to describe the power consumption of the linearization approach given the IM3 reduction. A record 120 dB·Hz$^{2/3}$ SFDR at 9 GHz and a response above 110 dB·Hz$^{2/3}$ to 18 GHz is demonstrated. The measured SiGe/SiP RoF indicates that the IIP3 improvement exists over more than 18 GHz, demonstrating the potential for broadband linearization.

4.2 Segmented MZMs for Broadband RF Response

SiP MZMs produce optical response through a change in the charge concentration in a *pn* junction along the optical waveguide. The MZM absorbs the reverse-biased depletion capacitor into a transmission line that can generally be modeled as a lumped circuit network where the LC ladder network predicts microwave propagation characteristics. In order to model loss, series resistance and shunt conductance are added to the LC

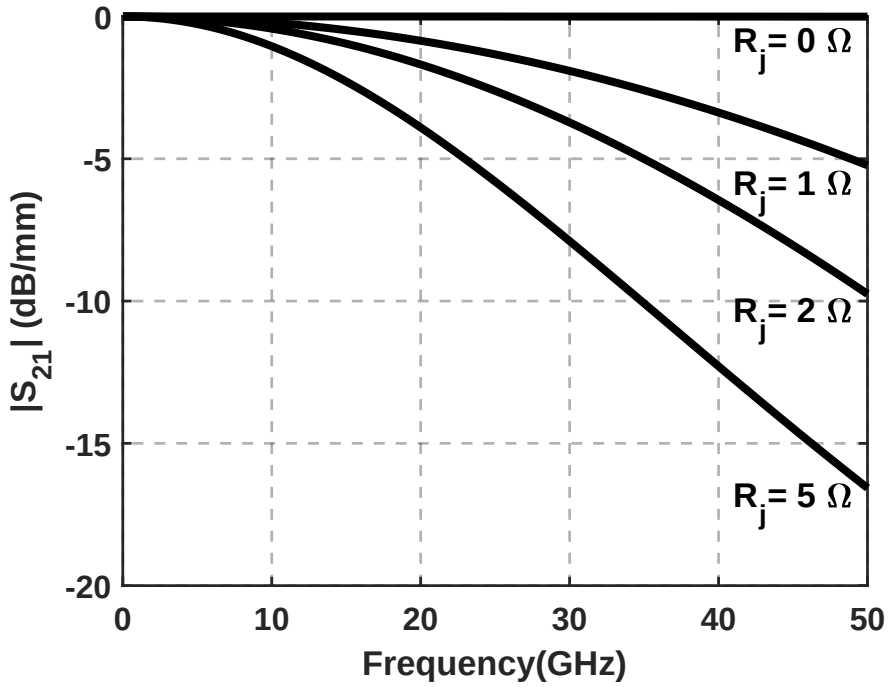

Figure 4.3: Insertion loss of a loaded transmission line as a function of frequency for different diode resistances.

network, where the former represents conductor loss and latter represents substrate loss. Fig. 4.2 shows unloaded and loaded transmission lines in the MZM and the corresponding lumped model unit cell, taking into account both conductor and dielectric loss. A small section of transmission line (Δz) is incorporated into the lumped model in Fig. 4.2, where Δz is the length of unit section. The attenuation constant per unit length and phase constant per unit length is

$$\alpha_{RF} \cong \frac{1}{2}\left(R\sqrt{\frac{C}{L}} + G\sqrt{\frac{L}{C}}\right) \tag{4.1a}$$

and

$$\beta_{RF} \cong \omega\sqrt{LC}. \tag{4.1b}$$

In an unloaded transmission line, the term $G\Delta z$ represent a large resistor, which models the conductor loss. The RF phase constant should be designed to match the optical traveling wave group velocity in a traveling wave MZM while the attenuation constant should be minimized to reduce the losses along the length of the line.

When the transmission line is loaded with a reverse biased diode, we can use the RC network model in Fig. 4.15 to find the new value for $G'\Delta z$. The series diode resistor R_j can be converted to a shunt resistor using series to shunt conversion for RC networks. With the new value of $G'\Delta z$, Fig. 4.3 plots the attenuation constant of a 1-mm long transmission line as a function of frequency for different values of R_j. Even a very small (2 Ohm) series junction resistance, α_{RF} induces a limited bandwidth and higher noise figure.

To improve the RoF link gain, a low V_π demands long MZM arms. However, the pn junction loss suggests that each arm should be under 1 mm to allow for a frequency response of 18 GHz. Therefore, the MZM transmission line of length L is broken into segments of less than 1 mm each. Consequently, the LNA should be distributed to allow a single transmission line input where the LNA buffers the signal as well as produces a differential drive signal to the two arms of the MZM. The LNA is a buffer between the transmission line and reverse bias diodes. The IL is improved resulting in lower NF for the system at high frequency.

A four-segment MZM shown in Fig. 4.4 is designed in 65-nm SiP technology, where each segment includes a differential p-i-n optical phase shifter to confine the optical field in the waveguide. While the S-MZM improves the 3-dB bandwidth compared to a TW-MZM, it does not improve the SFDR beyond 110 dB·Hz$^{2/3}$ [14]. To increase the SFDR further demands an active linearization approach to improve IIP3 that does not penalize NF.

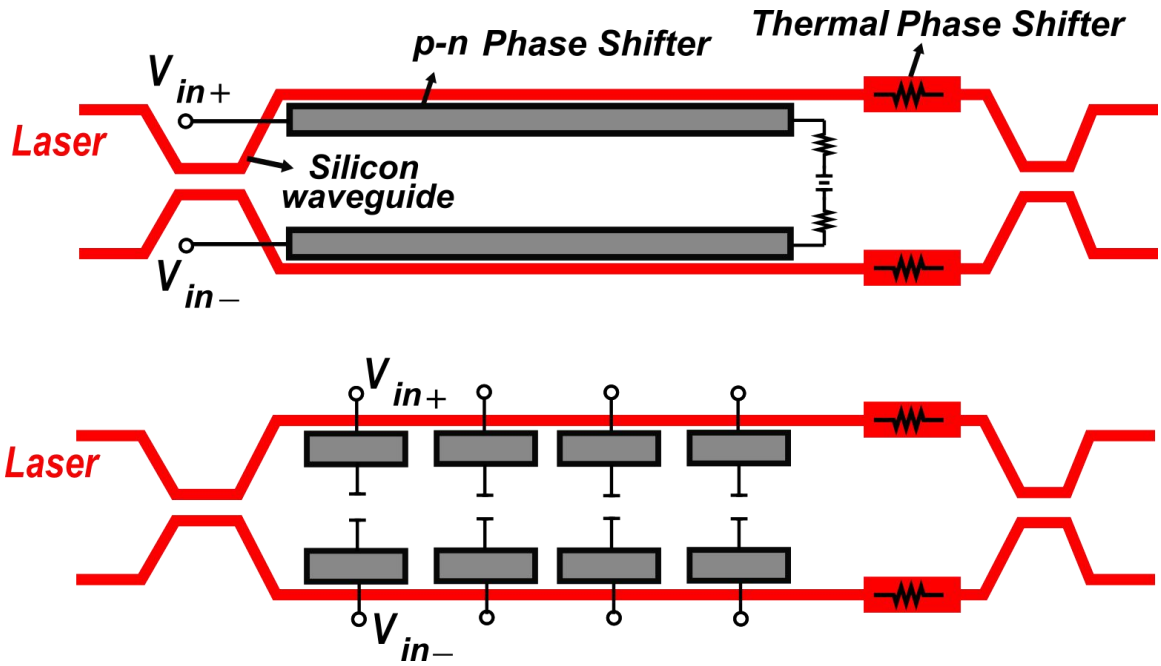

Figure 4.4: Comparison of E/O integration strategies based on MZMs using traveling wave design (top), and segmented design (bottom)

Figure 4.5: Block diagram representing a nonlinear model for distortion in the SiP MZM.

4.3 Takeaways from Distortion Analysis of SiP E/O Interfaces

The optical carrier travels with propagation constant $\gamma_{opt} = \alpha_{opt} + j\beta_{opt}$, where $\beta_{RF} \cong \beta_{opt}$. To modulate the optical carrier with the RF signal, the propagation constant has a linear dependence on the applied voltage such that $\alpha_{opt} = a_0 + a_1 V_i$ and $\beta_{opt} = b_0 + b_1 V_i$, where $b_1 = \frac{1}{V_\pi L}$. We will examine how the SiP MZM deviates from this model and produces distortion in the following sections.

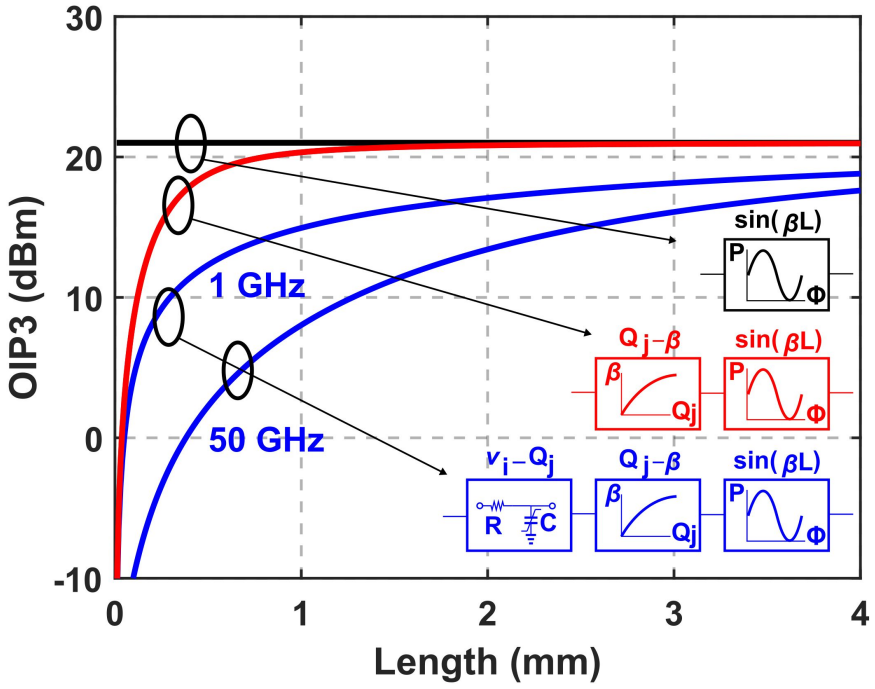

Figure 4.6: OIP3 as a function of MZM length for various cases considering different sources of nonlinearity, found from cascade analysis.

4.3.1 C-V Nonlinearity

Charge in the waveguide is modulated through a reverse-biased depletion capacitance, $Q = C(V)V$, where

$$C(V) = \frac{C_{J0}}{\left(1 - V/V_{bi}\right)^{m}}. \tag{4.2}$$

C_{J0} is the zero-bias junction capacitance, V_{bi} is the built-in potential, and m is the grading coefficient of the junction. The C_0 and C_1 are polynomial coefficients for (4.2). The capacitance nonlinearity is characterized by $IIP2_{VQ}$ and $IIP3_{VQ}$ and have been reported in prior work and summarized in Appendix I [14].

4.3.2 β Nonlinearity

The change in the charge produced by the depletion capacitance produces a change in the phase shift through the waveguide that is not necessarily linear but rather modeled by a higher-order polynomial. Rather than considering the voltage dependence on the phase constant, a charge relationship is used here to isolate the RF and optical sources of distortion.

$$\Delta\beta(Q) = \frac{2\pi}{\lambda}\Delta n_{eff} \approx \frac{2\pi}{\lambda}\sum_{k=1}^{m} q_k Q^k. \tag{4.3}$$

where Q_k is polynomial coefficient for the nonlinear index of refraction and λ is the light wavelength. The phase nonlinearity is characterized by $IIP2_{Q\beta} = |\frac{q_1}{q_2}|$ and $IIP3_{Q\beta} = \sqrt{|\frac{4q_1}{3q_3}|}$.

4.3.3 Cosine Nonlinearity

The optical transmission is determined by the differential phase shift between the two MZM arms. Additionally, a dc voltage is applied to the electrode that results in a static phase shift $\phi_D C$.

$$\frac{P_{out}}{P_{in}} = \frac{e^{-\alpha_{DC}L}}{2}\big(\cosh(2\alpha(Q)L) + \cos(2\beta(Q)L - \phi_{DC})\big), \tag{4.4}$$

The generalized model presented here characterizes the MZM by $IIP2_{\beta P}$ and $IIP3_{\beta P}$ to incorporate the transfer function from the junction capacitance nonlinearity and phase nonlinearity of p-n junction phase shifters [14, 19]. If (4.5) is assumed to be ideal with linear β with respect to the applied voltage and quadrature bias point, distortion is caused by the $\sin(x)$ transfer of V_i to P_{out} conversion. The output of optical transmission

is modeled with a third-order, memoryless nonlinearity.

$$\frac{P_{out}}{P_{in}} = c_1 v_i - c_3 v_i^3 = e^{-\alpha_{DC} L}\Big(\frac{\pi}{V_\pi} v_i - \frac{1}{6}(\frac{\pi}{V_\pi})^3 v_i^3\Big). \tag{4.5}$$

Consequently, the intermodulation distortion is characterized from $IIP3_{V\pi} = 2\sqrt{2}\frac{V_\pi}{\pi}$. For a 3-mm long SiP, the equivalent IIP3 is 26 dBm. Therefore, if we are dominated by the sine nonlinearity, the polynomial model is a memoryless, weakly nonlinear function and linearization of this characteristic is the primary role of broadband predistortion circuitry.

4.3.4 Cascade Nonlinearity Analysis

The block diagram in Fig. 4.5 represents both the amplitude and phase distortion in the MZM. Neglecting the amplitude path, which primarily generates only even-order distortion when biased at quadrature and driven differentially, a distortion cascade analysis for IIP3 combines each source of nonlinearity.

$$\begin{aligned}\frac{1}{IIP3_{MZM}^2} &= \frac{|A_1|^2}{IIP3_{VQ}{}^2} + \frac{|A_1|^2 C_0^2}{IIP3_{Q\beta}{}^2} + \frac{|A_1|^2 C_0^2 (\frac{2\pi}{\lambda} n_1)^2}{IIP3_{\beta P}{}^2} \\ &+ \frac{3}{2}\Big(\frac{C_1 |A_2|}{IIP2_{Q\beta}} + \frac{C_0^2 |A_1|^2 (\frac{2\pi}{\lambda} n_2) + C_1 |A_2| (\frac{2\pi}{\lambda} n_1)}{IIP2_{\beta P}}\Big).\end{aligned} \tag{4.6}$$

where $A_1(j\omega)$ and $A_2(j\omega)$ are Volterra kernels found for (4.2) and presented in Appendix I. The cascade analysis indicates how the components interact to produce a frequency-dependent distortion due to the capacitance of the waveguide. Considering the RF gain of the link is

$$G_{RF} = \sin\phi_{DC} e^{-\alpha_{DC} L} \frac{P_{in} \Re R_o}{V_\pi} \cong \frac{P_{in} \Re R_o}{V_\pi}, \tag{4.7}$$

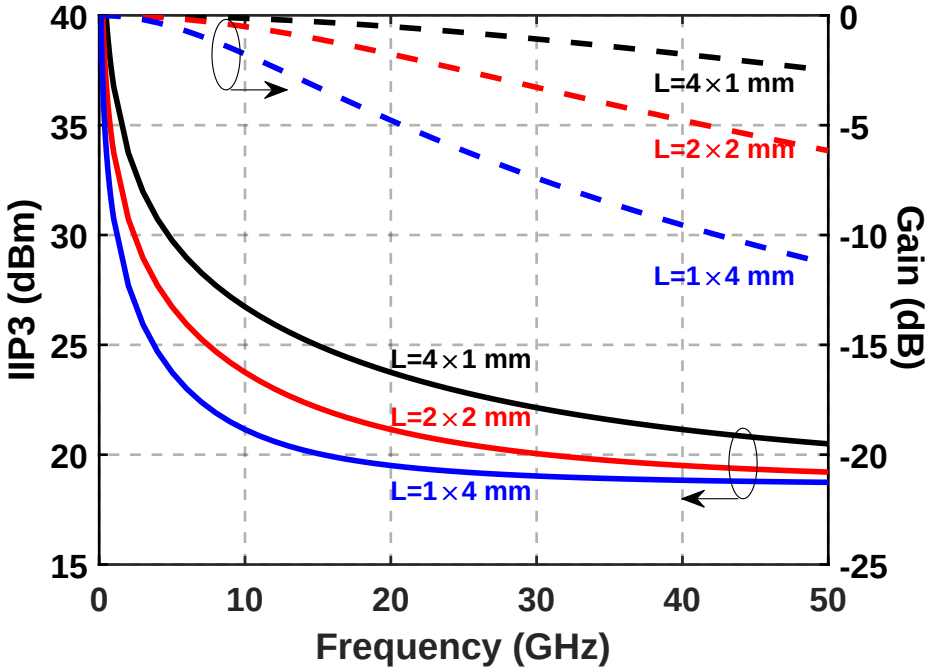

Figure 4.7: IIP3 and gain of the RC network using Volterra series for different configurations, where $L = N_{seg} \times L_{seg}$, as a fucntion of frequency.

where $\Re$ is the responsivity in A/W of the photodetector and R_o is the output resistance. The OIP3 is calculated from the product of IIP_{MZM} and G_{RF} and is plotted in Fig. 4.6. When considering only the V_π nonlinearity, the IIP3 is independent of length since IIP3 increases with V_π but the gain reduces with V_π.

When adding the β_{opt} nonlinearity, the OIP3 reduces for shorter MZM arms since a much larger voltage must be produced across the MZM diode capacitance and the large voltage produces a more nonlinear response in the phase constant. If we also include the diode depletion capacitance, the short length more significantly reduces the OIP3, particularly as the frequency increases. While we conclude that OIP3 improves for longer length, higher frequency loss is also increases as discussed in Sec. 4.2, which results in a trade-off between linearity and bandwidth.

4.4 Linearization Techniques for SiP Components

We propose three distinct RF linearization techniques for the O/E and E/O components specific to each source of nonlinearity presented in the previous section.

4.4.1 C-V Linearization

To mitigate the nonlinearity due to C-V variation in the depletion capacitance, the segments of the MZM allow the RC time constant of the segment to be tailored to reduce the generation of distortion. First, the design incorporates more fixed capacitance at each segment which reducing the contribution of the nonlinear C-V component. Additionally, a smaller resistance can be used to drive each segment to reduce the large voltage variation that results in IMD. In addition, biasing the junctions at higher reverse bias voltages will further reduce the capacitance and improves linearity. In a TW-MZM, junction capacitance and loading on the electrodes are optimized for E/O velocity matching and matching the characteristic impedance to the source impedance. These constraints move to other part of the design, the driver design, hence phase shifter loading can be optimized for linearity. IIP3 due to CV variation can be characterized by [14].

$$IIP3_{CV} = \sqrt{\frac{4}{3\omega R_i C_2}} \sqrt[4]{\frac{1+5\omega^2 R_i^2 C_0^2 + 4\omega^4 R_i^4 C_0^4}{1+\omega^2 R_i^2 (\frac{C_1^2}{C_2} + 2C_0)^2}} \tag{4.8}$$

where R_i is the load resistance. Fig. 4.7 illustrates IIP3 and gain due capacitance nonlinearity found from (4.8), and compared cases with one 4mm segment with two 2mm and four 1mm segments. As expected, gain roll-off increases as we increase the segment length, and hence capacitance. The IIP3 improvement is due to fixed load resistance being used for all three cases, which keeps voltage swings the same as well.

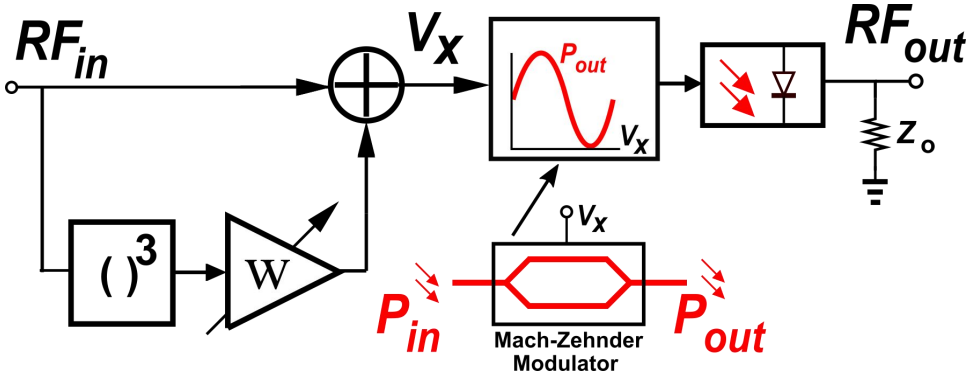

Figure 4.8: Concept of MZM linearization by third order predistortion

4.4.2 Kerr Effect Linearization

Prior work has demonstrated the linearization of the optical phase shift with induced voltage through engineering of the second-order optical response with respect to the electric field induced in the *pn* junction of the waveguide [56]. A *pin* junction diode is formed in the waveguide which introduces a Kerr effect (χ-2) dependence to the optical phase. Balancing the plasma dispersion and Kerr effect modulation linearizes the phase constant with applied voltage. Nonetheless, investigations SiP Kerr-effect MZMs have reported only slightly improvement of the SFDR at low frequency and no improvement higher frequency bands [57, 66, 67]. This is presumably due to the bottleneck in other sources of distortion.

4.4.3 Cosine Linearization

Since the $\arcsin(x)$ transfer function is frequency independent, a broadband predistortion circuit could linearize the MZM. The system shown in Fig. 4.8 is a cubic predistorter for linearization of the MZM. Here a second path generates a cubic term electronically which is then weighted by w and added back to the main signal before applying to the

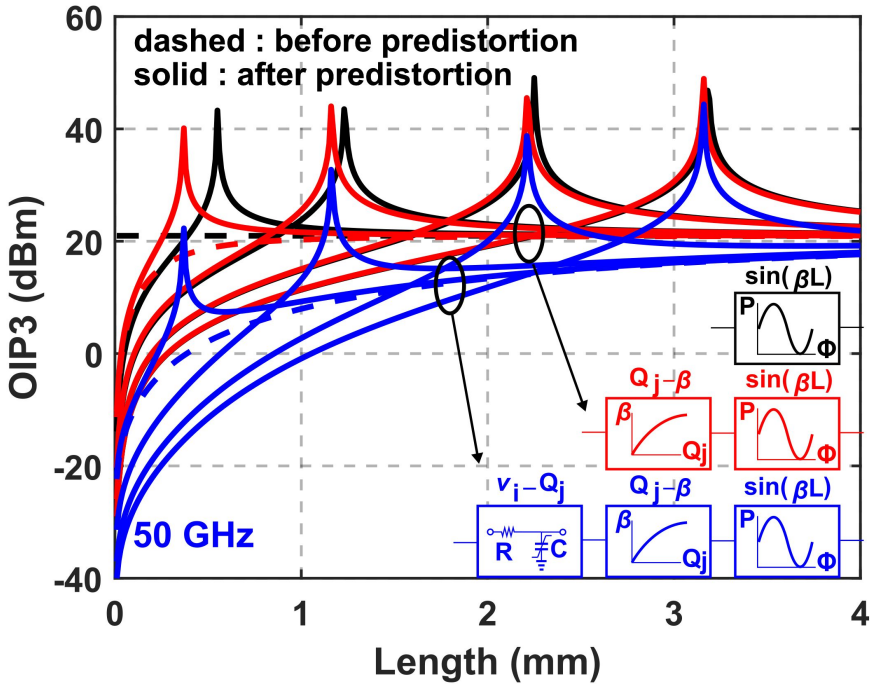

Figure 4.9: OIP3 as a function of MZM length when system is limited by different sources of nonlinearity (dashed), and after applying predistortion for different third order component weights (solid).

MZM. The predistorted signal is

$$v_x = v_i + wv_i^3 = v_i \cdot (1 + wv_i^2). \tag{4.9}$$

Applying this predistortion signal to the modulator results in

$$\frac{P_{out}}{P_{in}} = c_1 v_i + (wc_1 - c_3)v_i^3 - c_3 w v_i^5 - c_3 w^2 v_i^7 - c_3 w^3 v_i^9. \tag{4.10}$$

The $3^r d$-order term is eliminated when $w = \frac{c_3}{c_1}$ and the cubic polynomial generates a number of additional higher order terms. The effectiveness of this cancellation is demonstrated in the OIP3 plot as a function of MZM length for different values for w, represented in Fig. 4.9. For each device length, an optimum w produces OIP3 that

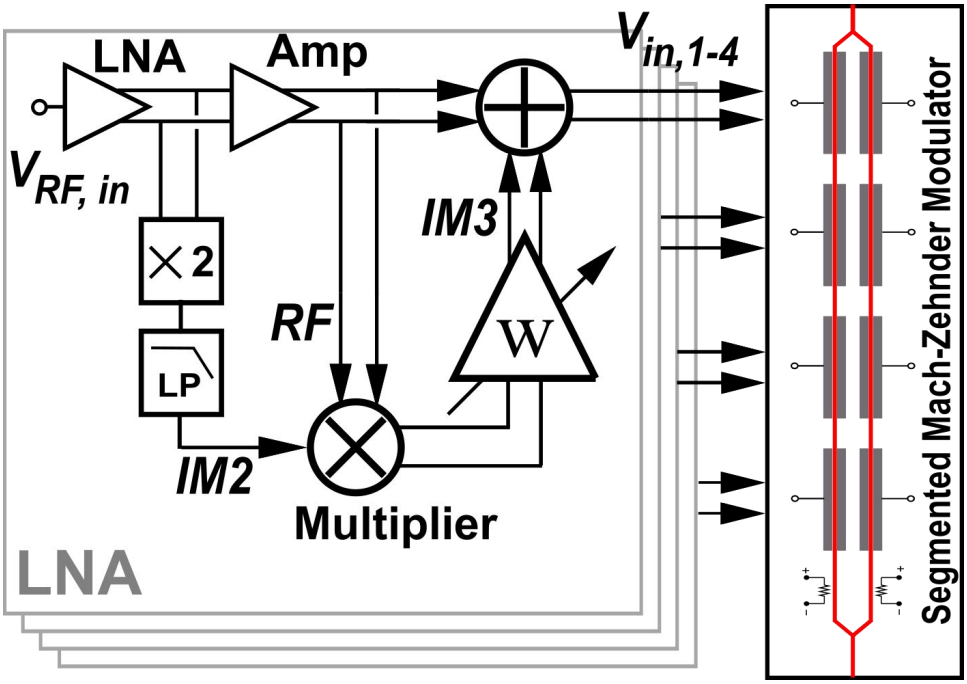

Figure 4.10: Conceptual illustration of the broadband linearization scheme with block diagram of distributed IM3 injection.

exceeds the original OIP3 (21 dBm) realized from the sine nonlinearity. Predistortion results in peaking for particular device lengths. Adding other sources of nonlinearity discussed in the previous sections results in red and blue curves in Fig. 4.9. Comparing these two figures indicates how secondary sources of nonlinearity, charge and phase shift, affect the overall OIP3.

Designing a broadband cubic term generator is challenging since the cubic nonlinearity generates signal components over 3 times the original signal bandwidth. Another approach to IM3 generation is to mix IM2 with original signal as indicated in the final equality in (4.9) to imitate a cubic term generator response, which we refer to as IM2 injection [68]. A broadband IM2 generator is realized from the intrinsic nonlinearity of a HBT device as is typically used in a frequency doubler. Since the squaring an RF signal at frequency ω_{RF} generates components at DC and $2\omega_{RF}$, we eliminate the components at $2\omega_{RF}$ with a low-pass filter. The remaining enveloped is modulated with the original

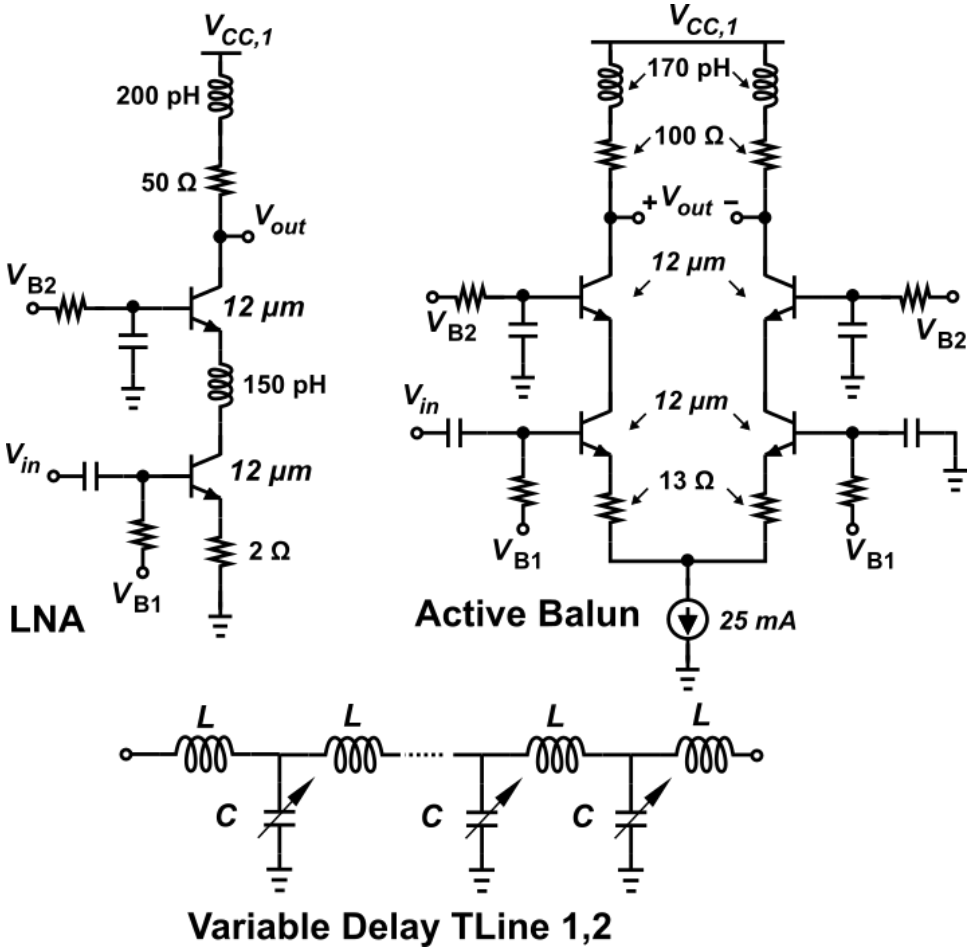

Figure 4.11: Circuit schematic illustrating the specific components including the single-ended LNA, wideband active balun, variable delay transmission line based on a LC ladder

RF signal and weighted to produce the desired IM3 term.

Fig. 4.10 provides a conceptual block diagram of the proposed distributed, analog predistortion LNA. The first block is the LNA with high gain to set the NF of the RoF and relax constraints on the length of MZM. The signal is then split between two paths. In one path, the RF signal is amplified while through an auxiliary path the RF signal is squared and filtered to generate a low-frequency IM2 component. Next, the IM2 component is mixed with the original RF signal to generate an IM3 component that can be weighted and added to the original RF signal to cancel the IM3 components generated

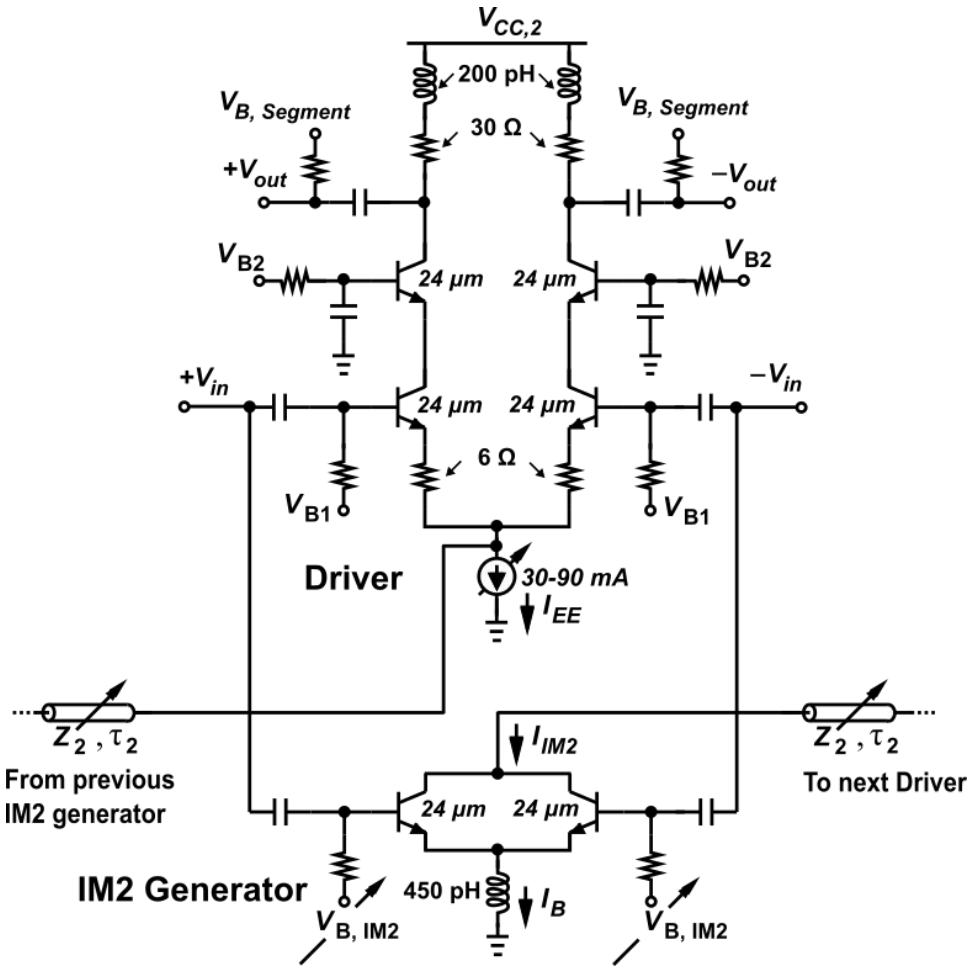

Figure 4.12: Circuit schematic illustrating the highly-linear differential driver and IM2 generator block

by the MZM. By adjusting the IM3 weight (w), the RoF can reached an IIP3 higher than the inherent MZM IIP3 as illustrated in Fig. 4.9.

4.5 Circuit Implementation

The distributed, predistortion stage illustrated in Fig. 4.10 is realized in an HBT technology. Fig. 4.11 shows the schematic of the LNA, active wideband balun, and tunable delay input transmission line. The wideband LNA is a resistively degenerated cascode stage with inductive peaking to extend the bandwidth. Resistive degeneration extends

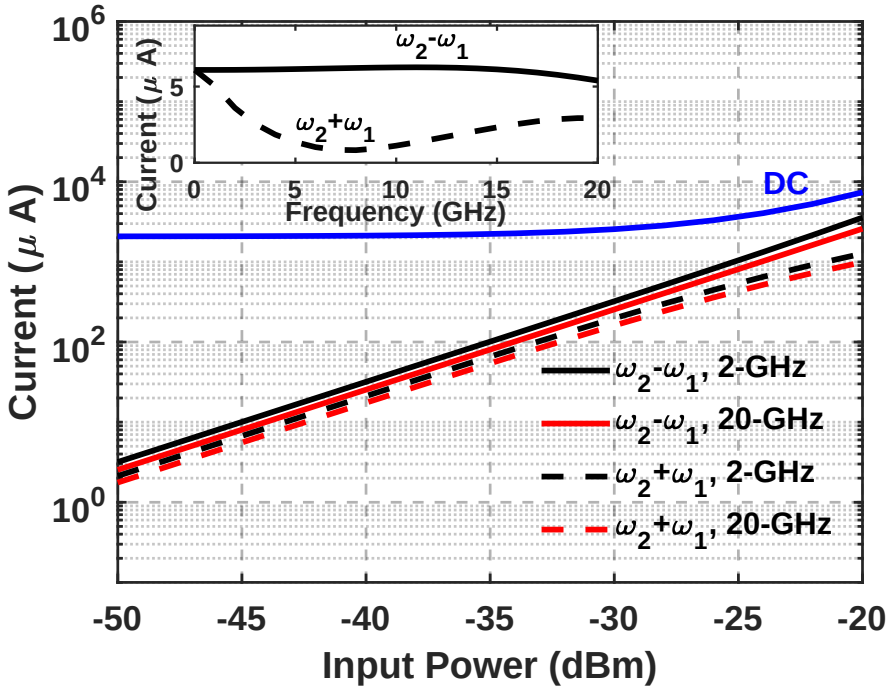

Figure 4.13: Current at $\omega_2 - \omega_1$ and $\omega_2 + \omega_1$ for the IM2 generator as a function of input power, at 2-GHz and 20-GHz

the broadband frequency response [69]. Next, an active balun produces differential RF signals with less than 1 dB amplitude and under 5° of phase imbalance up to 25 GHz [14]. To match the optical traveling wave velocity in the MZM with the RF traveling wave, the transmission line delay is adjusted over a small range with a varactor. The distributed design allows delay control between the RF input traveling wave line and the IM2 generation between stages.

Fig. 4.12 shows schematic of the linear, high-voltage differential cascode driver, which amplifies the RF signal to 2 Vpp to drive the *pin* phase shifter segments in the S-MZM along with the IM2 injection circuitry. The IM2 injection circuitry taps the differential signals and uses an inductively-degenerated frequency doubler to square and filter the IM2 products. The weighting and mixing function are produced by mirroring the IM2 current into the bias current of the high-voltage differential driver. The output current

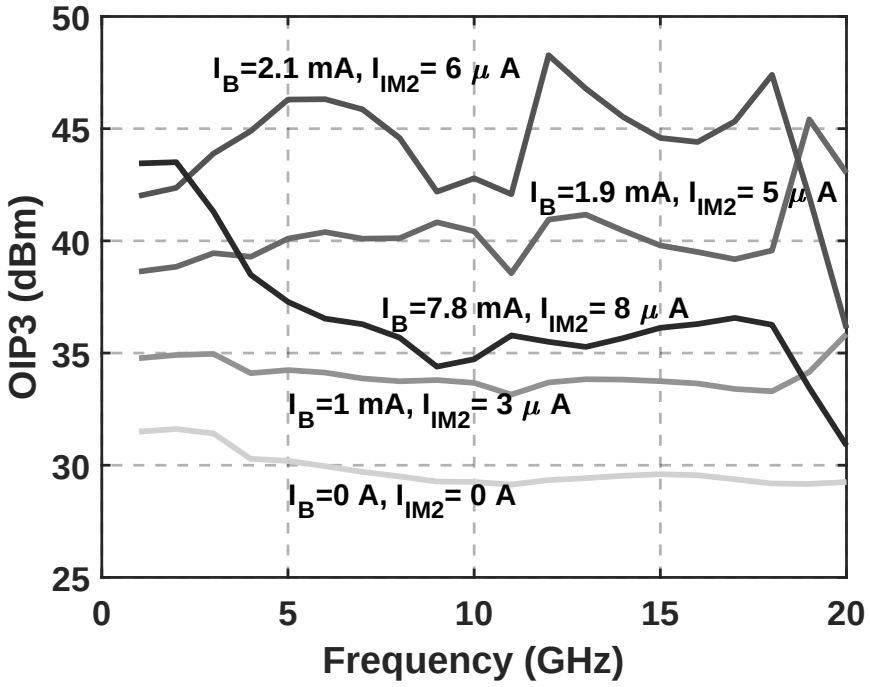

Figure 4.14: OIP3 of the driver as a function of frequency for different IM2 injection currents.

of the IM2 generator block, which is based on a frequency doubler, is composed of a DC and IM2 component.

$$I_{IM2} = I_B + \frac{I_B}{V_T^2}\left(\frac{v_{id}}{2}\right)^2 \tag{4.11}$$

where I_B is the DC bias current, V_T is the thermal voltage, and v_{id} is the amplitude of differential input voltage. If we drive the IM2 current generated with two closely-spaced tones at ω_1 and ω_2, current terms are produced at $\omega_1 - \omega_2$ and $\omega_1 + \omega_2$. Both IM2 components can be injected into the driver to produce IM3 components. Filtering of the sum components occurs due to the frequency response of the IM2 generator circuit. In Fig. 4.13, the inset plot shows the difference frequency current is constant to 18 GHz. The sum frequency is roughly 8 dB lower in the broadband IM2 generator.

The IM2 current is plotted in Fig. 4.13 for tones located at approximately 2 GHz and

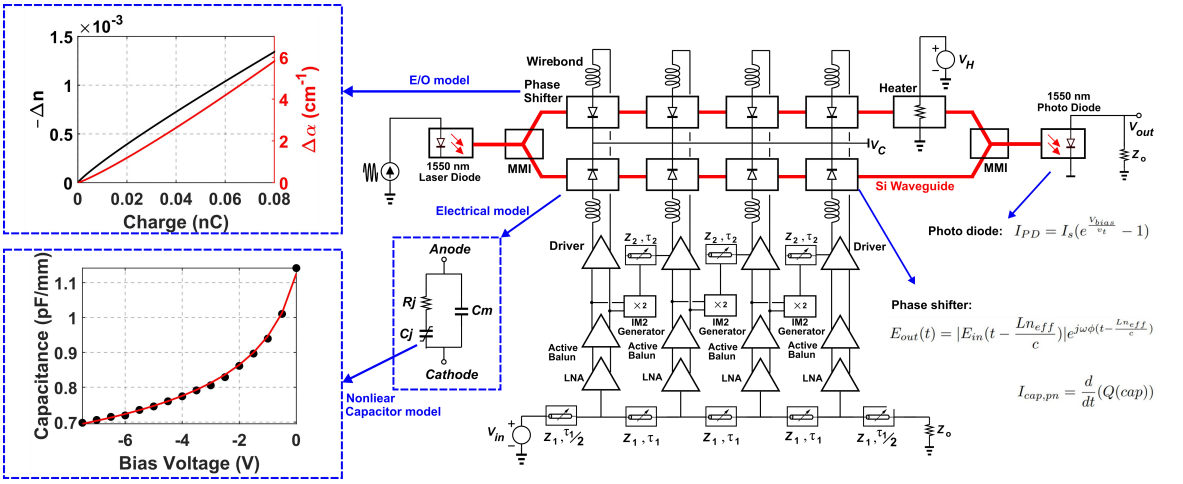

Figure 4.15: Electro-optic co-simulation test-bench based on Verilog-A models for SiP and BiCMOS process models.

20 GHz. The tone spacing is 100 MHz for the simulation and the DC bias current is 10 mA. The maximum IM2 current under this bias is 4 mA.

The output voltage of a differential BJT amplifier as a function of differential input voltage follows $\tanh(x)$ function. Therefore, predistorted output voltage for the circuit in Fig. 4.12 is

$$V_{out} = R_L\Big(I_{EE} + I_B + \frac{I_B}{V_T^2}\frac{v_{id}^2}{4}\Big)\tanh\frac{v_{id}}{2V_T}. \tag{4.12}$$

Representing the $\tanh(x)$ as a linear Taylor series equivalent,

$$V_{out} = R_L\big(I_{EE} + I_B + \frac{I_B}{V_T^2}\frac{v_{id}^2}{4}\big)\big(\frac{v_{id}}{2V_T} - \frac{1}{24}(\frac{v_{id}}{V_T})^3\big), \tag{4.13}$$

where we ignored higher-order terms generated by the tanh function. The desired predistorted signal is

$$V_{out} = V_{SW}\frac{v_{id}}{2V_T} + (I_B R_L - \frac{V_{SW}}{3})(\frac{v_{id}}{2V_T})^3, \tag{4.14}$$

where $V_{SW} = R_L\big(I_{EE} + I_B\big)$. Note that I_B is the desired weighting control that allows selection of the expansive IM3 products and can compensate distortion generated by the driver or the following MZM. Generally, we assume $I_{EE} + I_B \approx I_{EE}$.

Examination of the tanh indicates that it also produces undesirable 3^{rd}-order distortion. Consequently, by calculating gain and $IIP3 = \sqrt{\frac{4}{3}|\frac{a_1}{a_3}|}$ from (4.13), the OIP3 for the driver stage as a function of IM2 injection DC current is

$$OIP3 = 2V_{SW}\sqrt{|\frac{I_{EE} + I_B}{I_{EE} - 2I_B}|}. \tag{4.15}$$

The OIP3 is tuned through I_B and can cancel the self-generated distortion for $I_B = I_{EE}/2$. The injected IM2 current is relatively large suggesting high power consumption for the IM2 generator. For instance, a 1-V maximum swing requires 15 mA of I_B current. An alternative approach is to linearize the output driver such that the OIP3 can be improved to compensate the MZM nonlinearity. To include the role of R_E,

$$OIP3' \simeq OIP3\sqrt{(1 + \frac{(I_{EE} + I_B)R_E}{V_T})^3} \tag{4.16}$$

Fig. 4.14 shows OIP3 of the driver as a function of frequency for different IM2 injection current amplitudes demonstrating broadband improvement of OIP3. The average simulated OIP3 of the driver is about 43 dBm, an increase of more than 14 dB in the absence of IM2 injection.

4.6 Co-simulation of Electrical and Optical ICs

To co-simulate the RFIC and PIC, a Verilog-A library was developed for optical components including laser, silicon waveguide, splitter and combiner, *pin* junction phase

shifter, heater, and photodiode to capture the nature of the ideal and nonlinear behavior. With accurate behavioral modeling of the SiP MZM, the improvement in the OIP3 can be characterized.

Fig. 4.15 shows the co-simulation test bench including the driver and segmented MZM. A four-segment optical model for the SiP MZM is constructed in Cadence and is illustrated in Fig. 4.15. The sources of distortion as presented in Section IIIA-C. The nonlinear characteristics for the capacitance nonlinearity and phase and amplitude nonlinearity are included for the *pin* phase shifters. The capacitance change per applied reverse bias voltage is illustrated to the bottom left and was measured for the SiP MZM with an LCR meter. The capacitance changes from 0.7 pF/mm to 1.14 pF/mm. Additionally, the change in the index of refraction and attenuation constant with charge stored in the optical waveguide is plotted on the left of Fig. 15. To establish the linearity in terms of an RF output power, the MZM is connected to an ideal photodiode with responsivity of 1 A/W to produce an output current as terminated by a 50 Ohm.

The circuit schematic of the four-stage SiGe distributed IM2-injection LNA is illustrated in Fig. 4.15 based on the predistortion technique from Fig. 4.10. Each driver stage is co-designed specifically for the SiP segmented MZM stages. The input transmission line distributes the RF signal to the four LNA stages. The complete circuit schematic includes the LNA, active balun, driver and IM3 generation.

We simulate the OIP3 of the RoF link in Fig. 4.16 to indicate the benefit of the feedforward, distributed IM3 injection. The OIP3 is calculated in terms of RF power at the output of the photodiode found from electro-optical co-simulation of driver and MZM. In the absence of any predistortion, the OIP3 is around 5 dBm and rolls off around 10 GHz.

The use of predistortion with injection of IM2 components into the same stage indicates that the OIP3 is improved by 10 dB. However, the OIP3 is limited to under a few

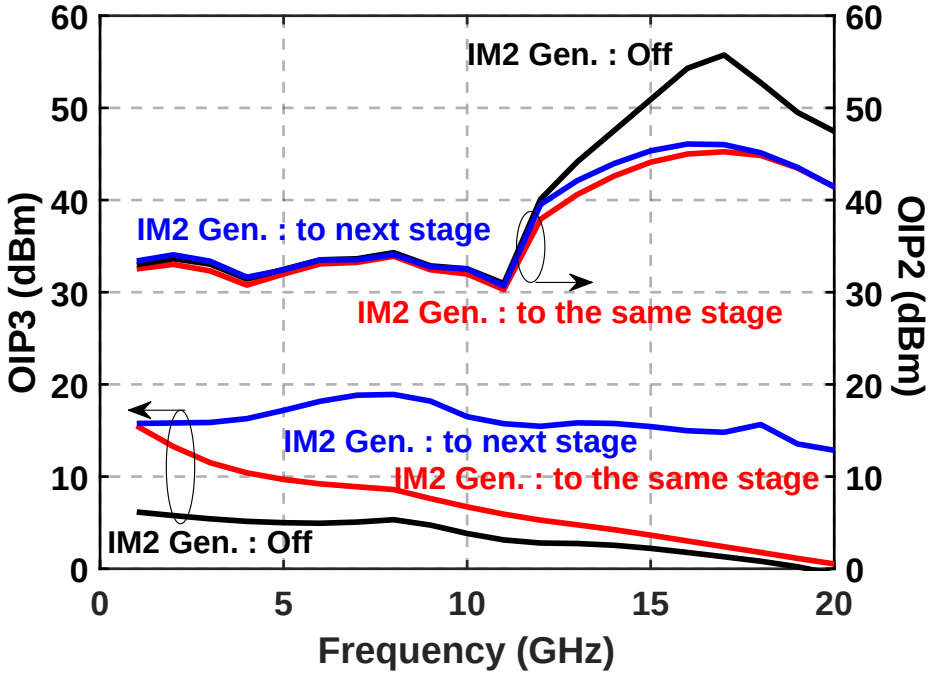

Figure 4.16: OIP2 and OIP3 found from electro-optic co-simulation of driver and MZM for three different cases: 1. IM2 off, 2. IM2 on and injected to the same stage, and 3. IM2 on and injected to the next stage.

GHz due to the timing mismatch between the RF signal and the IM3 products.

By injecting the IM2 component to the consecutive distributed stage, the time delay can be adjusted to achieve a broadband linearization. The OIP3 now remains above 15 dBm to 18 GHz. Consequently, the SFDR should be improved by more than 6 dB using the distributed predistortion scheme.

The co-simulated OIP2 is also plotted in Fig. 4.16. While there is a reduction in the OIP2 due to the injection of the IM2 term, all three cases indicate that the minimum OIP2 remains greater than 30 dBm from 0.5-20 GHz.

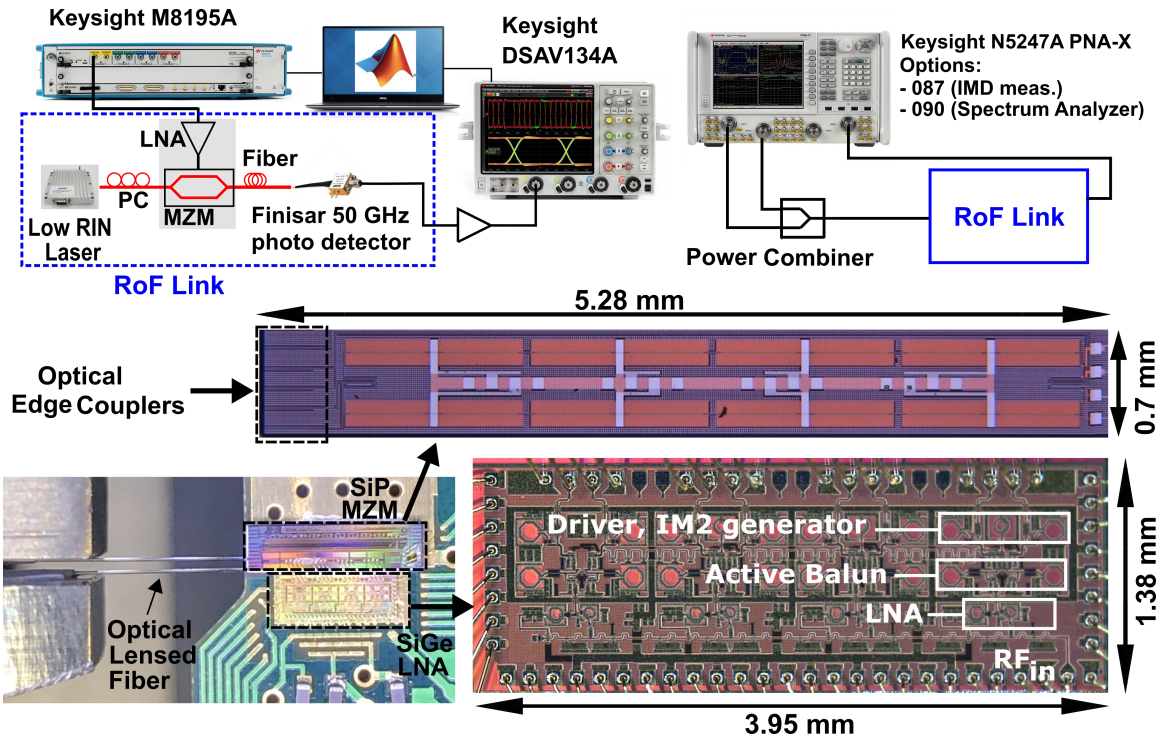

Figure 4.17: Measurement setups for link characterization with QAM signal (top left) and linearity measurements (top right), micrograph of the assembly (bottom left), SiP segmented MZM (middle), and LNA chip fabricated in 130-nm SiGe BiCMOS technology (bottom right).

4.7 Measurements Results

The SiP segmented MZM is fabricated in the 65-nm AIM silicon photonic (SiP) process and the broadband, low-noise driver is fabricated in the GlobalFoundries 130-nm SiGe BiCMOS technology. The SiP segmented MZM area is 5.5 x 0.65 mm^2 and driver chip area is 3.95 x 1.38 mm^2 and is shown in Fig. 4.17. The SiGe RFIC was designed using RF output GSSG pads with matching pitch to the MZM. The PCB assembly is illustrated in Fig. 4.17 with the SiGe distributed LNA and SiP MZM chips along with two 1550-nm lensed fibers used for optical interface with edge couplers. The two chips are assembled side-by-side on a PCB to minimize chip-to-chip wirebond length. The power consumption of the driver is 1.70 W (425 mW per stage) without IM3 predistortion and

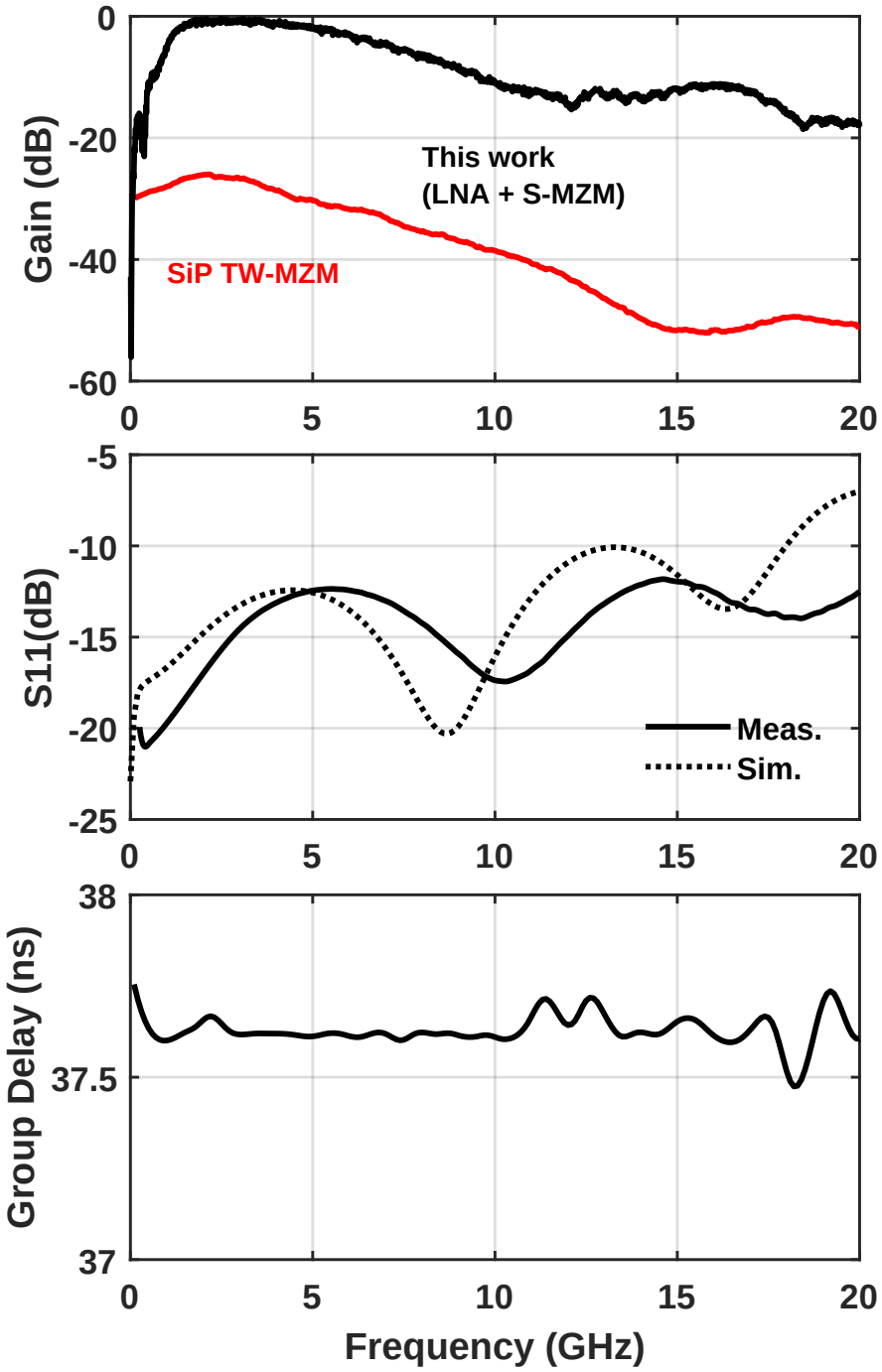

Figure 4.18: Measured RoF link gain compared to a single TW-MZM (top), simulated and measured input return loss (middle), and group delay as a function of frequency (bottom.

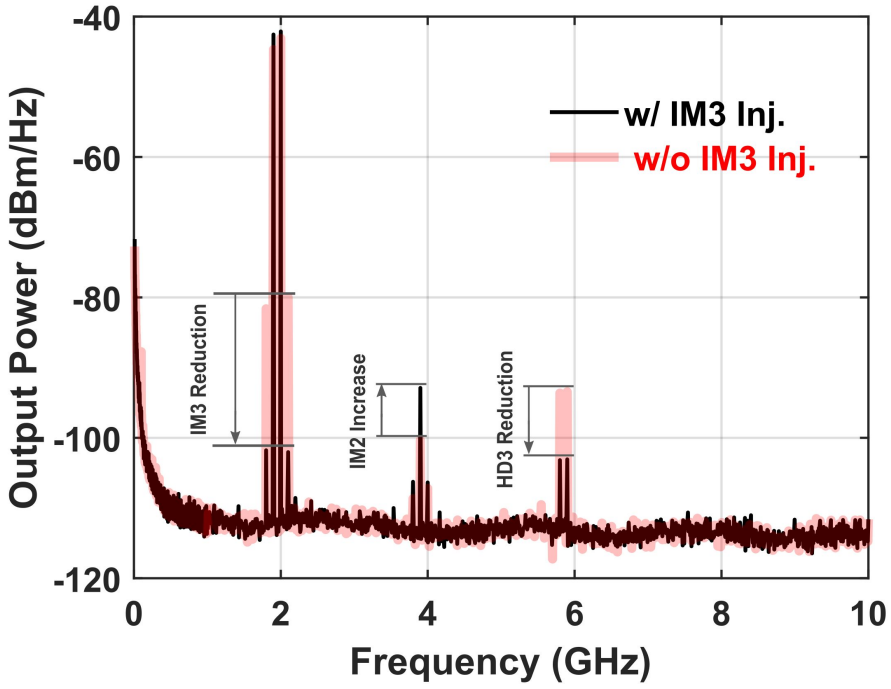

Figure 4.19: Measured power spectrum for two tones at 1.9 and 2 GHz at input of the driver

increases by 60 mW with the use of IM3 predistortion to provide the 10-20 dB IIP3 improvement. Most of the power consumption is consumed in the segment driver which is designed to produce 2 Vpp across the load resistor.

Fig. 4.17 provides a block diagram of the measurement setup with PNA-X, photodetector, micro-positioners, microscope for fiber alignment, and the PCB. Two different setups are used, one for small-signal and large-signal characterizations using PNA-X, and one for link characterization with modulated signals using an arbitrary waveform generator and oscilloscope.

A 1550-nm low-RIN laser drives the MZM in all measurements followed by a manual polarization controller. Measured loss for optical edge couplers is about 3-dB and total optical loss of MZM is less than 10-dB, including light coupling loss. The output of the MZM is sent to a 50-GHz dual band 1310/1550-nm photodetector, which generates an

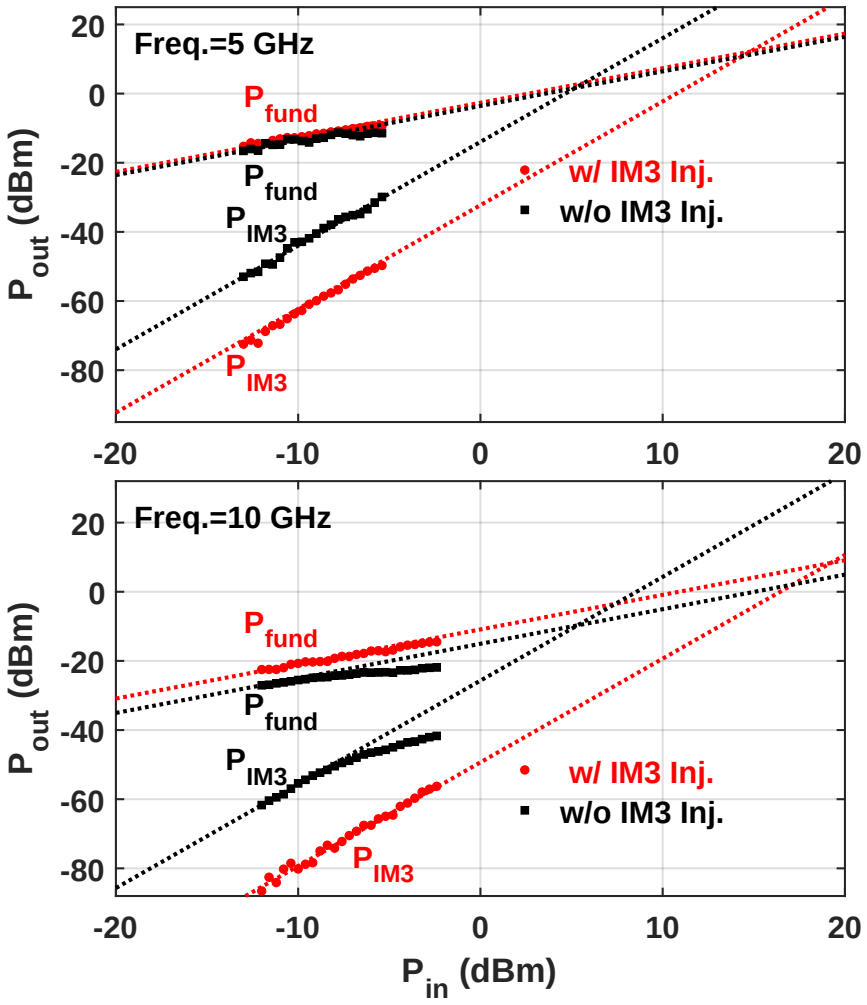

Figure 4.20: Input power sweep at 5 and 10 GHz with and without IM3 injection for fundamental and IM3 components.

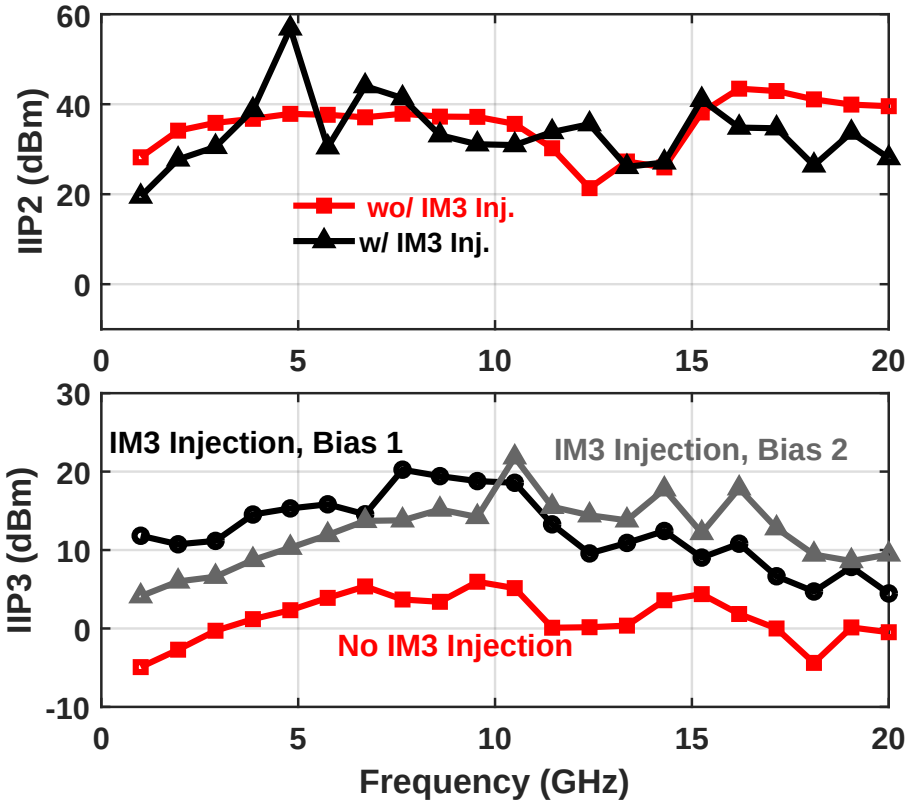

Figure 4.21: Measured IIP2 versus frequency before and after IM2 injection (top), and measured IIP3 versus frequency with and without IM3 injection at two bias points (bottom).

RF signal to the PNA-X.

Fig. 4.18 plots the measured S-parameters for the RoF link with an external high-linearity photodetector. The link gain is plotted against the measurement of a similar SiP TW-MZM in the same technology with the same length. The active driver improves the gain by 26 dB at 3 GHz and improves the gain by 40 dB above 15 GHz. This supports the advantage of the segmented design to improve the high-frequency response.

The simulated and measured input return loss are also shown in Fig. 4.18(middle), and the measured S_{11} is better than 10 dB to more than 20 GHz. The measured group delay is plotted in Fig. 4.18(bottom), and indicates low variation up to 24 GHz.

Fig. 4.19 graphs the measured output power spectrum for two tones at 1.9 and 2

GHz with and without IM2 injection. The two tones are generated by the PNA-X and combined into the driver. After applying IM2 injection and tuning the IM3 reduction manually in the driver, the IM3 components decrease by more than 23 dB while an IM2 term at 3.9 GHz increases by 8 dB. Additionally, the HD3 components are reduced by 10 dB, which demonstrates that the IM3 predistortion operates over a wide bandwidth.

The IM3 measurement is also characterized from the fundamental and IM3 over a range of input powers. Fig. 4.20 shows the input power sweep at 5 GHz and 10 GHz and indicates the predistortion improves the IIP3 by 10 dB and 14 dB, respectively. The weight of the IM3 component is controlled by bias current of IM2 generator and a slight increase in the injected fundamental power is observed.

Fig. 4.21 plots the IIP3 with and without IM2 injection at two different bias currents to demonstrate the linearization bandwidth. Over the entire 1-20 GHz range, the IIP3 is increased relative to the LNA without IM2 injection by at most 17 dB. The bias on the IM2 injection is adjusted to achieve higher IIP3 improvement above and below 10 GHz. The bias current of the IM2 generator block was 3.4 mA and 5.6 mA to get maximum IIP3 improvement in the 1-10 and 10-18 GHz bands, respectively.

For broadband (larger than an octave) systems, IIP2 is also a relevant metric. Since the IM2 generator injects IM2 components, the IIP2 is plotted as a function of frequency with and without IM2 injection. Notably, IIP2 does not substantially change over the frequency range with the IM2 bias current.

Fig. 4.22 plots the measured NF compared to the NF of a Si-based TW-MZM. The LNA improves the NF by more than 20 dB with a minimum 13.6 dB at 3 GHz. From the measured IIP3 and NF, the SFDR is 120 dB·Hz$^{2/3}$ at 9 GHz, a 19 dB improvement over earlier work and 22 dB improvement at 17 GHz. Fig. 4.23 compares measured wideband high SFDR achieved in this work against other works in the literature mostly exhibiting single frequency characterization. Here, the record high SFDR over bandwidth

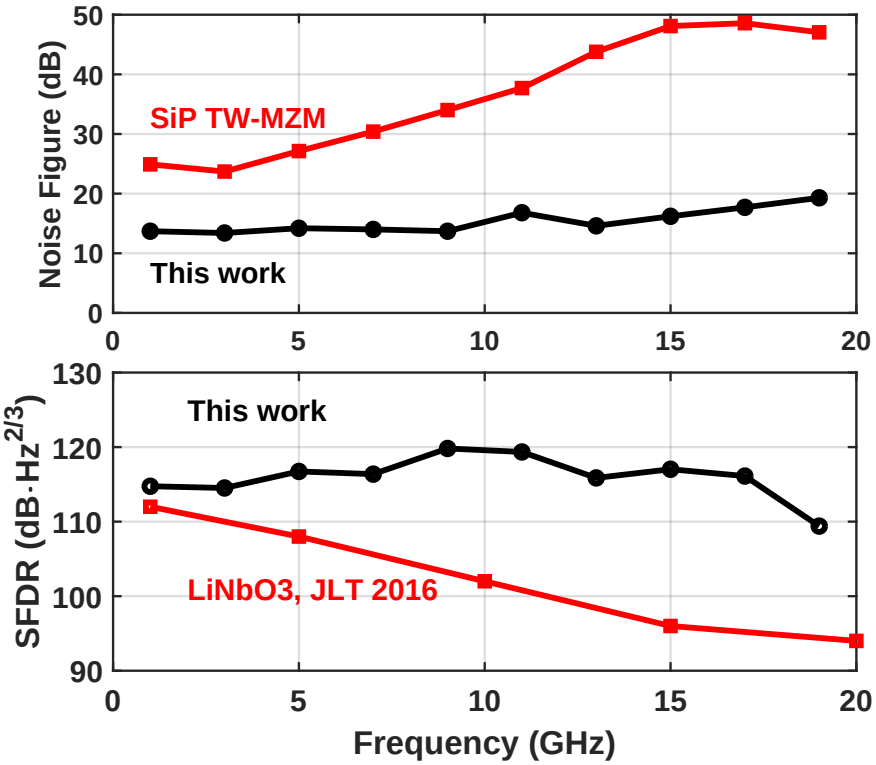

Figure 4.22: Measured NF of the RoF link compared to the NF of a Si-based TW-MZM (top), and calculated SFDR from measurement data and comparison with a LiNbO3 MZM with predistortion (bottom)

Table 4.1: State-of-the-art High SFDR RF Photonic Modulators

	[58]	[59]	[60]	[61]	[57]	**This Work**
Frequency (GHz)	1-20	12	1-18	2-20	10.9-12.9	**0.5-20**
SFDR (dB·Hz$^{2/3}$)	94-111	116	124	109-114	102-106	**109-120**
IIP3 (dBm)	2	18	42	2	23-24	**22**
NF (dB)	N/A	N/A	17-22	N/A	41-57	**13.6-19.3**
Technique	Discrete Predistorter	Dual Parallel MZM	Dual Series MZM	-	DC Kerr Mod.	**IM3 Injection**
Technology	$LiNbO_3$	$LiNbO_3$	$LiNbO_3$	$LiNbO_3$	Silicon	**Si-SiGe**
Integration	Discrete	Discrete	Discrete	Discrete	-	**Hybrid**

is achieved using a SiGe predistorter driver and a segmented silicon photonic MZM.

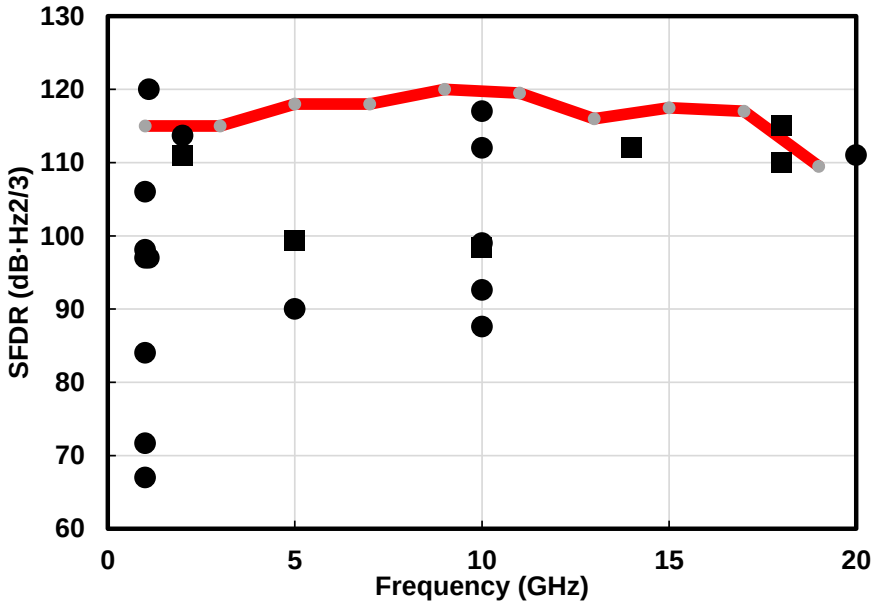

Figure 4.23: Measured wideband high SFDR achieved in this work compared to other works in the literature mostly exhibiting single frequency characterization.

The RoF link is also tested with a 2-Gbps QPSK, 16-QAM and 64-QAM modulated signals at carrier frequency of 11 GHz. For QPSK at 4 Gb/s, 16-QAM at 8 Gb/s, and 64-QAM at 16 Gb/s, measured EVMs are 2.6%, 3.7%, and 6.5%, respectively, which are measured without employing any digital predistortion.

This work is compared to earlier reported linearized MZM components or RoF links in Table 1. The presented work demonstrates the best SFDR for a SiP RF photonic link over the highest frequency range and puts silicon MZMs at a similar capability with reported $LiNbO_3$ modulators. Additionally, this is the first reported work based on an integrated electronic-photonic solution for RoF with small size and weight.

4.8 Conclusion

This work reports a co-designed SiGe LNA and SiP-based MZM for SFDR of up to 120 dB·$Hz^{2/3}$ and operating up to 20 GHz. A broadband analog predistortion scheme

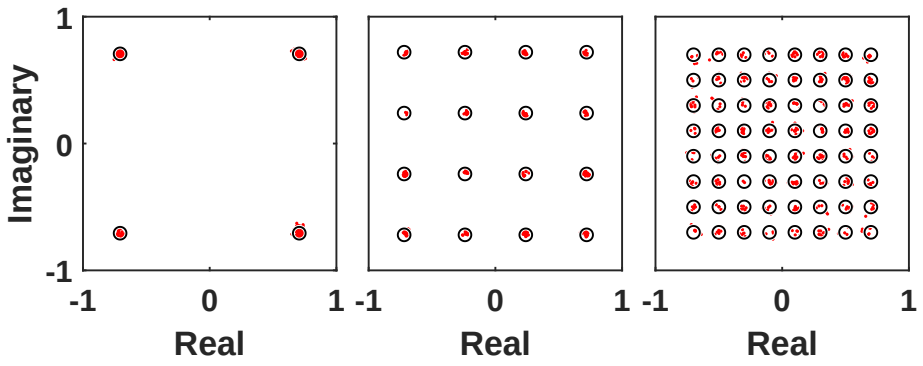

Figure 4.24: Measured QPSK (top), 16-QAM (middle), and 64-QAM constellation at 2 GS/s.

is introduced that forwards second-order intermodulation distortion products into the SiGe driver to eliminate third-order intermodulation distortion generated by the SiP MZM. The results demonstrate that SiP MZMs are capable of meeting high-performance criteria for RoF links and meets or surpasses commercial $LiNbO_3$ and III-V modulator performance. Prospects for future co-integration of Silicon Photonic and RF electronics on a single platform could support linearization of photonic devices.

Chapter 5

Co-design of an Integrated Optical Transmitter in 45 nm CMOS and 90-nm Silicon Photonics

5.1 Introduction

A variety of integration strategies are pursued for an optical transmitter [13, 70–74], as illustrated in Fig. 5.1. Conventionally, the MZM is constructed with traveling-wave electrodes that are driven from a separate broadband amplifier designed for the characteristic impedance of the MZM as shown in Fig. 5.1 (top). SiP-based p-n phase shifters exhibit large junction capacitance, which makes it difficult to design an electrode that is simultaneously velocity matched to the optical waveguide and impedance matched to 50 Ω. Additionally, the p-n junctions exhibit considerable junction resistance that loads the traveling-wave electrode, reducing the electrical bandwidth over long lengths.

These limitations can be addressed by breaking the traveling-wave electrode into smaller segments as shown in Fig. 5.1 (middle). While driving these segments individually

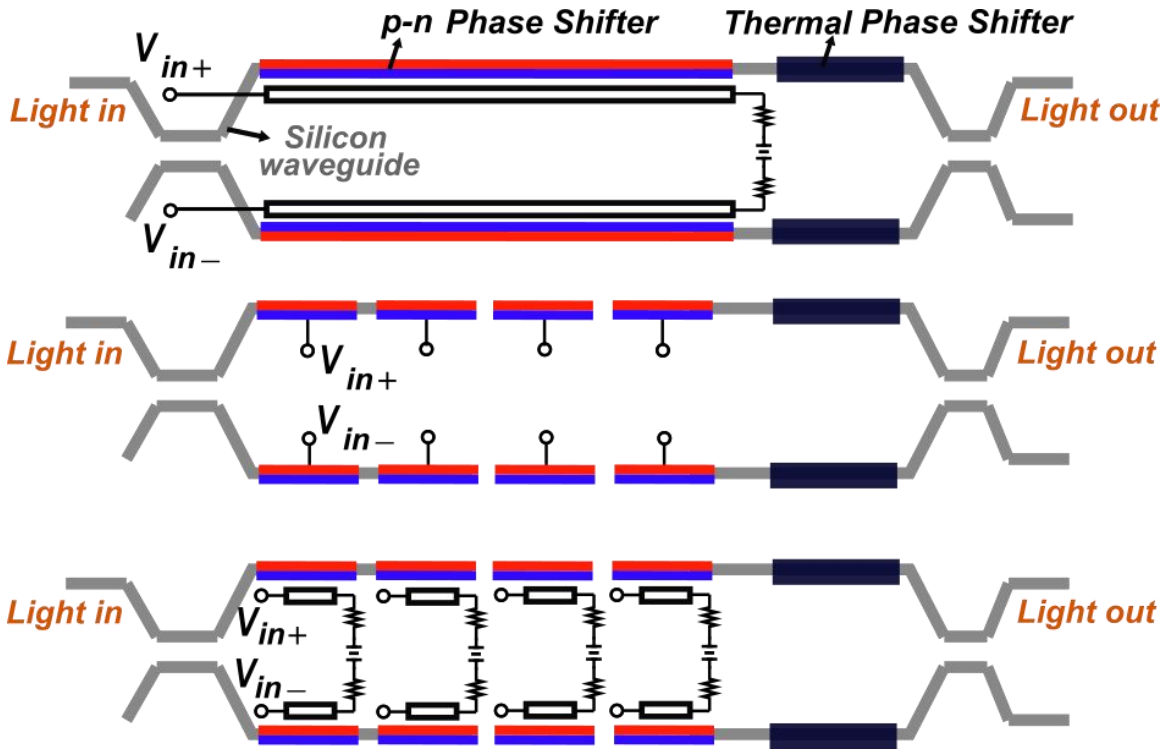

Figure 5.1: Comparison of E/O integration strategies based on MZMs using traveling wave design (top), segments (middle), and the proposed traveling-wave segments (bottom)

helps with increasing the bandwidth, the power consumption is increased as well as complexity of the driver integration due to the interconnection between the driver and the electrodes. If the length of each segment is electrically short, the bandwidth will be limited by RC, where R is the load resistance and C is the total output capacitance, which is dominated by phase shifter junction capacitance.

Here a traveling-wave segment (TWS) for the driver-MZM integration, illustrated in Fig. 5.1 (bottom), is proposed. Each segment consists of a shorter traveling wave electrode that is terminated on the SiP MZM. The segments are on the order of 1mm long due to the trade-off of bandwidth and power consumption. In Section 5.2, details of the MZM design is presented. In Section 5.3, DA schematics and simulations are demonstrated. Section 5.4 presents electrical and optical measurements.

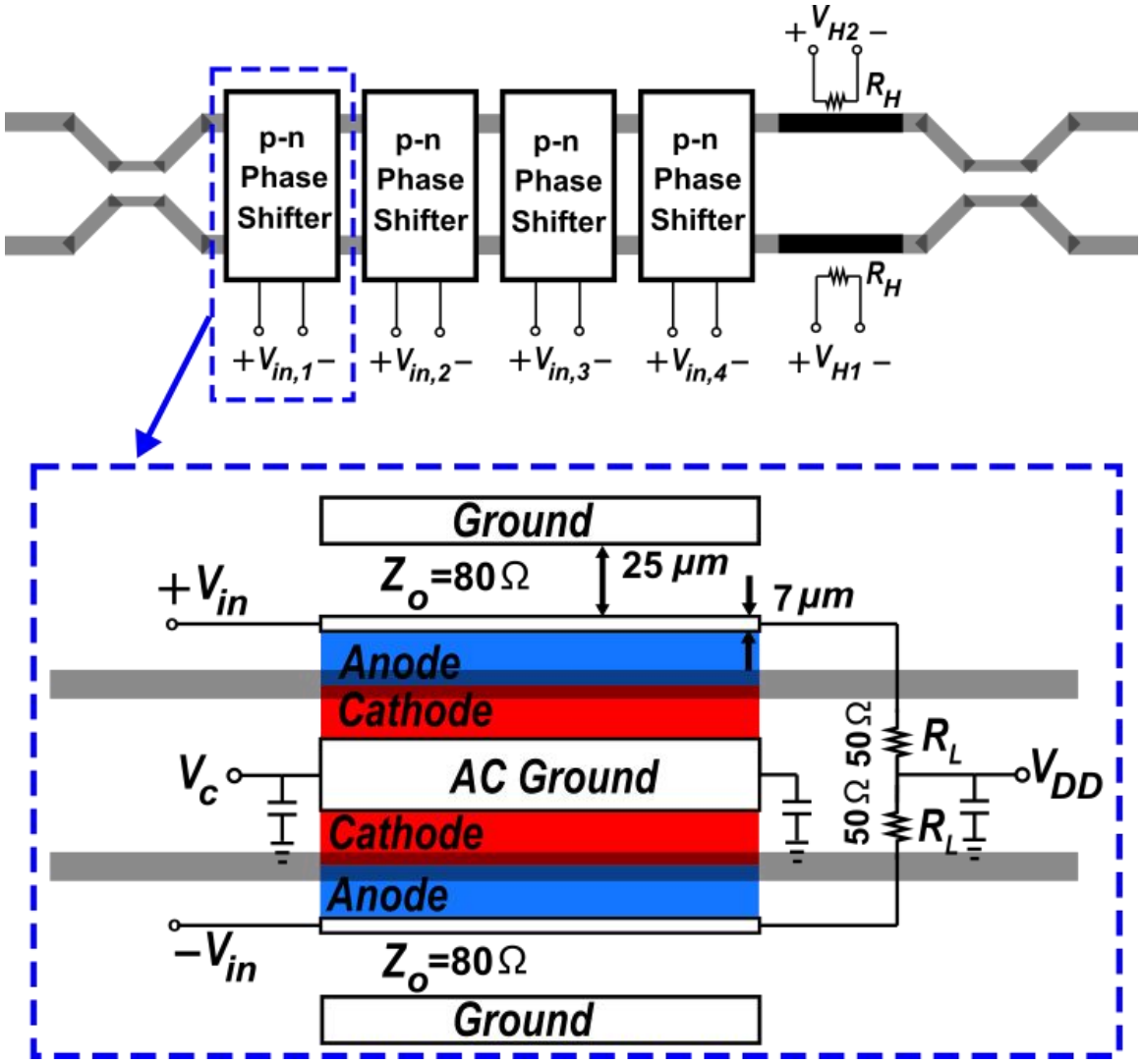

Figure 5.2: Proposed MZM design in 9WG 90nm CMOS technology (top), schematic of a single travelling wave segment (bottom).

5.2 Silicon Photonic Mach-Zehnder Modulator

The SiP MZM is implemented in a 90-nm (CMS90WG) CMOS SOI foundry using PDK-derived phase shifter elements, designed for 1310 nm wavelength. The MZM consists of 4 equal-length traveling-wave segments each 800 μm long. Fig. 5.2 shows the structure of the segmented Mach-Zehnder modulator as well as the co-planar waveguide (CPW) transmission line design.

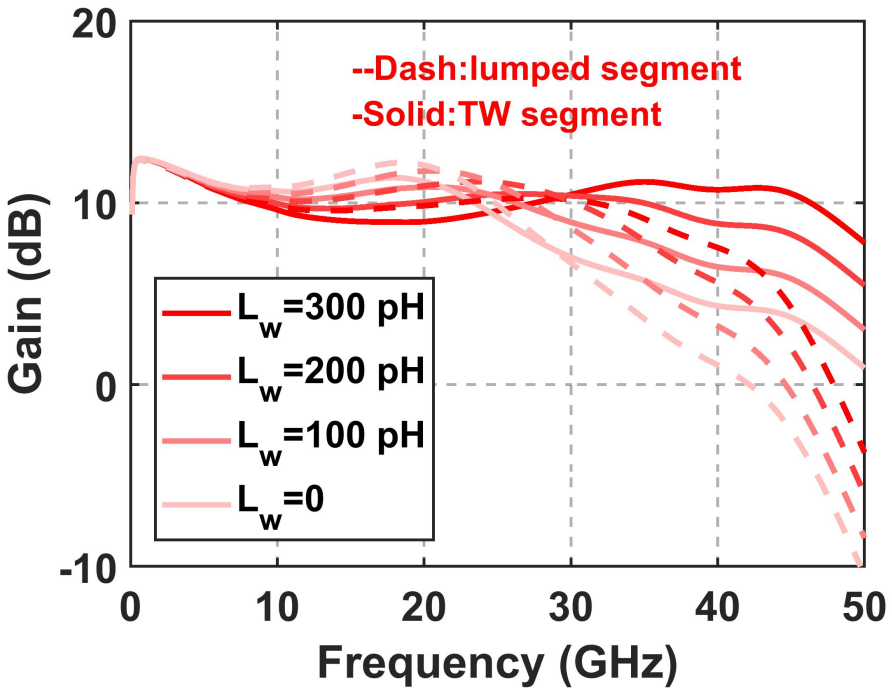

Figure 5.3: Effect of wirebond inductance on gain peaking at high frequencies for lumped segment and travelling wave segment loads.

A 3-dB directional coupler splits the optical signal equally between two branches. The phase shifters are based on reverse-biased p-n junctions. Heater resistors are inserted into each branch to bias the modulator at the quadrature point. The measured $V_\pi L$ was around 2 V.cm in this technology.

Accordingly, V_π for the designed MZM is 6.25 V considering total phase shifter length is 3.2 mm. Process simulations indicate a distributed junction capacitance of 400 fF/mm under 2 V reverse bias. To compensate for larger junction capacitance, a high characteristic impedance transmission line is needed. Hence, CPW is chosen over microstrip since it provides a larger characteristic impedance. Our modified CPW design uses a center ground connected to the cathode of both n-region of the junctions in both arms. This allows reverse biasing the anode based on the DC voltage that terminates the CPW lines.

In a segmented-MZM approach, the load resistor R for the driver is integrated in the

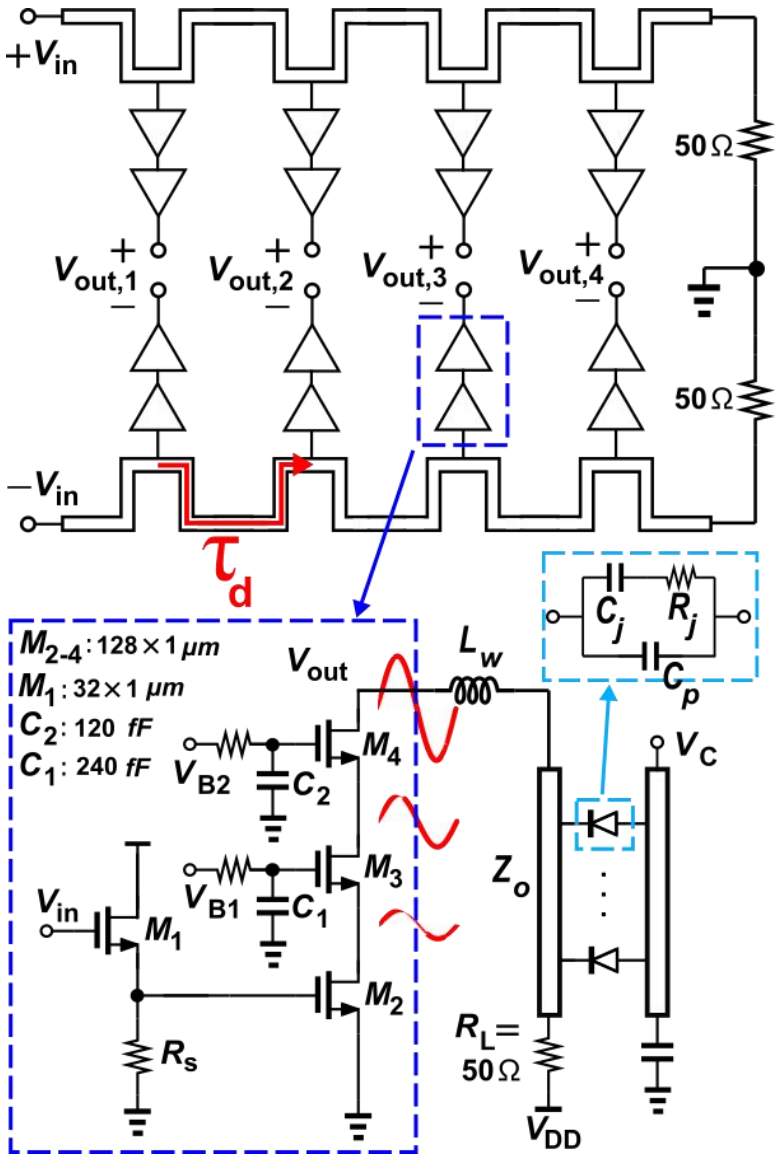

Figure 5.4: Block diagram of the distributed driver in 45 nm CMOS SOI technology (top), and schematic of the single driving stage and electrical model of p-n junction phase shifter (bottom)

driver stage [13, 14, 65]. By moving the load resistor to the MZM die, the bandwidth is improved since the wirebond inductance forms a π network with peaking at high frequencies. Moreover, the frequency response of the p-n junction phase shifter will not be bandwidth limited by RC, as each individual segment becomes a short traveling wave phase shifter, bandwidth limited by electrode loss. Fig. 5.3 shows simulated gain for the

two different cases: lumped segment load and traveling-wave segment load. In both cases, the wirebond inductance improves the 3dB bandwidth. Furthermore, the TWS design achieves a higher 3dB bandwidth. The higher mid-band gain of lumped segment case could reduce the the power consumption for low data-rates. However, smaller bandwidth will limit the highest data rate achievable with the lumped segment load.

5.3 45 nm CMOS SOI Distributed Driver

The schematic of the driver is shown in Fig. 5.4. To address the electrical/optical phase matching, the driver is based on a distributed amplifier. To provide wideband impedance matching, the driver uses an input transmission line to approximately velocity match the optical phase velocity in the MZM. The group index of refraction for the silicon waveguide is $n_g = 3.6$. Considering 900 μm pitch for segments, the required time delay (τ_d) in the input transmission line is $\tau_d = \frac{Ln_g}{c} = 10.8$ ps. The input transmission line in the driver chip is routed in serpentine fashion to match the time delay of the optical waveguide.

Each amplifier stage consists of source follower buffer followed by a 3-stack high voltage driver, providing close to 2.2-V single ended voltage swing. This corresponds to close to 0.7π phase shift for the transmitter. Supply voltage for the stacked FET driver is provided from the termination resistor in the modulator chip.

5.4 Measurements

The driver chip and MZM are fabricated in the GlobalFoundries 45nm CMOS SOI technology and SiP 9WG technologies, respectively. The micrograph is illustrated in Fig. 5.5. Each driver cell consumes 60 mW power, where about 4.5 mW is consumed in

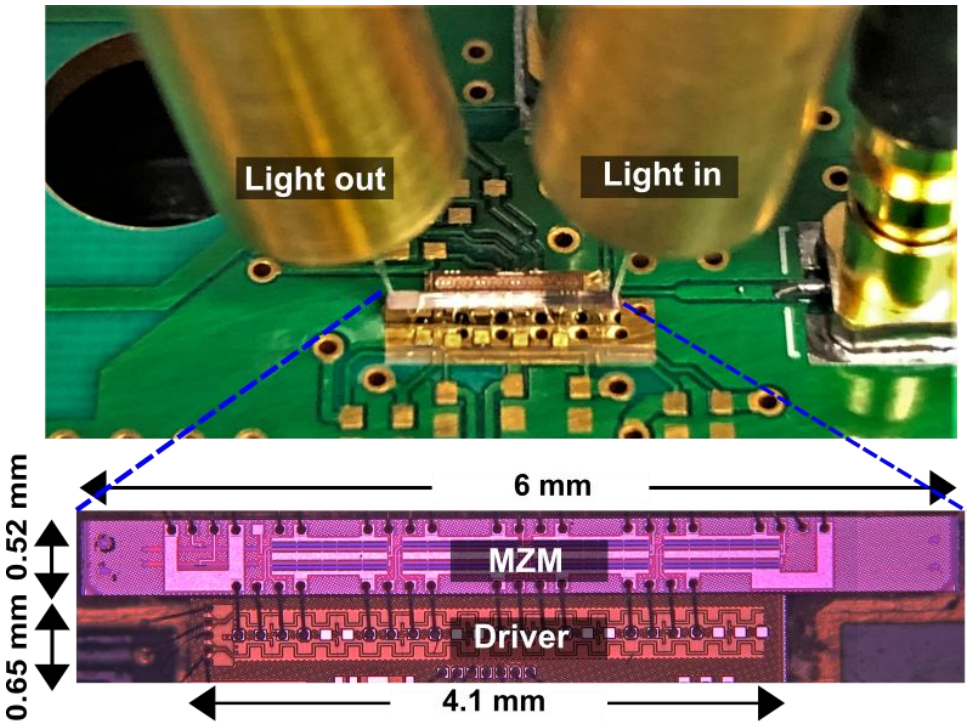

Figure 5.5: Opto-electronic transmitter assembly with SiP MZMs and CMOS distributed drivers

the source follower and 56 mW in the stacked FET driver.

To characterize the CMOS driver, the electrical frequency response is measured using Keysight's PNA-X and GGB probes. Four-port S-parameters are measured up to 35 GHz, where the gain of all 4 different outputs on the CMOS driver chip as well as input return loss are measured. The measured S_{11} and S_{21} for the driver chip are shown in Fig. 5.6 and are compared with simulation. Input return loss is better than 15-dB across the frequency band of 0-35 GHz, while the average measured S21 is 9 dB, with 3-dB BW of 26 GHz. Compared to simulation, S_{21} is lower at high frequencies which is mainly due calibration being done only for RF cables and not the probes, since input pad and output pads have different configurations (GSGSG and GSSG).

The driver chip and MZM are assembled closely on a MT40 PCB where the driver chip is elevated to shorten the chip-to-chip wirebonds. Mini-SMP connectors are used

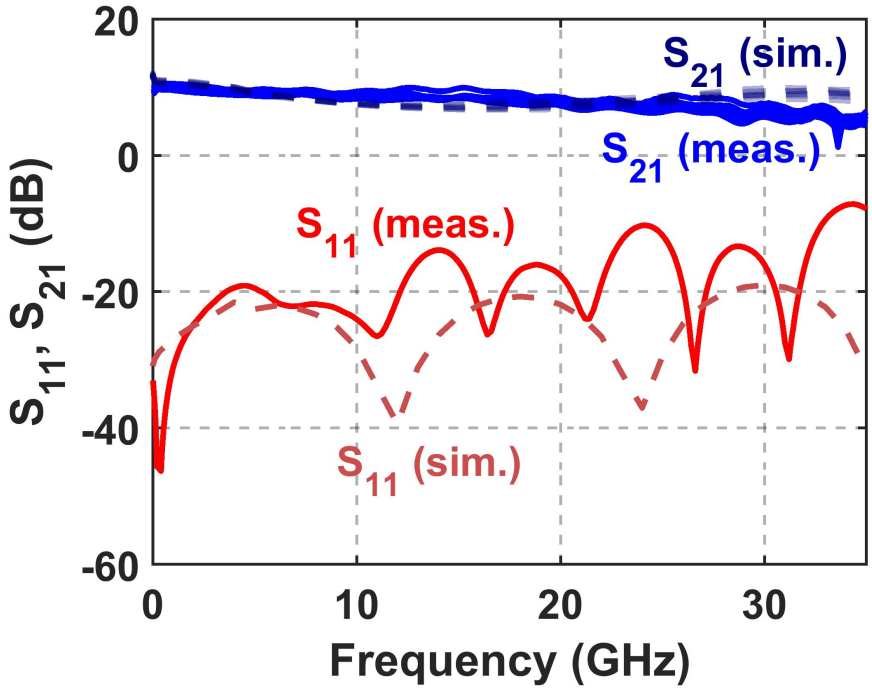

Figure 5.6: Measured and simulated S_{11} and S_{21} for four different outputs on the CMOS driver

on the board to supply input signal to the driver. A 13 dBm 1310 nm laser (Freedom Photonics) is coupled through vertical optical couplers to and from the grating couplers on the silicon photonic modulator. The measured optical power at the output of MZM is about -2 dBm, which corresponds to total 15 dB optical loss from the polarization controller, couplers and MZM. The output of the MZM is coupled to a 30 GHz Finisar photo-receiver which is connected to a sampling scope. A bit pattern generator is used to drive the transmitter with PRBS 31 pattern, with 550 mV maximum voltage. Bias-Ts are used to provide input bias voltage for the driver.

Measured eye-diagrams for the full link are shown in Fig. 5.7 for 20, 30, 40, and 50 Gb/s date rates with a PRBS-31 test pattern, where 2-tap FFE is utilized to enhance eye openings. The bit-error rate (BER) is measured by sweeping the sampling time. For 20 and 30 Gb/s, measured BER bathtub curves are plotted in Fig. 5.8. The BER is better

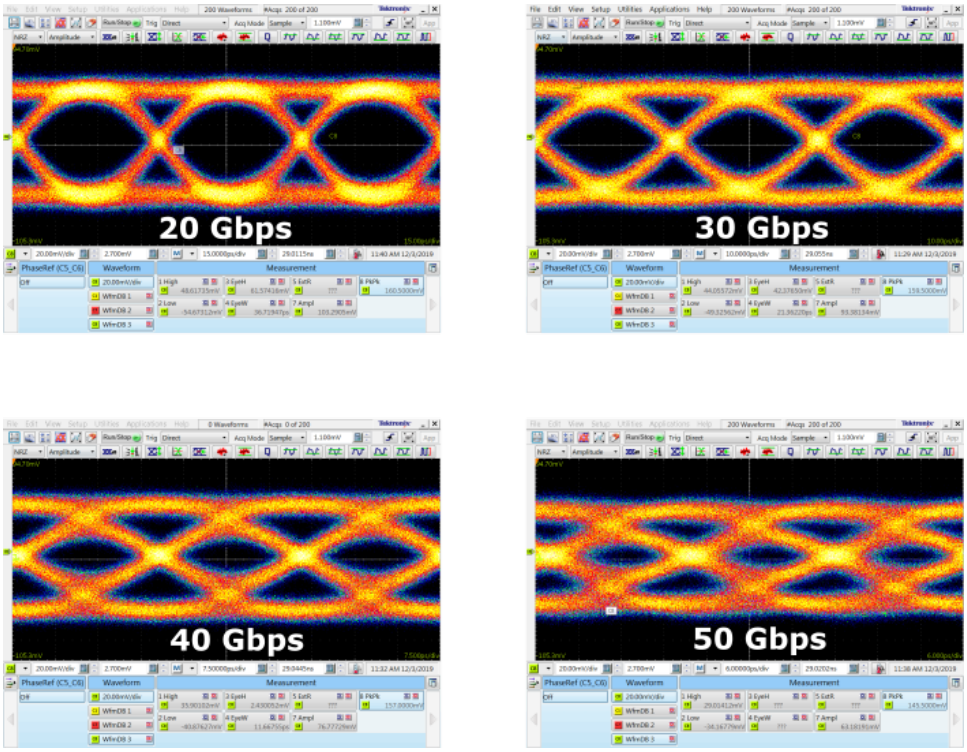

Figure 5.7: Measured eye diagram with PRBS 31 test pattern at 20, 30, 40, and 50 Gb/s data rates.

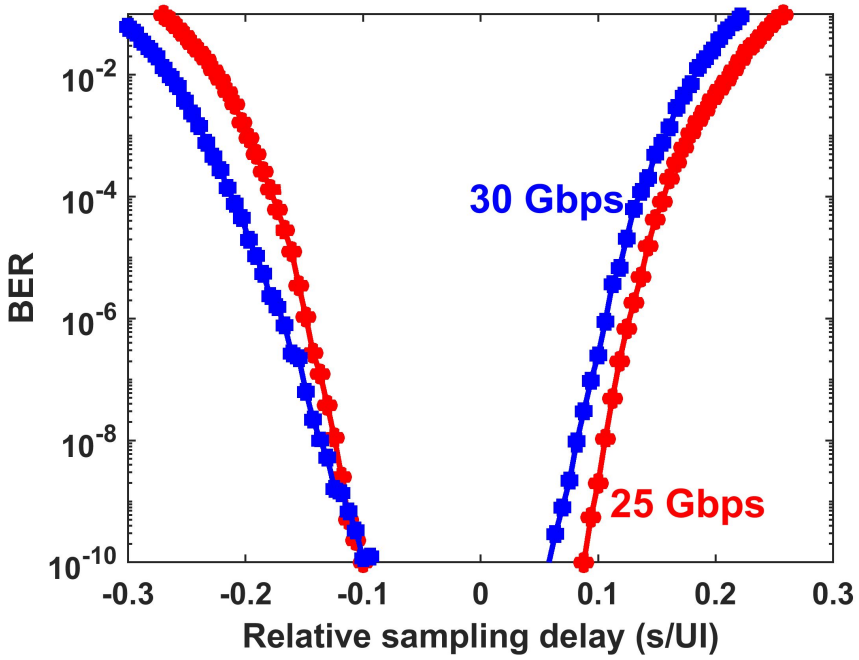

Figure 5.8: Measured BER at 20, and 30 Gb/s data rates

Table 5.1: State-of-the-art Comparison for CMOS and SiGe Optical Drivers

Parameter \ Reference	[70]	[71]	[72]	[73]	[74]	This Work
Technology	22 nm CMOS SOI	65 nm CMOS	0.25um BiCMOS	90 nm CMOS	28 nm CMOS	45 nm CMOS SOI
Data Rate (Gb/s)	30	30	2 × 37	20	44	50
Supply (V)	2	3.3	N/A	3	6	3
Energy (pJ/bit)	2.2	10.8	13.5	14	9.3	9.6
Test Pattern	PRBS 7	PRBS 15	N/A	PRBS 31	PRBS 31	PRBS 31
Integration with optic. Mod.	No	Yes	Yes	Yes	Yes	Yes

than 10^{-10} up to 30 Gb/s.

This result is compared in Table 1 with state of the art for CMOS and SiGe drivers. Note that not all the references have measured BER for optical transmitters. This work shows the highest data rate for optical transmitter based on CMOS technology, close to advanced BiCMOS transmitters and with relatively lower power consumption.

5.5 Conclusion

An integrated optical driver and Mach-Zehnder modulator is presented that operates to 50 Gb/s based on a traveling-wave segment driven from a 3-stack CMOS SOI driver. The optical eye is open to 50 Gb/s and indicates error-free operation to 30 Gb/s. The total circuit consumes 480 mW for an energy efficiency under 10 pJ/bit.

Chapter 6

A Monolithically Integrated Optical Transmitter in 90 nm CMOS

6.1 Introduction

One of the most challenging partS in opto-electronic co-integration is the interface between the electronic chip and photonic chip. Parasitics associated with interface, result of wirebonding or any other sort of assembly, have a high impact on the performance of the overall system at high frequencies. Monolithically integrated optical transmitters, on the other hand, are less susceptible to performance degradation due to packaging. There is growing interest in designing monolithically integrated electro-optical systems, with many works reported using III-V and silicon photonics integrated with CMOS or SiGe electronics. [75–94]. In this chapter a monolithically integrated optical transmitter is designed based on a novel topology that propose merging the driver into the optical modulator.

6.2 Architectures for Fully Integrated Optical Transmitters

In pursuing the goal to find the best architecture for monolithic integration of electronics and photonics, the available technology plays the biggest part. In this we look how to achieve maximum speed and efficiency using silicon photonic 9WG technology, which offers silicon photonic integrated with 90 nm CMOS. As the cut-off frequency of this process is not comparable to SiGe HBTs or more frequently used newer CMOS generations, design of a broadband amplifier is the next step. In this work, a distributed amplifier is chosen over inverter based drivers or a simple differential CMOS driver, as it takes advantage of bandwidth extension through absorbing transistor's parasitic capacitors in the transmission line.

There are three main scenarios to drive an MZM with a distributed driver as shown in Fig. 6.1. The first one discussed here is driving a travelling wave MZM with a matched distributed amplifier, as illustrated in Fig. 6.1a. The issue with this design is limited optical phase shift, as the DA itself occupy a large area and limits total active phase-shifter length. Hence, this design doesn't use the available area efficiently. We already know that phase-shifters in silicon photonics are not efficient and long phase-shifter are necessary to relax voltage swing requirement on the driver. The second architecture, shown in Fig. 6.1b, uses the familiar segmented MZM with a distributed driver. This design has already being used in chapter 3 and chapter 4. For high-speed optical transmitters, however, this design will not offer a fast driver for tho reasons: 1. limited speed of transistors in 90 nm technology, 2. The RC load will limit the bandwidth of the distributed amplifier, drain terminal parasites are no longer absorbed by a transmission line. Also, number of amplification stages in the DA needs to be increased as they need to drive a capacitive load. This will increase the power consumption of the overall transmitter.

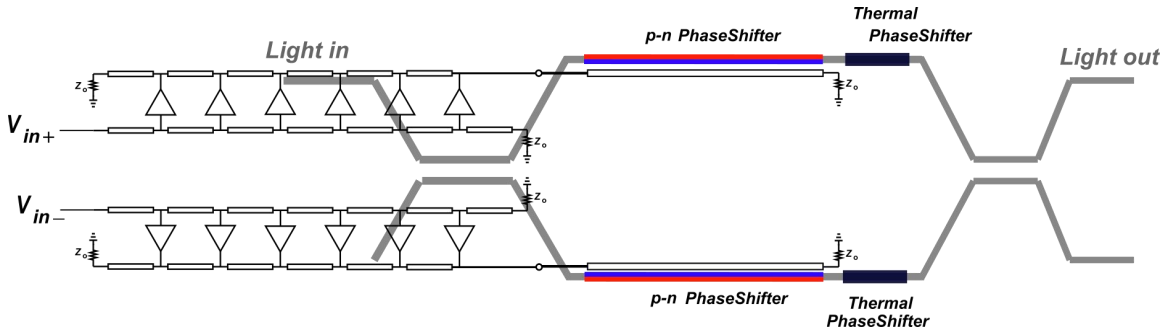

(a) Distributed amplifier driving a travelling-wave MZM.

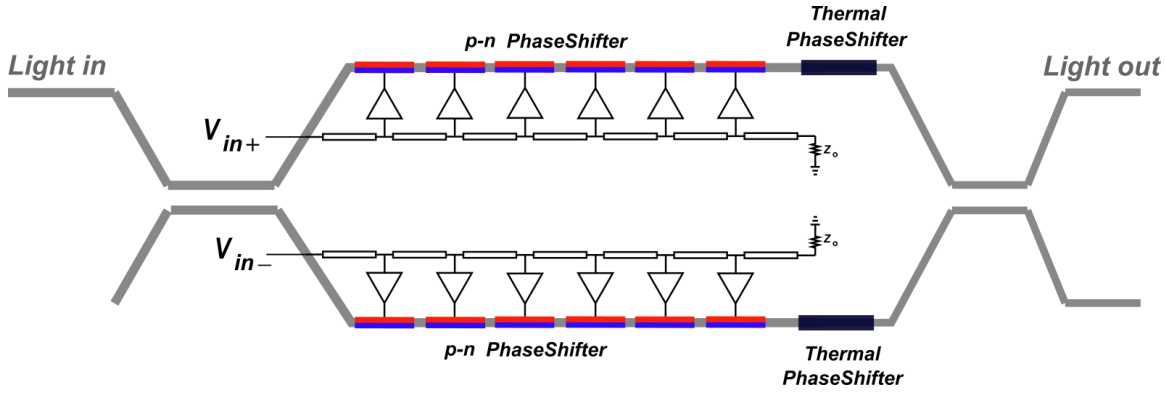

(b) Distributed amplifier driving a segmented-MZM.

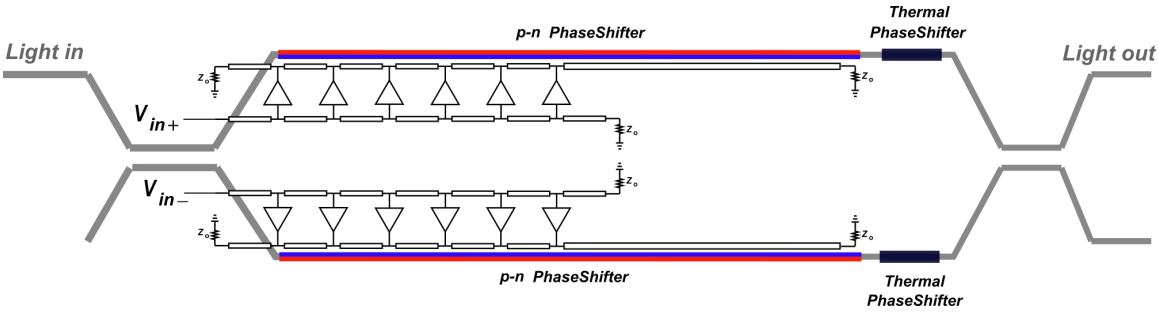

(c) Distributed amplifier merged in a travelling-wave MZM.

Figure 6.1: Comparison of different architectures for integration of driver in silicon photonic Mach-Zehnder modulator based on a distributed driver.

In this work, the novel design show in Fig. 6.1c is proposed to maximize both bandwidth and area efficiency. Here, the DA is merge into the modulator. In this design, the length of optical phase-shifter are no longer limited by the DA, as the output transmission line of the DA acts as the optical phase-shifter simultaneously. As the signal on the output transmission line of the DA propagates, it also results in optical phase-shift in the waveguide. It is also amplified as signals coming from each amplification stage are added along the way, and finally the maximum signal is applying to the longest section of optical phase-shifter electrode. This way all the signals on the output transmission line of the DA are used to generate optical modulation, maximizing efficiency and area usage. The challenge here however is velocity matching, as three signal must propagate with the same velocity. The first one is the electrical signal at the input transmission line of the DA. The seconds one is the electrical signal at the output transmission line of the DA. And the third one is the optical signal coming from the laser source and propagating through optical waveguide. This prompts to perform extensive electromagnetic simulations on all three structure. This has been done in this work, however process variation in the optical phase-shifter due to doping level offset could results in a limited bandwidth, and the only way is to counter that is to do post-measurement modeling and optimizing accordingly. Here, the first pass design is reported.

6.3 Driver and MZM Design

Driver is based on two DA stages driven pseudo-differentially. Driver has a differential input and drives a transmission line, which is also anode terminal for p-n junction phase shifters. The driver input is DC coupled. Fig. 6.2 shows the architecture of the driver. Input transmission line is designed to have 50 Ω characteristic impedance. The transmission line is loaded periodically by amplifying stages. The electric wave ampli-

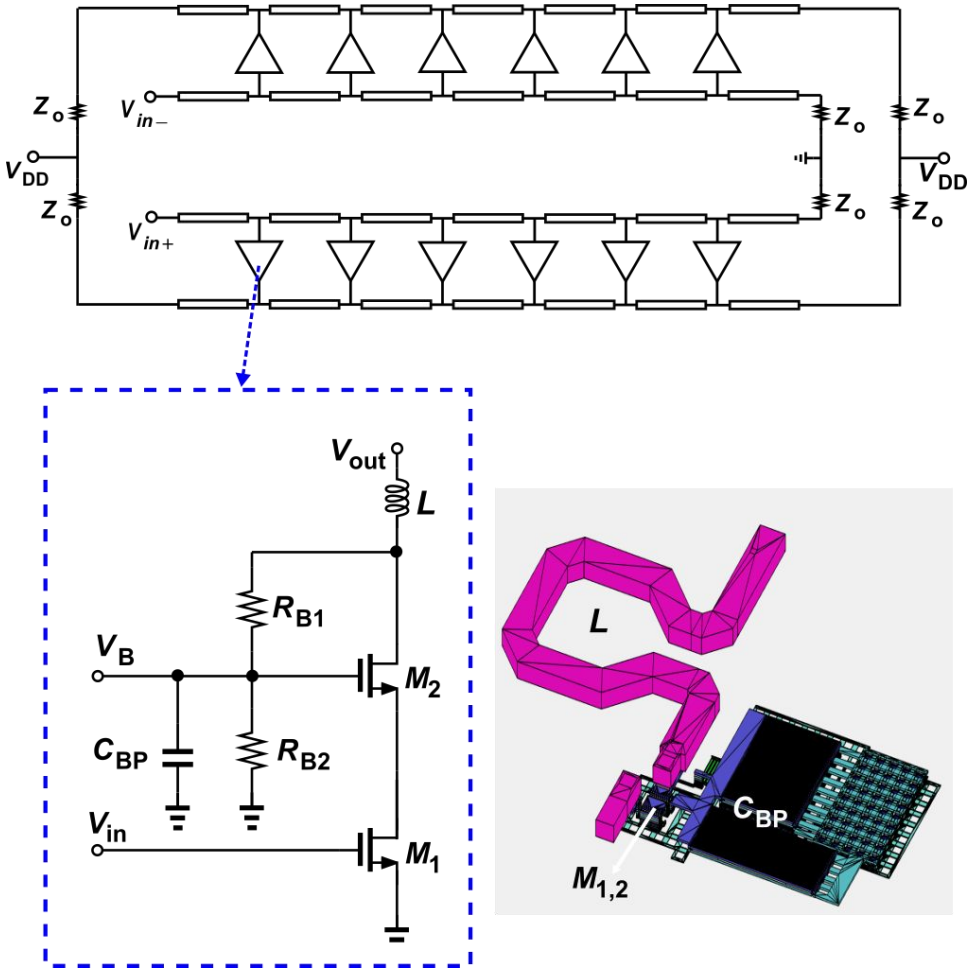

Figure 6.2: Opto-electronic transmitter schematic (top), unit amplification stage based on a cascode amplifier (bottom left), and layout of the cascode stage (bottom right)

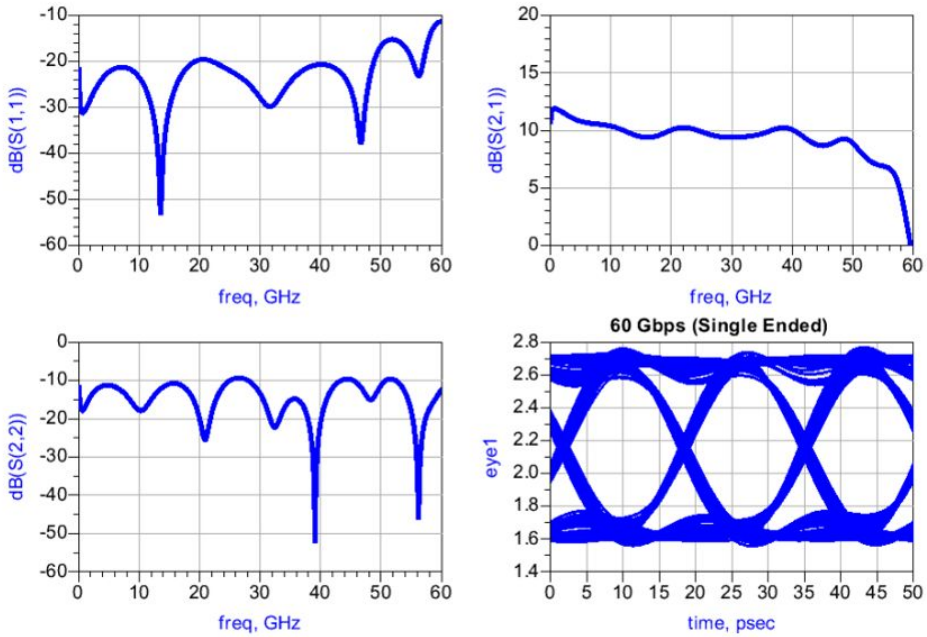

Figure 6.3: Post-layout EM simulated S_{11}, S_{22} and S_{21}, and simulated electrical eye diagram at the output of MZM at 60 Gbps.

tude on the drain transmission line increases across the transmission line and the final amplified signal drives the largest portion of the p-n junction phase shifter. Fig. 6.2 also illustrate the schematic of the unit amplification stage, which is a cascode design with self bias. Since the output transmission line is heavily loaded by capacitive load of optical phase-shifters, inductor L is employed in the drain terminal to decrease loading of the output transmission line by the amplification stage at high frequencies. Also L is sized as a variable to optimize velocity matching. The layout of the cascode unit stage is also shown Fig. 6.2.

Fig. 6.3 post-layout simulation result for the designed DA. The input return loss is better than 20 dB across the frequency band of 0-50 GHz, while output return loss, defined for the on-chip termination, is better than 10 dB. Average small signal gain is about 10 dB for 0-50 GHz, with 3 dB bandwidth of 53 GHz. Finally, simulated eye-diagram with a PRBS 16 pattern shows open eyes at 60 Gbps, with 1.1 V single-

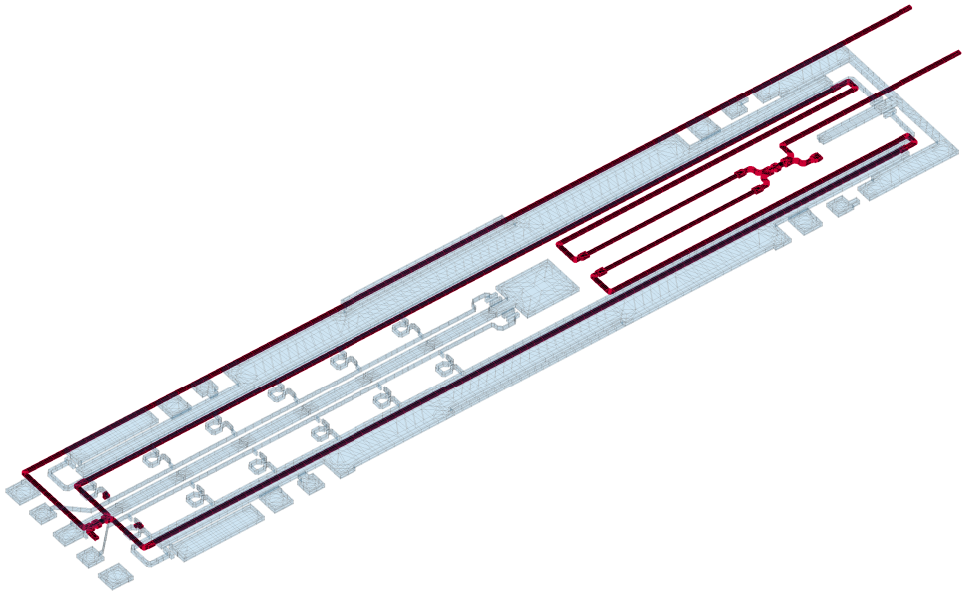

(a) Optical waveguide routing in the fully integrated optical transmitter

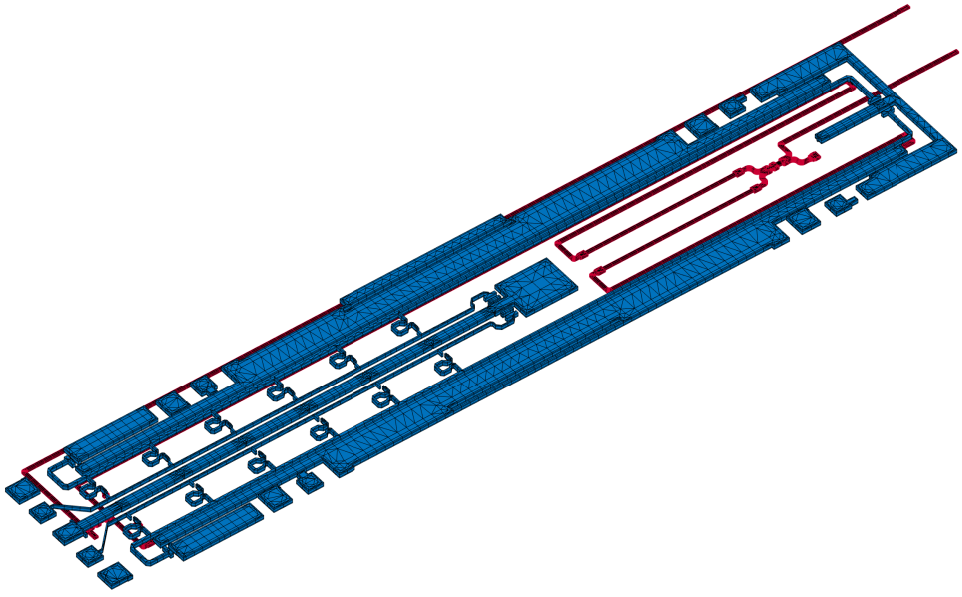

(b) Layout of the fully integrated optical transmitter, showing distributed amplifier merged in MZM

Figure 6.4: 3D view of layout of the designed monolithic optical transmitter

ended voltage swing. Of course this electrical eye will not be the same as optical eye as bandwidth of phase-shifter and their electro-optical conversion efficiency are limited. All EM simulations here are performed using Integrand EMX.

Fig. 6.4 illustrate the layout of the MZM and driver. In Fig. 6.4a, the waveguide connection underneath the electronics are shown. The input and output electrical terminals are based on edge-couplers. There is also one grating-coupler that can be used as the auxiliary optical output. Thermal phase shifters are used to bias the MZM at quadrature point. Fig. 6.4b shows the layout of the whole chip. The total power consumption of the driver is 480 mW.

6.4 Implementation and measurement results

The chip is fabricated in GlobalFoundries CMS90WG technology. Fig. 6.5 shows the opto-electronic transmitter assembly with the fully integrated optical transmitter (left), and chip micro-photograph (right). The chip size is 6×1 mm^2. Surface capacitors are used to bypass the bias traces on the board. Two identical mini-SMP cables are used to drive the optical transmitter. A 13-dBm 1310 nm laser is used as optical source. The output of the MZM is coupled to a 30 GHz Finisar photo-receiver which is connected to a sampling scope. A bit pattern generator is used to drive the transmitter with PRBS 31 pattern, with 550 mV maximum voltage. Bias-Ts are used to provide input bias voltage for the driver.

Measured eye-diagrams for the integrated optical transmitter are shown in Fig. 6.6 for 10, 20, and 30 Gb/s date rates with a PRBS-31 test pattern, where 2-tap FFE is utilized to enhance eye openings.

At higher frequencies optical eyes closes. It's expected that this is mainly due to process variation and uncertainty in modeling of optical phase-shifters in the design.

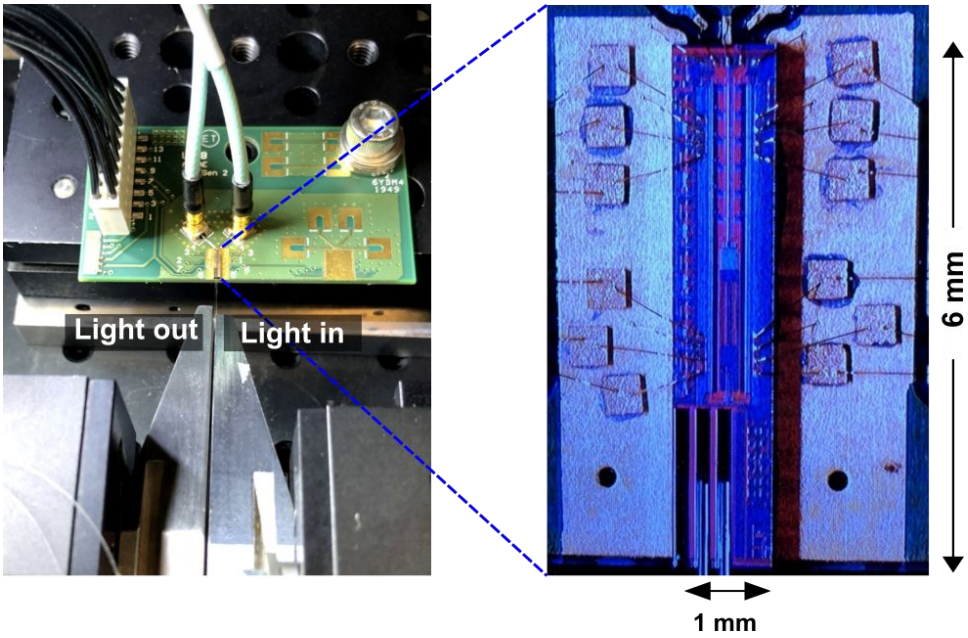

Figure 6.5: Opto-electronic transmitter assembly with the fully integrated optical transmitter (left), and chip micro-photograph (right)

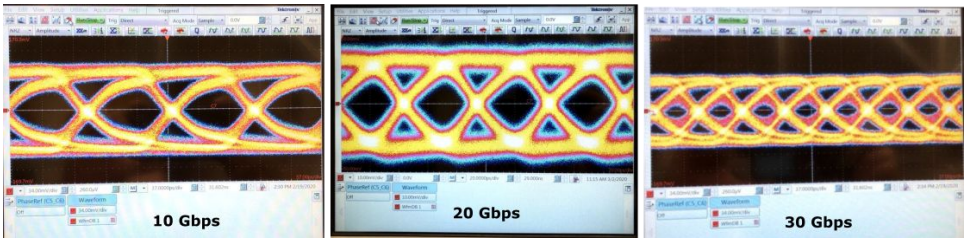

Figure 6.6: Measured eye diagram with PRBS 31 test pattern at 10, 20, and 30 Gb/s data rates.

Any change in doping levels is the p-n phase shifters will result in both optical velocity change and junction capacitor size. Both of these are critical in the design, particularly for electro-optical velocity matching.

6.5 Conclusion

A fully integrated optical transmitter with 90-nm CMOS driver is presented. The novel design maximizes area and bandwidth efficiency. However, this design should be considered a high-risk design in current constancy evolving silicon photonic processes, since it requires a very precise model for optical phase-shifter in order to achieve the maximum simulated bandwidth. Open optical eyes are measured up to 30 Gbps for the first pass implementation.

Chapter 7

Conclusion and Future Work

The potential of silicon photonic integrated circuits for next generation of communication systems has been explored. With the power of electronics integration, and by employing a co-design approach, we can take advantage of extra flexibility in the design to overcome silicon photonic limitations. It has been shown that RF and microwave photonic systems can be designed in silicon photonic technology with performance on par with exotic photonic circuits based on LiNbO3 and III-V technologies. Fully integrated electro-optical promises more efficient and faster communication systems as they are not susceptible to chip-to-chip packaging parasitics.

The work on the wideband high-dynamic range RF photonic receiver can be further developed to test it in a real wireless communication scenario, as shown in Fig. 7.1. For the input LNA of the RoF receiver need to be interface with two (or more) antennas specific for each band. On the other end, the signal of the photo diode needs to be demodulated to extract the original sent signals from each band. This can be done with mixers with different LO frequencies. This type of systems can be utilized for signal distribution in environment with many different frequency channels.

Power optimization on the design of the distributed low noise driver is the next step

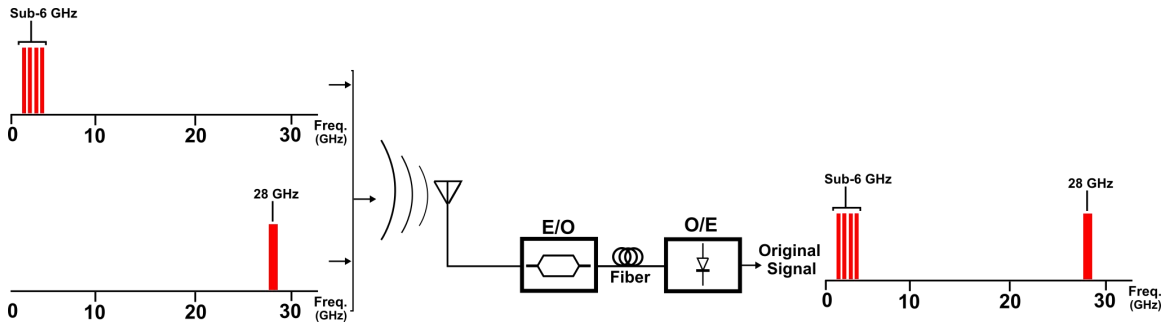

Figure 7.1: Multi-band utilization of the high dynamic range RoF system

to improve the link power efficiency. The current version of the driver consumes close to 1.7W. This is mainly due to the last stage of the driver designed assuming a low V_π modulator. With further progress in improving efficiency of the optical modulators, or by using alternative approaches like optical ring modulators, the voltage swing requirement on the drive chip can be relaxed and power consumption can be reduced significantly. Other stages in the distributed driver design can also be designed for lower output power which will further reduce the power consumption of the chip.

The design of the optical transmitters in chapter 5 and chapter 6 can be further developed to build a coherent optical transmitter using a nested Mach-Zehnder modulator. With the power of an integrated electro-optical process, and with faster CMOS or SiGe transistors, fully integrated coherent optical transceivers can be designed, as illustrated in Fig. 7.1.

This enables building highly efficient optical systems. In addition, if a faster CMOS transistor become available in a photonic process, we can design segmented MZMs and distributed drives to drive all segment. As each segment is a capacitive load for the driver, a fully digital transmitter can be designed to save a large portion of static power. This type of drivers are typically based on inverter cells and for higher swing we can stack transistors to get higher voltages. Of course these type of optical systems cannot be realized with hybrid integration as the wirebond inductance limits the bandwidth when

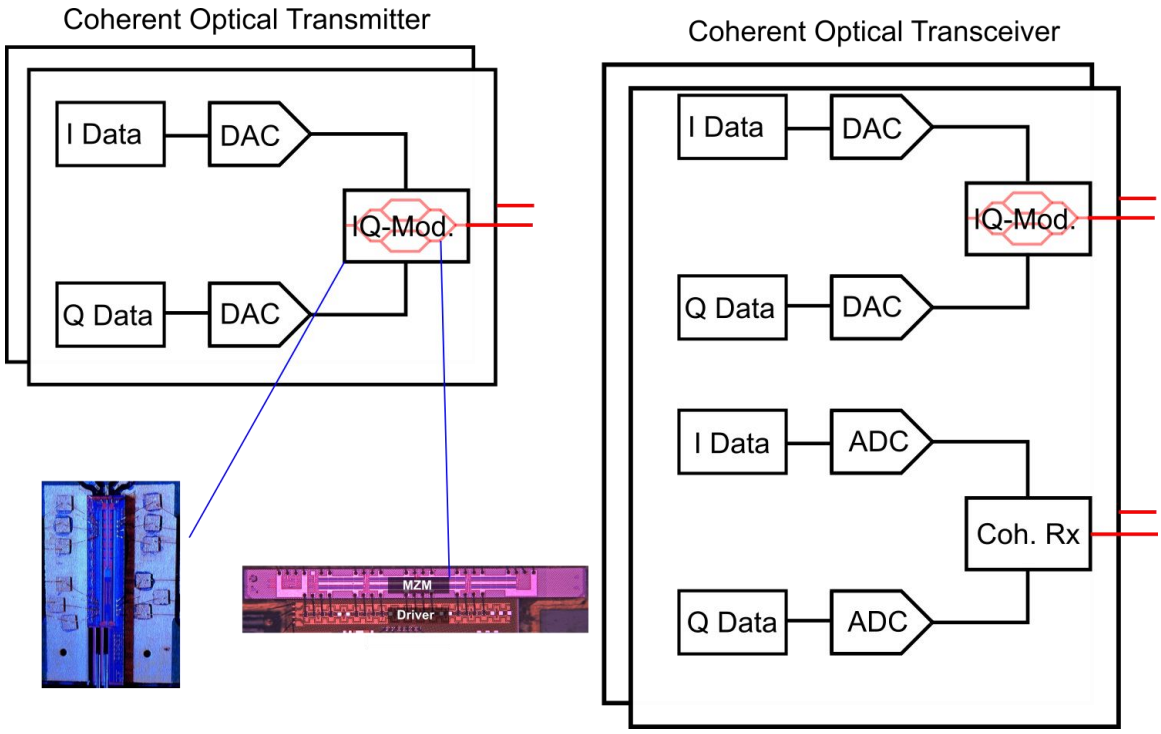

Figure 7.2: Coherent optical transmitter based on a hybrid and monolithic integration of MZM and driver (left), and conceptual illustration of a fully integrated coherent optical transceiver (right) in a fast process.

the load is capacitive. The power efficiency of such systems can be further enhance by employing an equalization based scheme in the driver and controlling the signals and delays on each segment.Alternately, optical ring modulators can be used for electro-optical conversion in the place of Mach-Zehnder modulator. Ring modulators have smaller capacitive input load compared to MZMs, hence a lower power drive can be used for the optical transmitter design.

Appendix A

Appendix

A.1 Volterra Kernels calculations

The Volterra kernels are defined by

$$A_1(j\omega_a) = \frac{1}{1 + j\omega_a C R_i}, \tag{A.1a}$$

$$A_2(j\omega_a, j\omega_b) = \frac{-1}{2} \frac{jC_1 R_i(\omega_a + \omega_b) A_1(j\omega_a) A_1(j\omega_b)}{1 + j(\omega_a + \omega_b) C_0 R_i}, \tag{A.1b}$$

and

$$A_3(j\omega_a, j\omega_b, j\omega_c) = \\ \frac{j(\omega_a + \omega_b + \omega_c) R_i (C_1 \overline{A_{12}} + \frac{C_2}{3} A_1(j\omega_a) A_1(j\omega_b) A_1(j\omega_c))}{1 + j(\omega_a + \omega_b + \omega_c) C R_i}, \tag{A.1c}$$

where

$$\overline{A_{12}} = \frac{1}{3}(A_1(j\omega_a)A_2(j\omega_b, j\omega_c)+$$
$$A_1(j\omega_b)A_2(j\omega_a, j\omega_c) + A_1(j\omega_c)A_2(j\omega_a, j\omega_b)). \tag{A.1d}$$

A.2 Jacobi–Anger Expansion

$$\cos(z\cos\theta) \equiv J_0(z) + 2\sum_{n=1}^{\infty}(-1)^n J_{2n}(z)\cos(2n\theta), \tag{A.2}$$

$$\sin(z\cos\theta) \equiv -2\sum_{n=1}^{\infty}(-1)^n J_{2n-1}(z)\cos\left[(2n-1)\,\theta\right], \tag{A.3}$$

$$\cos(z\sin\theta) \equiv J_0(z) + 2\sum_{n=1}^{\infty} J_{2n}(z)\cos(2n\theta), \tag{A.4}$$

$$\sin(z\sin\theta) \equiv 2\sum_{n=1}^{\infty} J_{2n-1}(z)\sin\left[(2n-1)\,\theta\right]. \tag{A.5}$$

Bibliography

[1] *Cisco Annual Internet Report, 2018–2023*, 2020.

[2] E. Torkildson, U. Madhow, and M. Rodwell, *Indoor Millimeter Wave MIMO: Feasibility and Performance*, *IEEE Transactions on Wireless Communications* **10** (2011), no. 12 4150–4160.

[3] R. W. Heath, N. González-Prelcic, S. Rangan, W. Roh, and A. M. Sayeed, *An overview of signal processing techniques for millimeter wave mimo systems*, *IEEE Journal of Selected Topics in Signal Processing* **10** (2016), no. 3 436–453.

[4] M. Agiwal, A. Roy, and N. Saxena, *Next generation 5g wireless networks: A comprehensive survey*, *IEEE Communications Surveys Tutorials* **18** (2016), no. 3 1617–1655.

[5] *How to stop data centres from gobbling up the world's electricity, author=Jones, Nicola*, *Nature* **561** (2018), no. 7722 163–167.

[6] N. Hosseinzadeh, A. Jain, R. Helkey, and J. F. Buckwalter, *Rf silicon photonics for wideband, high dynamic range microwave and millimeter-wave signal processing*, in *2018 IEEE 18th Topical Meeting on Silicon Monolithic Integrated Circuits in RF Systems (SiRF)*, pp. 41–44, 2018.

[7] F. Berland, T. Fromenteze, D. Boudescoque, P. Di Bin, H. H. Elwan, C. Aupetit-Berthelemot, and C. Decroze, *Microwave photonic mimo radar for short-range 3d imaging*, *IEEE Access* **8** (2020) 107326–107334.

[8] T. Berceli and P. R. Herczfeld, *Microwave Photonics: A Historical Perspective*, *IEEE Transactions on Microwave Theory and Techniques* **58** (Nov, 2010) 2992–3000.

[9] F. Bucholtz, V. J. Urick, M. Godinez, and K. J. Williams, *Graphical Approach for Evaluating Performance Limitations in Externally Modulated Analog Photonic Links*, *IEEE Transactions on Microwave Theory and Techniques* **56** (Jan, 2008) 242–247.

[10] A. H. Ahmed, A. El Moznine, D. Lim, Y. Ma, A. Rylyakov, and S. Shekhar, *A dual-polarization silicon-photonic coherent transmitter supporting 552 gb/s/wavelength*, *IEEE Journal of Solid-State Circuits* (2020) 1–1.

[11] C. L. Schow, *Low Power Analog Coherent Links for Next-Generation Datacenters*, in *2019 Conference on Lasers and Electro-Optics (CLEO)*, pp. 1–2, 2019.

[12] C. L. Schow and K. Schmidtke, *Intrepid: Developing power efficient analog coherent interconnects to transform data center networks*, in *2019 Optical Fiber Communications Conference and Exhibition (OFC)*, pp. 1–3, 2019.

[13] N. Hosseinzadeh, A. Jain, K. Ning, R. Helkey, and J. F. Buckwalter, *A 1 to 20 GHz Silicon-Germanium Low-Noise Distributed Driver for RF Silicon Photonic Mach-Zehnder Modulators*, in *2019 IEEE MTT-S International Microwave Symposium (IMS)*, pp. 774–777, June, 2019.

[14] N. Hosseinzadeh, A. Jain, K. Ning, R. Helkey, and J. F. Buckwalter, *A Linear Microwave Electro-Optic Front End With SiGe Distributed Amplifiers and Segmented Silicon Photonic Mach–Zehnder Modulator*, in *IEEE Transactions on Microwave Theory and Techniques*, vol. 67, pp. 5446–5458, Dec, 2019.

[15] N. Hosseinzadeh, K. Fang, L. Valenzuela, C. Schow, and J. F. Buckwalter, *A 50-Gb/s Optical Transmitter Based on Co-design of a 45-nm CMOS SOI Distributed Driver and 90-nm Silicon Photonic Mach-Zehnder Modulator*, in *2020 IEEE MTT-S International Microwave Symposium (IMS)*, 2020.

[16] N. Hosseinzadeh, A. Jain, R. Helkey, and J. F. Buckwalter, *RF Silicon Photonics for wideband, high dynamic range microwave and millimeter-wave signal processing*, in *2018 IEEE 18th Topical Meeting on Silicon Monolithic Integrated Circuits in RF Systems (SiRF)*, pp. 41–44, Jan, 2018.

[17] F. Gan, *High-speed silicon electro-optic modulator for electronic photonic integrated circuits*. PhD thesis, Massachusetts Institute of Technology, 2007.

[18] V. J. Urick, K. J. Williams, and J. D. McKinney, *Fundamentals of microwave photonics*. John Wiley & Sons, 2015.

[19] N. Hosseinzadeh, A. Jain, R. Helkey, and J. Buckwalter, *Sources of RF Intermodulation Distortion in Silicon Photonic Modulators*, in *2018 Proc. IEEE Avion. Veh. Fiber-Opt. Photon. Technol. Conf.*, pp. 1–2, Nov, 2018.

[20] R. G. Meyer and M. L. Stephens, *Distortion in Variable-capacitance Diodes*, .

[21] R. Soref and B. Bennett, *Electrooptical Effects in Silicon*, .

[22] A. Jain, N. Hosseinzadeh, X. Wu, H. K. Tsang, R. Helkey, J. E. Bowers, and J. Buckwalter, *A High Spur-Free Dynamic Range Silicon DC Kerr Ring Modulator for RF Applications*, *IEEE/OSA Journal of Lightwave Technology* (2019) 1–1.

[23] C. H. Henry, R. A. Logan, and K. A. Bertness, *Spectral dependence of the change in refractive index due to carrier injection in GaAs lasers*, *Journal of Applied Physics* **52** (1981), no. 7 4457–4461, [https://doi.org/10.1063/1.329371].

[24] R. Soref and J. Larenzo, *All-silicon active and passive guided-wave components for Lambda = 1.3 um and 1.6 um*, .

[25] M. Nedeljkovic, R. Soref, and G. Z. Mashanovich, *Free-Carrier Electrorefraction and Electroabsorption Modulation Predictions for Silicon Over the 1–14-m Infrared Wavelength Range*, .

[26] L. Chrostowski and M. Hochberg, *Silicon Photonics Design: From Devices to Systems*. Cambridge University Press, 2015.

[27] R. W. Ridgway, C. L. Dohrman, and J. A. Conway, *Microwave photonics programs at darpa*, *Journal of Lightwave Technology* **32** (2014), no. 20 3428–3439.

[28] S. Pan, D. Zhu, S. Liu, K. Xu, Y. Dai, T. Wang, J. Liu, N. Zhu, Y. Xue, and N. Liu, *Satellite Payloads Pay Off*, *IEEE Microwave Magazine* **16** (Sep., 2015) 61–73.

[29] V. J. Urick, M. S. Rogge, P. F. Knapp, L. Swingen, and F. Bucholtz, *Wide-band predistortion linearization for externally modulated long-haul analog fiber-optic links*, *IEEE Transactions on Microwave Theory and Techniques* **54** (June, 2006) 1458–1463.

[30] C. Zhang, P. A. Morton, J. B. Khurgin, J. D. Peters, and J. E. Bowers, *Ultralinear Heterogeneously Integrated Ring-assisted Mach-Zehnder Interferometer Modulator on Silicon*, *Optica* **3** (Dec, 2016) 1483–1488.

[31] J. Ding, S. Shao, L. Zhang, X. Fu, and L. Yang, *Method to improve the linearity of the silicon Mach-Zehnder optical modulator by doping control*, *Opt. Express* **24** (Oct, 2016) 24641–24648.

[32] C. Zhang, P. A. Morton, J. B. Khurgin, J. D. Peters, and J. E. Bowers, *Highly linear heterogeneous-integrated Mach-Zehnder interferometer modulators on Si*, *Opt. Express* **24** (Aug, 2016) 19040–19047.

[33] J. Cardenas, P. A. Morton, J. B. Khurgin, A. Griffith, C. B. Poitras, K. Preston, and M. Lipson, *Linearized silicon modulator based on a ring assisted Mach Zehnder inteferometer*, in *Opt. Express*, vol. 21, pp. 22549–22557, OSA, Sep, 2013.

[34] C. Xiong, D. Gill, J. Rosenberg, M. Khater, T. Barwicz, S. Assefa, S. Shank, C. Reinholm, E. Kiewra, J. Ellis-Monaghan, S. Kamlapurkar, A. Stricker, W. Green, Y. A. Vlasov, and W. Haensch, *A Linear Push-Pull Silicon Optical Modulator*, in *Frontiers in Optics 2014*, p. FM3A.4, Optical Society of America, 2014.

[35] Y. Zhou, L. Zhou, F. Su, J. Xie, H. Zhu, X. Li, and J. Chen, *Linearity measurement of a silicon single-drive push-pull mach-zehnder modulator*, in *2015 Conference on Lasers and Electro-Optics (CLEO)*, pp. 1–2, IEEE, 2015.

[36] A. Ayazi, T. Baehr-Jones, Y. Liu, A. E.-J. Lim, and M. Hochberg, *Linearity of silicon ring modulators for analog optical links*, *Opt. Express* **20** (Jun, 2012) 13115–13122.

[37] A. Gutiérrez, J. Galan, J. Herrera, A. Brimont, M. Aamer, J. Martí, D. Marris-Morini, L. Vivien, J. Fédéli, D. Thomson, *et. al.*, *Silicon-based electro-optic modulators for linear and nonlinear radio-over-fiber applications*, in *2012 IEEE International Topical Meeting on Microwave Photonics*, pp. 168–171, IEEE, 2012.

[38] A. M. Gutierrez, J. V. Galan, J. Herrera, A. Brimont, D. Marris-Morini, J. M. FÃ©dÃ©li, L. Vivien, and P. Sanchis, *High linear ring-assisted MZI electro-optic silicon modulators suitable for radio-over-fiber applications*, in *The 9th International Conference on Group IV Photonics (GFP)*, pp. 57–59, Aug, 2012.

[39] L. Chen, J. Chen, J. Nagy, and R. M. Reano, *Highly linear ring modulator from hybrid silicon and lithium niobate*, *Opt. Express* **23** (May, 2015) 13255–13264.

[40] M. Streshinsky, A. Ayazi, Z. Xuan, A. E.-J. Lim, G.-Q. Lo, T. Baehr-Jones, and M. Hochberg, *Highly linear silicon traveling wave Mach-Zehnder carrier depletion modulator based on differential drive*, *Opt. Express* **21** (Feb, 2013) 3818–3825.

[41] D. Zhu, J. Chen, and S. Pan, *Multi-octave linearized analog photonic link based on a polarization-multiplexing dual-parallel Mach-Zehnder modulator*, *Opt. Express* **24** (May, 2016) 11009–11016.

[42] X. Han, X. Chen, and J. Yao, *Simultaneous even- and third-order distortion suppression in a microwave photonic link based on orthogonal polarization modulation, balanced detection, and optical sideband filtering*, *Opt. Express* **24** (Jun, 2016) 14812–14827.

[43] S. Li, X. Zheng, H. Zhang, and B. Zhou, *Highly Linear Radio-Over-Fiber System Incorporating a Single-Drive Dual-Parallel Mach Zehnder Modulator*, *IEEE Photonics Technology Letters* **22** (Dec, 2010) 1775–1777.

[44] X. J. Meng and A. Karim, *microwave photonic link with carrier suppression for increased dynamic range*, .

[45] Z. Chen, L. Yan, W. Pan, B. Luo, X. Zou, Y. Guo, H. Jiang, and T. Zhou, *SFDR enhancement in analog photonic links by simultaneous compensation for dispersion and nonlinearity*, *Opt. Express* **21** (Sep, 2013) 20999–21009.

[46] R. Zhu, X. Zhang, D. Shen, and Y. Zhang, *Ultra Broadband Predistortion Circuit for Radio-over-Fiber Transmission Systems*, *IEEE/OSA Journal of Lightwave Technology* **34** (Nov, 2016) 5137–5145.

[47] S. Jin, L. Xu, and Y. Li, *Quantum well mach-zehnder intensity modulator with enhanced linearity*, in *2016 IEEE MTT-S Int. Microw. Symp. Dig.*, pp. 1–3, May, 2016.

[48] B. Liu, J. Shim, Y.-J. Chiu, A. Keating, J. Piprek, and J. E. Bowers, *Analog characterization of low-voltage MQW traveling-wave electroabsorption modulators*, *IEEE/OSA Journal of Lightwave Technology* **21** (Dec, 2003) 3011–3019.

[49] A. Rao, A. Patil, P. Rabiei, A. Honardoost, R. DeSalvo, A. Paolella, and S. Fathpour, *High-performance and linear thin-film lithium niobate Machâ"Zehnder modulators on silicon up to 50 GHz*, *Opt. Lett.* **41** (Dec, 2016) 5700–5703.

[50] P. A. Morton, J. Cardenas, M. Lipson, and J. B. Khurgin, *Miniature, Linearized silicon photonics modulators for phased array systems*, in *2013 Proc. IEEE Int. Topical Meeting Microw. Photon.*, pp. 275–277, Oct, 2013.

[51] I. Garcia Lopez, A. Aimone, P. Rito, S. Alreesh, T. Brast, V. Höhns, G. Fiol, M. Gruner, J. K. Fischer, J. Honecker, A. G. Steffan, M. Schell, A. Awny, A. C. Ulusoy, and D. Kissinger, *High-Speed Ultralow-Power Hybrid Optical Transmitter Module With InP I/Q-SEMZM and BiCMOS Drivers With 4-b Integrated DAC*, *IEEE Transactions on Microwave Theory and Techniques* **64** (Dec, 2016) 4598–4610.

[52] P. Rito, I. García López, D. Petousi, L. Zimmermann, M. Kroh, S. Lischke, D. Knoll, D. Micusik, A. Awny, A. C. Ulusoy, and D. Kissinger, *A Monolithically Integrated Segmented Linear Driver and Modulator in EPIC 0.25- μ m SiGe:C BiCMOS Platform*, *IEEE Transactions on Microwave Theory and Techniques* **64** (Dec, 2016) 4561–4572.

[53] A. Zandieh, P. Schvan, and S. P. Voinigescu, *Linear Large-Swing Push–Pull SiGe BiCMOS Drivers for Silicon Photonics Modulators*, *IEEE Transactions on Microwave Theory and Techniques* **65** (Dec, 2017) 5355–5366.

[54] P. Rito, I. García López, A. Awny, M. Ko, A. C. Ulusoy, and D. Kissinger, *A DC-90-GHz 4- V_{pp} Modulator Driver in a 0.13- μm SiGe:C BiCMOS Process*, *IEEE Transactions on Microwave Theory and Techniques* **65** (Dec, 2017) 5192–5202.

[55] B. G. Lee, N. Dupuis, J. Orcutt, J. Ayala, K. Nummy, H. Ainspan, J. E. Proesel, C. W. Baks, D. M. Gill, M. Meghelli, and W. M. J. Green, *FEC-Free 60-Gb/s Silicon Photonic Link Using SiGe-Driver ICs Hybrid-Integrated with Photonics-Enabled CMOS*, in *Optical Fib. Comm. Conf.*, p. M2D.4, Optical Society of America, 2018.

[56] E. Timurdogan, C. V. Poulton, M. Byrd, and M. Watts, *Electric field-induced second-order nonlinear optical effects in silicon waveguides*, *Nature Photonics* **11** (2017), no. 3 200.

[57] C. G. Bottenfield, V. A. Thomas, and S. E. Ralph, *Silicon photonic modulator linearity and optimization for microwave photonic links*, *IEEE Journal of Selected Topics in Quantum Electronics* **25** (2019), no. 5 1–10.

[58] R. Zhu, X. Zhang, D. Shen, and Y. Zhang, *Ultra Broadband Predistortion Circuit for Radio-over-Fiber Transmission Systems*, *Journal of Lightwave Technology* **34** (Nov, 2016) 5137–5145.

[59] W. Jiang, Q. Tan, W. Qin, D. Liang, X. Li, H. Ma, and Z. Zhu, *A Linearization Analog Photonic Link With High Third-Order Intermodulation Distortion Suppression Based on Dual-Parallel Mach–Zehnder Modulator*, *IEEE Photonics Journal* **7** (June, 2015) 1–8.

[60] A. Karim and J. Devenport, *High Dynamic Range Microwave Photonic Links for RF Signal Transport and RF-IF Conversion*, *Journal of Lightwave Technology* **26** (Aug, 2008) 2718–2724.

[61] A. Nikolov, D. Guenther, W. Liu, R. Cendejas, and R. Dutt, *Advancements and Challenges for Photonic Components For Avionic Interconnects*, in *2013 IEEE AVFOP*, pp. 5–6, Oct, 2013.

[62] R. Sadhwani and B. Jalali, *Adaptive cmos predistortion linearizer for fiber-optic links*, *Journal of Lightwave Technology* **21** (2003), no. 12 3180–3193.

[63] Y. Chiu, B. Jalali, S. Garner, and W. Steier, *Broad-band electronic linearizer for externally modulated analog fiber-optic links*, *IEEE Photonics Technology Letters* **11** (1999), no. 1 48–50.

[64] J. Okyere, K. Yu, K. Entesari, and S. Palermo, *A fifth-order polynomial predistortion circuit for mach-zehnder modulator linearization in 65nm cmos*, in

2017 Texas Symposium on Wireless and Microwave Circuits and Systems (WMCS), pp. 1–4, 2017.

[65] N. Hosseinzadeh, A. Jain, K. Ning, R. Helkey, and J. F. Buckwalter, *A 0.5-20 GHz RF Silicon Photonic Receiver with 120 dB•Hz2/3 SFDR using Broadband Distributed IM3 Injection Linearization*, in *2019 IEEE Radio Frequency Integrated Circuits Symposium (RFIC)*, pp. 99–102, June, 2019.

[66] C. G. Bottenfield, V. A. Thomas, and S. E. Ralph, *Microwave photonic links: Optimizing sip modulator design and operation*, in *2019 Optical Fiber Communications Conference and Exhibition (OFC)*, pp. 1–3, 2019.

[67] A. Jain, N. Hosseinzadeh, X. Wu, H. K. Tsang, R. Helkey, J. E. Bowers, and J. F. Buckwalter, *A high spur-free dynamic range silicon dc kerr ring modulator for rf applications*, *Journal of Lightwave Technology* **37** (2019), no. 13 3261–3272.

[68] S. Lou and H. C. Luong, *A linearization technique for rf receiver front-end using second-order-intermodulation injection*, *IEEE Journal of Solid-State Circuits* **43** (2008), no. 11 2404–2412.

[69] K. Fang, C. S. Levy, and J. F. Buckwalter, *Supply-scaling for efficiency enhancement in distributed power amplifiers*, *IEEE Journal of Solid-State Circuits* **51** (2016), no. 9 1994–2005.

[70] L. Szilagyi, R. Henker, D. Harame, and F. Ellinger, *2.2-pJ/bit 30-Gbit/s Mach-Zehnder Modulator Driver in 22-nm-FDSOI*, in *2018 IEEE/MTT-S International Microwave Symposium - IMS*, pp. 1530–1533, June, 2018.

[71] K. Li, D. J. Thomson, S. Liu, P. Wilson, and G. T. Reed, *A 30 Gb/s CMOS driver integrated with silicon photonics MZM*, in *2015 IEEE Radio Frequency Integrated Circuits Symposium (RFIC)*, pp. 311–314, May, 2015.

[72] I. G. López, P. Rito, D. Petousi, S. Lischke, D. Knoll, M. Kroh, L. Zimmermann, M. Ko, A. C. Ulusoy, and D. Kissinger, *Monolithically Integrated Si Photonics Transmitters in 0.25 um BiCMOS Platform for High-Speed Optical Communications*, in *2018 IEEE/MTT-S International Microwave Symposium - IMS*, pp. 1312–1315, June, 2018.

[73] D. M. Gill, J. Proesel, C. Xiong, J. C. Rosenberg, M. Khater, T. Barwicz, S. Assefa, S. M. Shank, C. Reinholm, E. Kiewra, J. Ellis-Monaghan, S. Kamlapurkar, W. M. J. Green, and Y. A. Vlasov, *Monolithic travelling-wave Mach-Zehnder transmitter with high-swing stacked CMOS driver*, in *2014 Conference on Lasers and Electro-Optics (CLEO) - Laser Science to Photonic Applications*, pp. 1–2, June, 2014.

[74] Z. Yong, S. Shopov, J. C. Mikkelsen, R. Mallard, J. C. C. Mak, S. P. Voinigescu, and J. K. S. Poon, *A 44Gbps high extinction ratio silicon Mach-Zehnder modulator with a 3D-integrated 28nm FD-SOI CMOS driver*, in *2017 Optical Fiber Communications Conference and Exhibition (OFC)*, pp. 1–3, March, 2017.

[75] B. Analui, D. Guckenberger, D. Kucharski, and A. Narasimha, *A fully integrated 20-gb/s optoelectronic transceiver implemented in a standard 0.13- μm cmos soi technology*, *IEEE Journal of Solid-State Circuits* **41** (2006), no. 12 2945–2955.

[76] J. F. Buckwalter, J. Kim, X. Zheng, G. Li, K. Raj, and A. Krishnamoorthy, *A fully-integrated optical duobinary transceiver in a 130nm soi cmos technology*, in *2011 IEEE Custom Integrated Circuits Conference (CICC)*, pp. 1–4, 2011.

[77] K. Gupta, *A 1pj/bit 10gbps optical carrier-injection ring modulator and all-digital driver circuit in 45nm soi*, in *2015 IEEE Dallas Circuits and Systems Conference (DCAS)*, pp. 1–4, 2015.

[78] S. Assefa, W. M. J. Green, A. Rylyakov, C. Schow, F. Horst, and Y. A. Vlasov, *Monolithic integration of cmos and nanophotonic devices for massively parallel optical interconnects in supercomputers*, in *69th Device Research Conference*, pp. 253–256, 2011.

[79] J. F. Buckwalter, X. Zheng, G. Li, K. Raj, and A. V. Krishnamoorthy, *A monolithic 25-gb/s transceiver with photonic ring modulators and ge detectors in a 130-nm cmos soi process*, *IEEE Journal of Solid-State Circuits* **47** (2012), no. 6 1309–1322.

[80] A. Narasimha, B. Analui, Y. Liang, T. J. Sleboda, S. Abdalla, E. Balmater, S. Gloeckner, D. Guckenberger, M. Harrison, R. G. M. P. Koumans, D. Kucharski, A. Mekis, S. Mirsaidi, D. Song, and T. Pinguet, *A fully integrated 4 $\times$ 10-gb/s dwdm optoelectronic transceiver implemented in a standard 0.13 μm cmos soi technology*, *IEEE Journal of Solid-State Circuits* **42** (2007), no. 12 2736–2744.

[81] D. M. Gill, J. Proesel, C. Xiong, J. C. Rosenberg, M. Khater, T. Barwicz, S. Assefa, S. M. Shank, C. Reinholm, E. Kiewra, J. Ellis-Monaghan, S. Kamlapurkar, W. M. J. Green, and Y. A. Vlasov, *Monolithic travelling-wave Mach-Zehnder transmitter with high-swing stacked CMOS driver*, in *2014 Conference on Lasers and Electro-Optics (CLEO) - Laser Science to Photonic Applications*, pp. 1–2, 2014.

[82] P. Rito, I. G. López, D. Petousi, L. Zimmermann, M. Kroh, S. Lischke, D. Knoll, D. Kissinger, and A. C. Ulusoy, *A monolithically integrated segmented driver and modulator in 0.25 m sige:c bicmos with 13 db extinction ratio at 28 gb/s*, in *2016 IEEE MTT-S International Microwave Symposium (IMS)*, pp. 1–4, 2016.

[83] J. Park, S. Takagi, and M. Takenaka, *Monolithic integration of InGaAsP MZI modulator and InGaAs driver MOSFET using III-V CMOS photonics*, in *2017 Optical Fiber Communications Conference and Exhibition (OFC)*, pp. 1–3, 2017.

[84] D. Petousi, L. Zimmermann, P. Rito, M. Kroh, D. Knoll, S. Lischke, C. Mai, I. G. Lopez, A. C. Ulusoy, G. Winzer, K. Voigt, and K. Petermann, *Monolithic photonic BiCMOS sub-system comprising MZM and segmented driver with 13 dB ER at 28 Gb/s*, in *2016 Conference on Lasers and Electro-Optics (CLEO)*, pp. 1–2, 2016.

[85] P. Rito, I. García López, B. Heinemann, A. Awny, A. C. Ulusoy, and D. Kissinger, *A 28 Gb/s 3-V optical driver with high efficiency in a complementary SiGe:C BiCMOS technology*, in *2017 IEEE 17th Topical Meeting on Silicon Monolithic Integrated Circuits in RF Systems (SiRF)*, pp. 23–25, 2017.

[86] I. García López, P. Rito, D. Petousi, L. Zimmermann, M. Kroh, S. Lischke, D. Knoll, A. Awny, A. C. Ulusoy, and D. Kissinger, *A 40 Gb/s PAM-4 monolithically integrated photonic transmitter in 0.25 m SiGe:C BiCMOS EPIC platform*, in *2017 IEEE 17th Topical Meeting on Silicon Monolithic Integrated Circuits in RF Systems (SiRF)*, pp. 30–32, 2017.

[87] P. Rito, I. García López, D. Petousi, L. Zimmermann, M. Kroh, S. Lischke, D. Knoll, D. Micusik, A. Awny, A. C. Ulusoy, and D. Kissinger, *A Monolithically Integrated Segmented Linear Driver and Modulator in EPIC 0.25- μ m SiGe:C BiCMOS Platform*, *IEEE Transactions on Microwave Theory and Techniques* **64** (2016), no. 12 4561–4572.

[88] C. Xiong, D. Gill, J. Proesel, J. Orcutt, W. Haensch, and W. M. J. Green, *A Monolithic 56 Gb/s CMOS Integrated Nanophotonic PAM-4 Transmitter*, in *2015 IEEE Optical Interconnects Conference (OI)*, pp. 16–17, 2015.

[89] H. Andrade, T. Hirokawa, A. Maharry, A. Rylyakov, C. L. Schow, and J. F. Buckwalter, *Monolithically-Integrated 50 Gbps 2pJ/bit Photoreceiver with Cherry-Hooper TIA in 250nm BiCMOS Technology*, in *Optical Fiber Communication Conference (OFC) 2019*, p. M3A.5, Optical Society of America, 2019.

[90] H. Andrade, A. Maharry, T. Hirokawa, L. Valenzuela, S. Simon, C. L. Schow, and J. F. Buckwalter, *Comparison of three monolithically integrated TIA topologies for 50 Gb/s OOK and PAM4*, in *Optical Interconnects XX*, vol. 11286, p. 112860W, International Society for Optics and Photonics, 2020.

[91] H. Andrade, A. Maharry, T. Hirokawa, L. Valenzuela, S. PINNA, C. Schow, J. Buckwalter, and S. Simon, *Analysis and Monolithic Implementation of Differential Transimpedance Amplifiers*, *Journal of Lightwave Technology* (2020) 1–1.

[92] D. M. Gill, J. E. Proesel, C. Xiong, J. S. Orcutt, J. C. Rosenberg, M. H. Khater, T. Barwicz, S. Assefa, S. M. Shank, C. Reinholm, J. Ellis-Monaghan, E. Kiewra, S. Kamlapurkar, C. M. Breslin, W. M. J. Green, W. Haensch, and Y. A. Vlasov, *Demonstration of a High Extinction Ratio Monolithic CMOS Integrated Nanophotonic Transmitter and 16 Gb/s Optical Link*, *IEEE Journal of Selected Topics in Quantum Electronics* **21** (2015), no. 4 212–222.

[93] B. Wohlfeil, N. Eiselt, P. Rito, A. Dochhan, G. R. Mehrpoor, D. Rafique, D. Petousi, I. Lopez, S. Lischke, D. Kissinger, L. Zimmermann, M. Eiselt, H. Griesser, and J. Elbers, *First Demonstration of Fully Integrated Segmented Driver and MZM in* $0.25 - \mu$m *SiGe BiCMOS employing 112 Gb/s PAM4 over 60 km SSMF*, in *2018 European Conference on Optical Communication (ECOC)*, pp. 1–3, 2018.

[94] C. Xiong, D. Gill, J. Proesel, J. Orcutt, W. Haensch, and W. M. J. Green, *A monolithic 56 Gb/s CMOS integrated nanophotonic PAM-4 transmitter*, in *2015 IEEE Optical Interconnects Conference (OI)*, pp. 16–17, 2015.